University of Nevada, Reno

INVESTIGATION INTO FRACTURE NETWORK PERMEABILITY EVOLUTION AND GEOTHERMAL RESERVOIR DEFORMATION IN RESPONSE TO HYDRAULIC STIMULATION, UTILIZING COUPLED THERMO-HYDRO-MECHANICAL MODELING

A dissertation submitted in partial fulfillment of the
requirements for the degree of Doctor of Philosophy in
Geo-Engineering

by

Stefano Benato

Dr. Greg M. Pohll Dissertation Advisor

December 2014

THE GRADUATE SCHOOL

We recommend that the dissertation
prepared under our supervision by

STEFANO BENATO

Entitled

Investigation Into Fracture Network Permeability Evolution And Geothermal Reservoir Deformation In Response To Hydraulic Stimulation, Utilizing Coupled Thermo-Hydro-Mechanical Modeling

be accepted in partial fulfillment of the
requirements for the degree of

DOCTOR OF PHILOSOPHY

Greg M. Pohll, Ph.D., Advisor

Robert J. Watters, Ph.D., Committee Member

James "Jim" R. Carr, Ph.D., Committee Member

Joshua Taron, Ph.D., Committee Member

James "Jim" M. Thomas, Ph.D., Graduate School Representative

David W. Zeh, Ph. D., Dean, Graduate School

December, 2014

ABSTRACT

A series of hydraulic stimulations aimed at enhancing reservoir fracture-permeability were carried out in Desert Peak geothermal well 27-15 from September 2010 to March 2013. Fracture-permeability is controlled by the combined influence of induced thermal (T), hydrologic (H), and mechanical (M) processes, also known as THM. A hydro-mechanical (FLAC3D) model first, and a dual-porosity thermo-hydro-mechanical (TFReact) model second, are implemented to test if the proposed conceptual model is generally able to reproduce observations from the stimulation treatment. Numerical simulations are performed to determine: a) pore pressure diffusion and stress field modifications, b) development of mechanical deformation, and, above all c) relative impact of thermo-mechanical vs. shear deformation on reservoir permeability evolution.

Both FLAC3D and TFReact coupled models display an evident cause-effect relation between stimulation of either the *shallow* or the *extended* intervals and shear deformation on a deep known structural feature, the STF (*"Shearing Target Fault"* – where most of the induced micro-seismicity is observed). Injection-induced thermo-mechanical and hydro-mechanical processes are found to govern permeability enhancement during stimulation of the *shallow* interval in well 27-15. Conversely, induced shear failure processes developing on a larger structural feature (STF) seem to control most of the permeability gain produced during the well 27-15 *extended* interval stimulation. Distinctive signatures at the well-head (pressure curve) are shown by the different permeability-change processes, and this is confirmed and matched by coupled THM simulation results.

TABLE OF CONTENTS

INTRODUCTION

This Ph.D. Dissertation is composed of three scientific papers. A summary of the research covered in the manuscripts is provided in the following short paragraphs, after which a status and brief outline are presented for each paper before they unfold. Overall results and conclusions are recapped at the end of the Dissertation.

1 RESEARCH SUMMARY

1.1 Background

Like many other geothermal fields, the volume of hot rock surrounding the Desert Peak field (Nevada, USA) is far more extensive than the volume of hot *and* permeable rock. These circumstances drove the need for a series of hydraulic stimulations aimed at enhancing reservoir fracture-permeability (Enhanced Geothermal System or EGS). Stimulation treatments were carried out in well 27-15 from September 2010 to March 2013. Hydraulic stimulations were operated through a *shallow* (920m to 1070m) interval first, and an *extended* (920m to 1770m) interval later. Injectivity values improved more than ~70 fold and the well currently contributes an extra power plant output of ~1.7 MW.

1.2 Problem Statement

Fracture permeability is controlled by the combined influence of induced thermal (T), hydrologic (H), mechanical (M), and chemical (C) processes, also known as THMC. These processes interplay in a complex and non-linear way, and they can enhance or inhibit fluid transmission. The success of a variety of geo-engineering applications, including Geothermal, largely depends on a better understanding of implications, interactions and roles attached to these mechanisms.

1.3 Objectives and Scope

The goal of this research is to investigate and simulate any potential injection-induced permeability change mechanism (i.e., tensile and shear dilation) and to match their pressure response at the wellhead. This study puts forth the following main objectives:

1) to identify any structure that (a) appears to be spatially associated with the development of induced microseismicity, and (b) may also represent a permeability conduit enabling a connection to the rest of the field;
2) to numerically simulate induced fluid pressure diffusion in the reservoir in order to establish whether it is an effective trigger for frictional failure within the identified structures;
3) to numerically simulate permeability changes activated by either or both injection-induced thermo-mechanical and/or shear deformation;
4) to simulate alternative stimulation scenarios that may yield greater permeability gains.

1.4 Methodology

A conceptual model and a DFN (Discrete Fracture Network) model are first developed based on a synthesis and analysis of previously acquired field data. Hydro-mechanical (FLAC3D) and dual-porosity thermo-hydro-mechanical (TFReact) numerical simulations are then implemented to test if the proposed conceptual model is generally able to reproduce observations from the stimulation treatment. FLAC3D is a three-dimensional explicit finite-difference program for continuum mechanics computation, which also models fluid flow and its corresponding poromechanical effects. TFReact couples the solid mechanics analyses of FLAC3D with the multiphase, non-isothermal and reactive capabilities of TOUGHREACT. Numerical simulations are performed to determine: a) pore pressure diffusion and stress field modifications, b) mechanical deformation development and, above all, c) relative impact of thermo-mechanical vs. shear deformation on reservoir permeability evolution.

2 MANUSCRIPT OUTLINES

2.1 Manuscript I (pp. 5 to 46)

Title: Computational Investigation of Hydro-Mechanical Effects on Transmissivity Evolution During the Initial Injection Phase at the Desert Peak EGS Project, NV.

Status: Published in Proceedings of the 2013 Stanford Workshop on Geothermal Reservoir Engineering, SGP-TR-198.

This paper provides a quantitative and qualitative initial assessment of (1) 3D site-specific geometry of key structures involved in the experiment, 2) representative statistical fracture network from FMS/ABI85 image and TPS log analyses, 3) DFN (Discrete Fracture Network) simulations, equivalent permeability tensors and preferred fluid migration directions, and 4) a FLAC3D hydro-mechanical simulation of the initial September 2010, low flow-rate stimulation phase in well 27-15, testing the potential for hydraulically-induced shear failure activation along identified geological structures.

2.2 Manuscript II (pp. 47 to 92)

Title: Desert Peak EGS Project Conceptual Model and Numerical Analysis: Reservoir Response to the Shallow Medium Flow-Rate Hydraulic Stimulation Phase.

Status: imminent submission to Geothermics Elsevier EGS Special Issue.

Based on additional induced seismicity datasets acquired after the publication of the first study, this paper provides a more in-depth analysis of possible cause-effect relations between hydraulic injection operations in well 27-15 and the development of induced microseismicity on a deep structural feature or STF (Shearing Target Fault) introduced in the above Stanford-published paper. As part of this study, a detailed assessment of the reservoir baseline permeability is carried out through the integration of previously DFN-derived equivalent permeability tensors, known injectivity tests and transient testing numerical simulations. Following this comprehensive

permeability assessment, a more detailed FLAC3D model – which includes injection-induced implications related to nearby injectors – is used to simulate conditions conducive to both tensile and shear failure during the subsequent April 2011, medium flow-rate stimulation phase. Results reveal that pore pressure diffusion to depths below the stimulation interval – especially under concurrent injection operations in injector 22-22 – can lead to pressurization and poromechanical stressing of the STF.

2.3 Manuscript III (pp. 93 to 154)

Title: Desert Peak EGS: Mechanisms Influencing Permeability Evolution Investigated through Dual-Porosity Simulator TFReact.

Status: imminent submission to Geothermics Elsevier EGS Special Issue.

In this study, hydraulic stimulation-induced reservoir responses and permeability modifications are modeled using the coupled THM(C) dual-porosity simulator TFReact, which combines FLAC3D's solid mechanics (M) analyses and TOUGHREACT's multiphase, non-isothermal and reactive capabilities (THC). The conceptualization developed as part of the previous studies is incorporated into this coupled model. All major stimulation phases from April 2011 to March 2013 are simulated to evaluate the relative impact of tensile vs. shear deformation on the observed reservoir permeability evolution (including on the STF). Simulated permeability modifications appear to be predominantly governed by thermo-hydro-mechanical dilation (elastic) during stimulation of the *shallow* interval and by hydro-mechanical deformation (inelastic shear) during stimulation of the *extended* interval. Shear deformation delivers higher permeability gains in the shortest time, only if hydraulically-conductive features well-oriented with respect to the stress field (STF) are targeted with the stimulation treatment. The simulator's reactive component (C) is not utilized, though it may be switched on at any time for further analyses.

3. MANUSCRIPT I - COMPUTATIONAL INVESTIGATION OF HYDRO-MECHANICAL EFFECTS ON TRANSMISSIVITY EVOLUTION DURING THE INITIAL INJECTION PHASE AT THE DESERT PEAK EGS PROJECT, NV

Stefano Benato[1,#], Donald M. Reeves[1], Rishi Parashar[1], Nicholas C. Davatzes[2], Stephen Hickman[3], Derek Elsworth[4], Paul Spielman[5], Joshua Taron[3]

1 - Division of Hydrologic Sciences, Desert Research Institute, Reno, NV, 89512 USA

2 - Temple University, Philadelphia, PA, 19122 USA

3 - U.S. Geological Survey, Menlo Park, CA, 94025 USA

4 - Pennsylvania State University, University Park, PA, 16802 USA

5 - Ormat Nevada Inc., Reno, NV, 89511 USA

Corresponding author: E-mail address: stefano.benato@gmail.com

ABSTRACT

The low-flow-rate injection phase of an Engineered Geothermal System (EGS) experiment in Desert Peak well 27-15 produced increased injectivity at wellhead pressures less than the minimum principal stress, consistent with hydraulically induced mechanical shear failure in the surrounding rock. We use statistical fracture analysis and hydro-mechanical modeling to simulate the observed pressure response during this shear stimulation, to explore one possible conceptual framework for the overall Desert Peak EGS experiment. This is part of a long-term study to

simulate the complete Desert Peak EGS stimulation, including both shearing and hydraulic fracturing (tensile) failure.

Discrete fracture network simulations, based on fracture/fault attributes measured downhole and at the surface, were used to derive equivalent permeability tensors for comparison with preferred fluid migration directions observed in hydraulic and tracer tests. FLAC3D, a hydro-mechanical simulator, was used to investigate changes in stress and displacement according to a Mohr-Coulomb frictional model subjected to perturbations in pore pressure. Although almost all of the seismicity observed during the EGS stimulation occurred during the high-flow-rate tensile stimulation phase, we use this seismicity to illuminate the geometry of large-scale geologic structures that could also have served as preferential flow paths during shear stimulation. This analysis shows that conditions for shear failure during the low-flow-rate shear stimulation could occur in locations consistent with locations of micro-seismicity observed during the tensile phase of the EGS experiment, providing a possible hydrologic connection between EGS well 27-15 and injection/production wells further south-southwest. This FLAC3D hydro-mechanical model will next be coupled to TOUGHREACT to investigate the near-field evolution of reservoir transmissivity associated with thermal, hydraulic, mechanical and chemical processes during all phases of the Desert Peak EGS stimulation.

1 INTRODUCTION

The goal of an Engineered Geothermal System (EGS) is to develop a complex and extensive flow path in hot, but low permeability rocks. The application of EGS at operating hydrothermal reservoirs is intended to convert dry or low-permeability unusable wells into operational injectors or producers, in an attempt to increase field productivity. To develop a complex flow path characterized by large surface area to rock volume ratios, as needed for optimal heat exchange, EGS experiments to date (e.g., Soultz-sous-Forêts, Desert Peak, Newberry, Habanero) have

typically used stimulation techniques that enhance the permeability of existing and naturally tortuous fracture networks generally found to be ubiquitous within the crust.

The Desert Peak geothermal field (Figure 1) is a successfully operating geothermal field with an approximate 23 MWe output located in the northern portion of the Hot Springs Mountains of northwestern Churchill County, Nevada, about 100 km northeast of Reno. Well 27-15 was selected to carry out a U.S. Department of Energy supported EGS project with the intent of improving the hydraulic connection with the rest of the reservoir and enhancing overall injectivity. Well 27-15 was originally drilled to a total depth of about 1771m. In 2010 it was back-filled to a total depth of about 1067m, with the completed open-hole section extending from 914m to 1067m to provide a short interval just below the casing shoe, but within the reservoir, to stimulate through hydraulic and chemical methods [2].

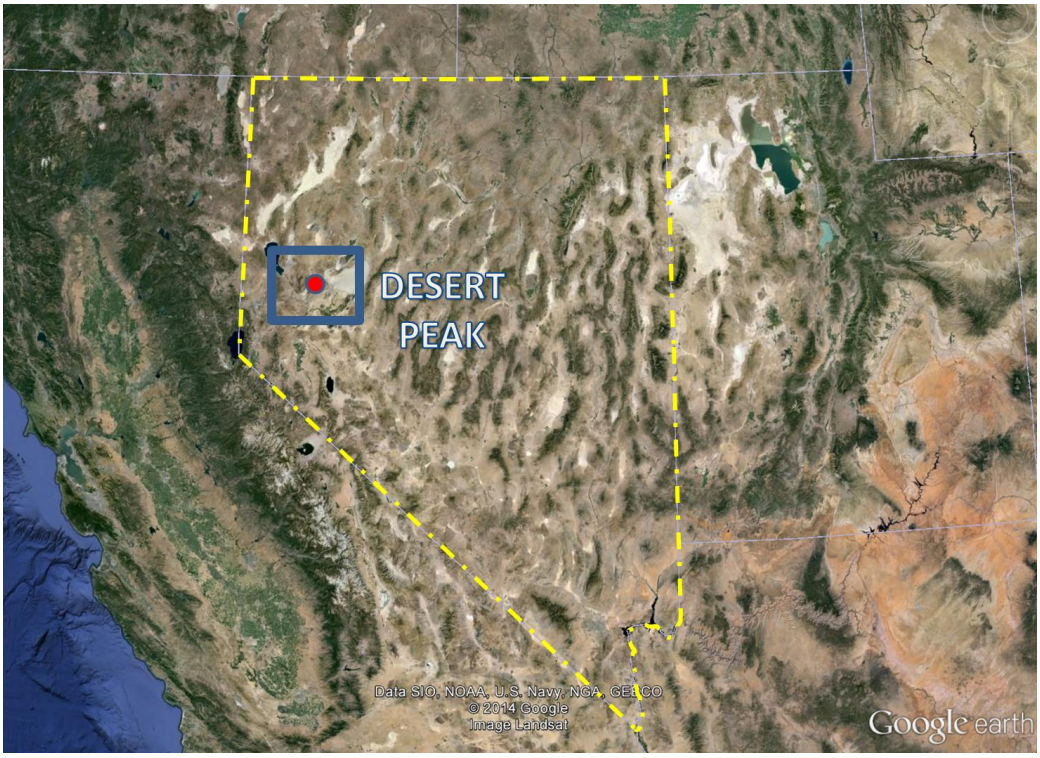

Figure 1 – Desert Peak Geothermal field location map.

Hydraulic stimulation carried out in Desert Peak well 27-15 from September 2010 through April 2011 led to a nearly 60-fold increase in injectivity [2]. This stimulation was carried under two different fluid pressure conditions relative to the least principal stress. An initial period of shear stimulation, which increased injectivity by more than one order of magnitude, from ~0.011 to ~0.15 gpm/psi, was carried out in a series of steps at low fluid pressures up to 4.5 MPa well head pressure (WHP). This maximum WHP was chosen to remain below the magnitude of the least horizontal principal stress (WHP ~5.2 MPa), as measured in this well just below the casing shoe by a mini-hydraulic fracturing test [15]. This low-flow-rate phase was immediately followed by a large-volume controlled hydraulic fracturing operation that lasted more than 23 days, which was carried out at high injection rates and WHP in excess of the least principal stress. This hydraulic fracturing stage resulted in an additional 4-fold increase in injectivity [2]. Temperature-Pressure-Spinner logs show that the injected fluid exited and stimulated well 27-15 at two primary locations: 1) the bottom of the open-hole section during the low-flow-rate injection phase and 2) the hydraulic fracture just below the casing shoe during the high-flow-rate injection phase.

During the EGS experiment, a total of 42 micro-earthquakes (MEQs) with magnitudes ranging from +0.10 to +0.74 were recorded between EGS well 27-15 and injection/production wells to the south-southwest, including in proximity to injection wells 21-2 and 22-22 (see Figure 2 and Figure 3) [2]. All but one of these MEQs occurred during the controlled hydraulic fracturing stimulation, with only one event (discussed below) occurring during shear stimulation. During all stimulation stages, the greatest injectivity gains are associated with the initiation or occurrence of these MEQs under either constant or decreasing wellhead pressure (Figure 4). This suggests that shear failure (i.e., faulting) resulting in the generation of MEQs is a key physical process controlling the evolution of transmissivity.

Variations in injection rate occurred in wells 21-2 and 22-22 at various times during the EGS stimulation, especially prior to the controlled hydraulic fracturing stage. In some cases, this

makes it difficult to establish a unique correlation between EGS operations and the observed seismicity. However, no significant variations in injection rate were occurring in wells 21-2 and 22-22 when the first MEQ was observed on Sept 17, 2010, during the low-flow-rate shear stimulation (Figure 4). As discussed below, this is one reason this stage of the Desert Peak EGS stimulation was selected for analysis in the present paper.

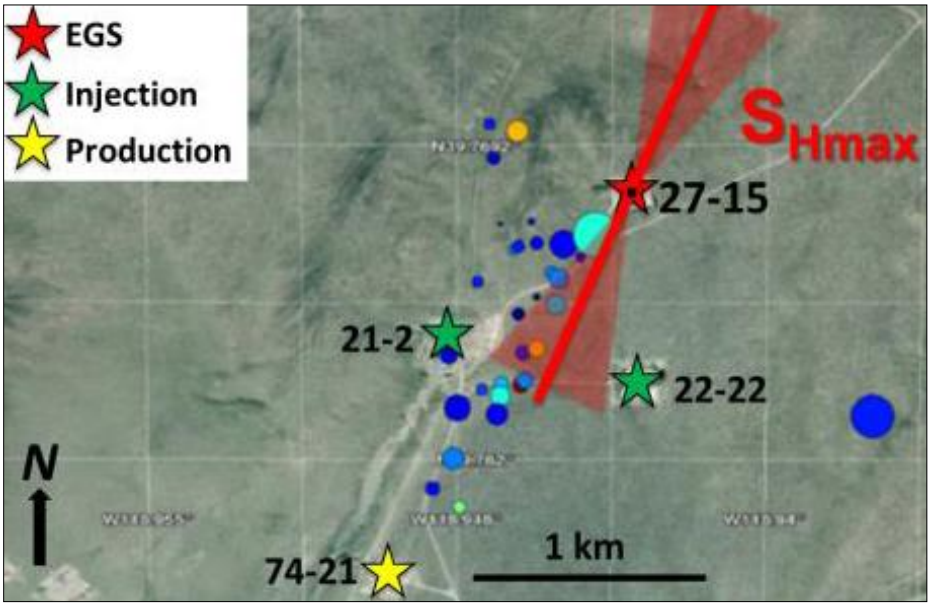

Figure 2 - Map view of the MEQs observed throughout the entire EGS experiment. The events are aligned with the direction of S_{Hmax} (Figure from [2]).

Poor focal sphere coverage and limited constraints on the seismic velocity model make it difficult to: (1) derive the exact source mechanism for these MEQs, (2) detect events smaller than magnitude $M_w < +0.1$ or (3) define the location of individual events with precision. Nevertheless, tensile failure produces relatively high frequency signals at the crack tip – typically of $M<<0$, which can usually only be detected with the use of specialized downhole instruments [34]. Thus, it is likely that the primary process generating MEQ events at Desert Peak is hydraulically-induced shear failure (Mode II-III) along pre-existing natural fractures and faults that are well-oriented for shear failure in the regional stress field (see [3] and [15]).

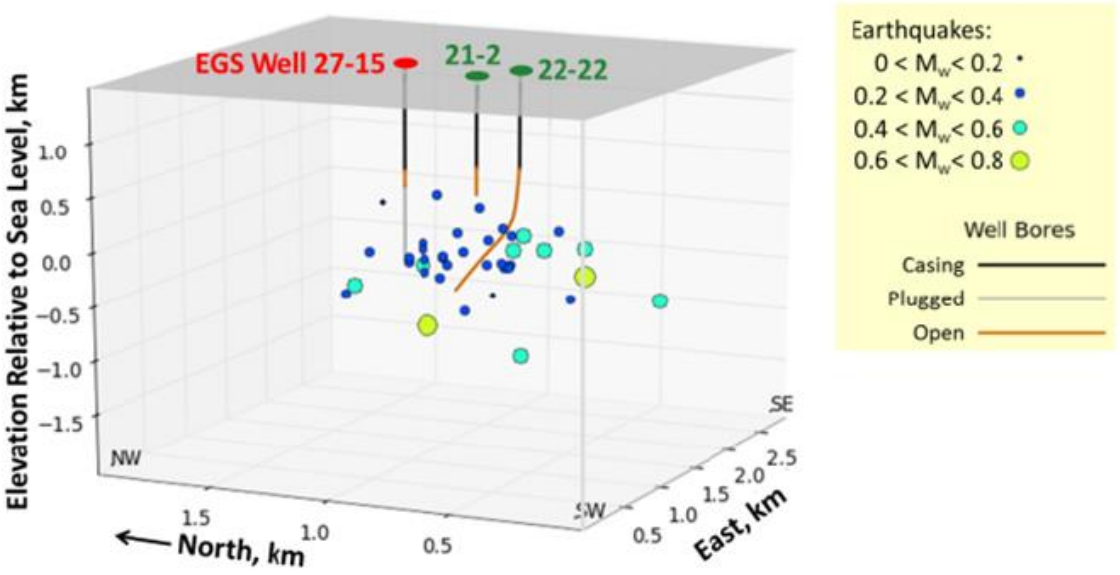

Figure 3 - 3D view of the 42 MEQs observed throughout the entire EGS experiment. The events appear to be clustered at about 1500m depth (Figure from [2]).

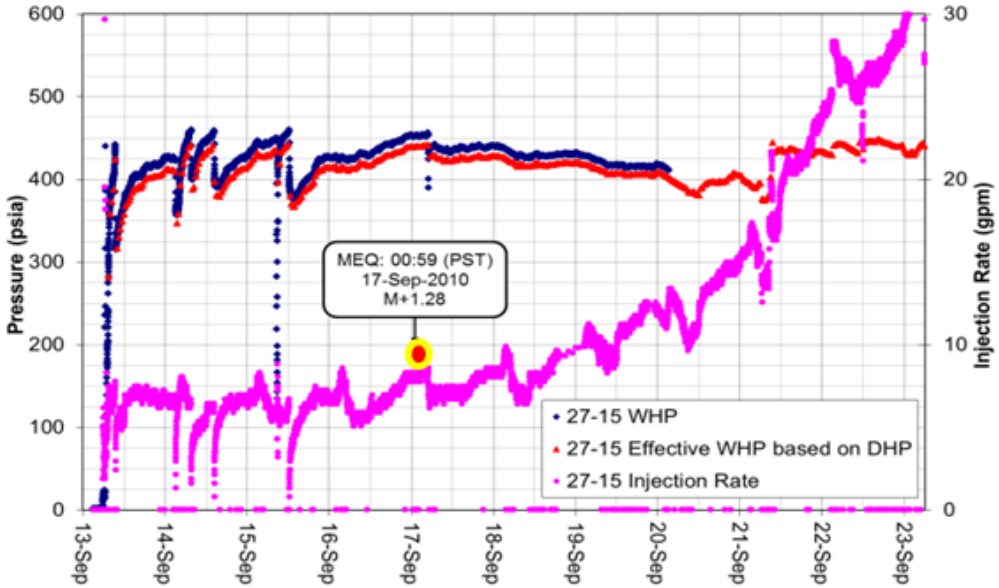

Figure 4 - Low-flow rate injection phase, Sept 2010: well 27-15 well-head pressure (WHP) and injection rate. The observed Sept 17 micro-earthquake (MEQ) occurs after about 4 days of injection and it is followed by a remarkable increase in the injection rate under constant wellhead pressure (Figure from [2]).

The first goal of this study is to identify any structure that may provide a high permeability conduit enabling connection to the rest of the field, and appearing to be spatially associated with MEQs during the various stimulation phases (all 42 MEQs).

The occurrence of MEQs at any stage of the injection phase is critical as: 1) most of the observed MEQs precede strong changes in injectivity during otherwise approximately constant WHP (indicating permeability development/enhancement); 2) The first, and lowest pressure phase of injection is associated with a single MEQ located below the injection interval, but approximately on the same population of MEQs observed during all stimulation phases. This MEQ also immediately precedes large gains in injectivity at near constant WPH in 27-15, which suggests a connection between fluid supplied from 27-15 and the MEQ, and that the MEQ along the flow path from 27-15 to the main field is one of many shear events that caused a reduction in resistance to flow (i.e., a gain in permeability) during the Sept 2010 low-flow-rate injection phase.

The second goal of the study is to numerically simulate whether fluid pressure changes at the location of this MEQ, in response to low-flow-rate injection into 27-15, are sufficient to cause frictional failure. This simulation utilizes: (a) injection rates into 27-15 during the low-flow-rate injection phase (when the single MEQ occurred), (b) a statistical characterization of the fracture population surrounding well 27-15, and (c) the effect on fluid pressure at the MEQ location due to concurrent injection into well 22-22 to the south. Note that the underlying proposition of this consistency test is that the MEQ is causally related to a subsequent change in injectivity. This is accomplished by simulating well-head pressure response during the Sept 2010 low-flow-rate EGS injection phase (Figure 4). The Sept 2010 stimulation phase is a good candidate for our initial model verification and calibration because: a) injection during this phase occurred at pressures below S_{hmin}, thus only shearing processes were involved, b) the injection rate climbs immediately after a single, yet significant, MEQ event and c) injection into nearby wells 22-1 and 22-22 was

relatively steady at the time this earthquake occurred, which also coincided with the onset of the pronounced injectivity gain observed in well 27-15 (Figure 4).

Thus, only shear failure is considered and modeled in this paper, as it is the only process occurring during the Sept 2010 injection phase. Tensile failure likely occurs during the subsequent medium to high-flow-rate hydraulic fracturing phases around the open-hole section of well 27-15 at Desert Peak. Such tensile failure is not addressed in this paper and will be part of a future study. Thermal stresses will also be considered in modeling all stages of the Desert Peak EGS stimulation at a later date.

The model presented in this paper is not unique but offers one possible explanation for the deep location of MEQs observed during the Desert Peak EGS stimulation. The observed MEQs seem to be influenced in a complex way by injection operations in both wells 27-15 and 22-22. Although we allow for some injection into well 22-22 in our modeling (see below), this issue is not addressed in detail here but will be addressed in detail in a future study.

2 RESERVOIR CONCEPTUAL MODEL

The Desert Peak geothermal field is located in the northern portion of the Hot Springs Mountains. Extensive drilling in the Desert Peak geothermal area has shown that the Hot Springs Mountains are mainly comprised of Tertiary volcanic and sedimentary rocks that lie directly on Mesozoic metamorphic and granitic basement [10][19]. Intrusive rocks below depths of 2134 m have intruded and contact-metamorphosed a Mesozoic sequence of marine metasedimentary and metavolcanic rocks between about 900 m and 2200 m depth. A Tertiary volcanic section that overlies the pre-Tertiary rocks can be broken into a lower rhyolitic unit composed primarily of ash-flow tuffs and an upper basaltic unit known as the Chloropagus Formation. The combined thickness of this volcanic package is between 760 m and 920 m. Overlying these volcanic rocks is a sequence of Pliocene, lacustrine sedimentary rocks known as the Truckee Formation, which is

up to 180 m thick in the vicinity of the wells. Quaternary alluvium and layers of windblown sand cover most of the surface area in the immediate vicinity of the well-fields [12]. The main Desert Peak reservoir resides in pre-Tertiary rocks [10] (Figure 5).

The Desert Peak geothermal field and the Northern Hot Springs Mountains lie within the NNE-trending Humboldt structural zone, which is orthogonal to the extensional direction of the Walker Lane. On a large scale, the Walker Lane is a system of dextral faults that accommodates ~20% of the relative motion between the Pacific and North American plates [8].

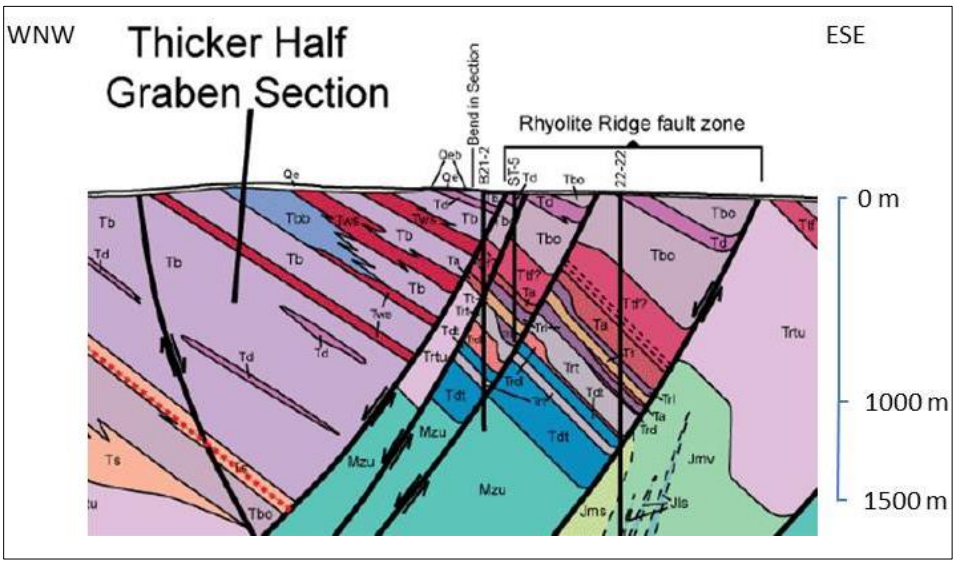

Figure 5 - Well 27-15 WNW-trending geologic cross section of the Northern Hot Spring Mountains. Unit abbreviations: Mzu, Mesozoic basement; Jmv, Jls, Jms, Jurassic metamorphic rocks; Trtu, Oligocene tuffs; Tdt, Trt, Oligocene ash-flow tuffs; Trdl, Oligo-Miocene rhyolite-dacite lavas; Trl, Oligo-Miocene rhyolite lavas; Tt, late Oligocene-early Miocene tuff; Ta, early to middle Miocene andesite-dacite lavas; Ttf, middle Miocene ash-flow tuff; Tbo, older basalt lavas; Tbb, basaltic breccia; Td, diatomite; Ts, lacustrine sediments; Tb, basalt lavas; Qe, eolian deposits. (Figure modified from [9]).

The dominant fault pattern trends about N25°E and appears to be related to Basin-and-Range tectonic stresses. The Humboldt structural zone may reflect both strain transfer and extension

related to the Walker Lane [10]. The most significant fault in the area is the WNW-dipping Rhyolite Ridge fault zone, which consists of several strands and steps to the left, in the vicinity of the Desert Peak geothermal field [9] (Figure 5 and Figure 6). NW-trending gravity contours across the Desert Peak field may reflect a relay ramp [18] associated with southward-increasing displacement on the Rhyolite Ridge fault zone [9]. Kinematic data gleaned from fault surfaces indicate dip-slip normal displacement on the NNE striking faults and a WNW-trending extension direction, which is compatible with: 1) regional extension directions inferred from geodetic data [13]; 2) borehole tensile failure data and stress magnitudes from a mini hydraulic fracturing experiment; and 3) rock densities consistent with a normal faulting stress regime from wells in the area [3][15] (Figure 6).

The most productive area in the system occupies left steps in the NNE-striking, west-dipping normal fault system. Although left stepping oblique- or strike-slip faults are not required for the localization of high permeability (i.e., interactions among normal-faults could also lead to dilatation and locally enhanced fracture permeability in this region) the potential for high fracture density in this step-over region could enhance permeability [9] (Figure 7) and is consistent with modeled slip on the Rhyolite Ridge fault [37].

Tracer test returns in production well 74-21 from injection in both 21-2 and 22-22 confirm strong hydraulic connectivity in the productive area of the field [32] (Figure 8). In contrast, tracer tests conducted by injecting in well 27-15 and sampling in well 74-21 show only modest connection between 27-15 and the rest of the reservoir [2].

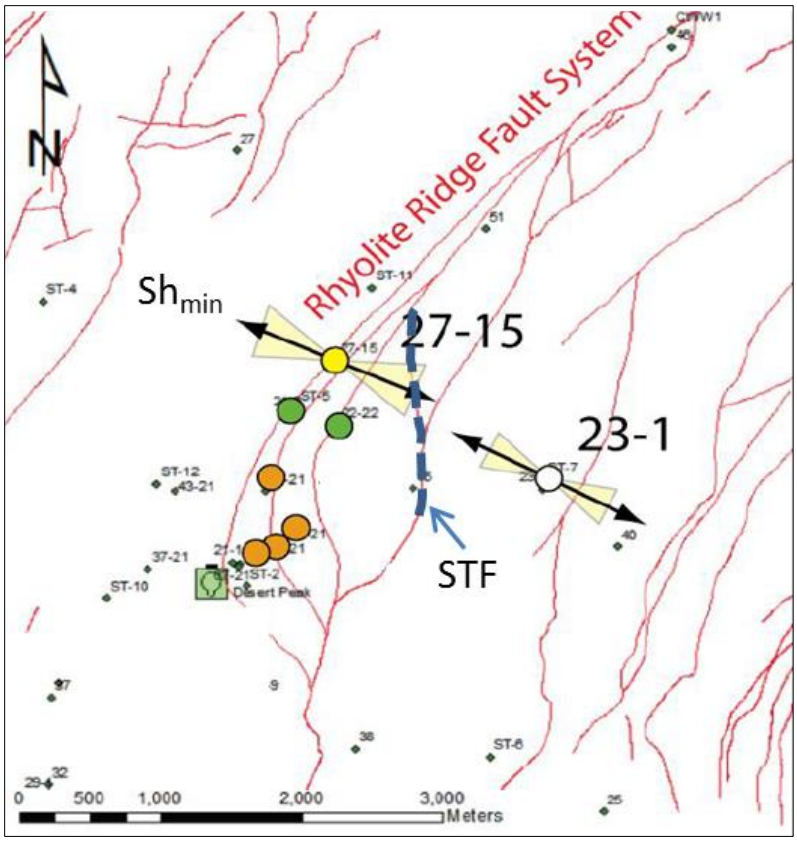

Figure 6 - Desert Peak Geothermal Field: a consistent orientation of S_{hmin} is inferred from observations of tensile fractures in wells 27-15 [3] and 23-1 [31]. Production wells are shown in orange, injectors in green, EGS well 27-15 in yellow (Figure modified from [37]). Surface trace of the Shearing Target Fault (STF, discussed below) inferred to intersect wells 22-22 and 27-15 at depth is also shown with a blue dashed line (see explanation below).

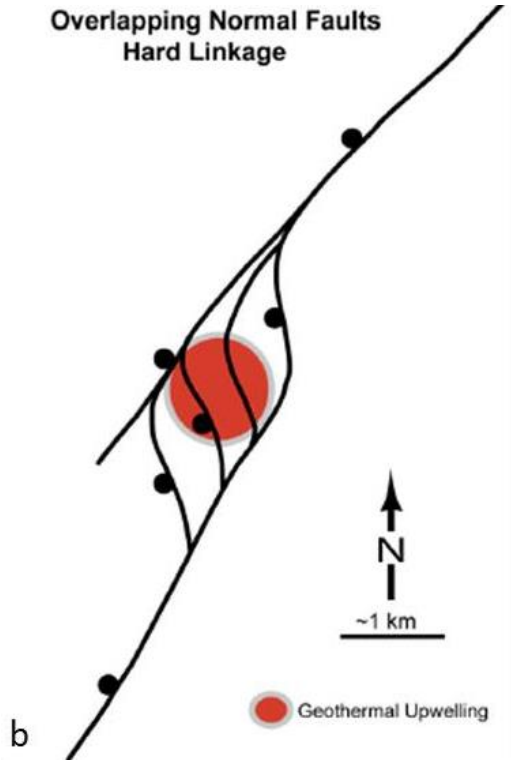

Figure 7 - Commercial permeability is encountered in the interpreted left-step of the Rhyolite Ridge Fault Zone [9], where production wells are located. Black dots are shown on downthrown sides of normal faults (Figure from [9]).

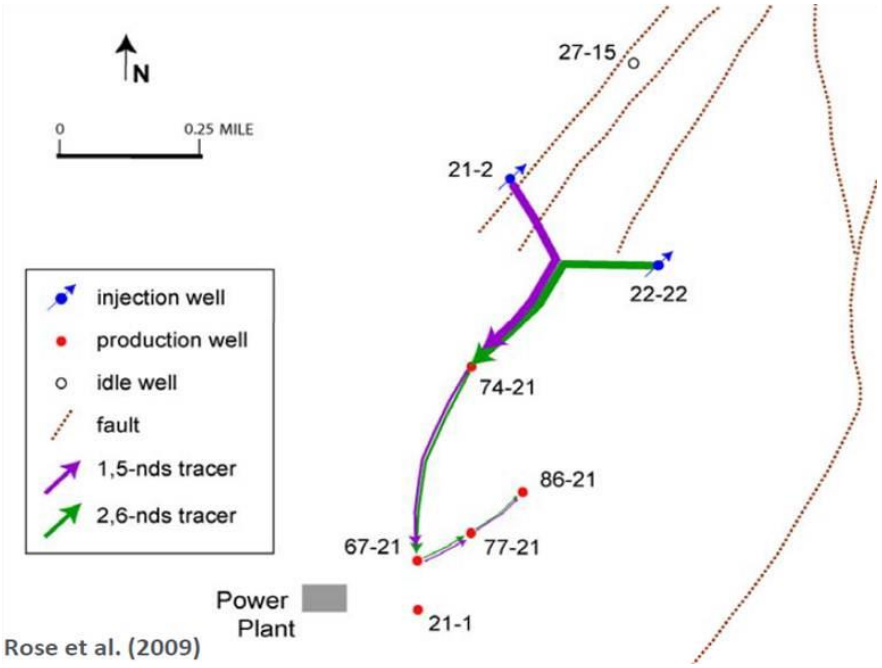

Figure 8 - Hydrologic connections (i.e., flow paths) inferred in 2009 by injecting tracers in injection wells 22-22 and 21-2 and sampling in production wells. Results show strong returns to nearest producer 74-21, and slower, weaker returns to other wells. Connection between reservoir and 22-22 occurs through base of Rhyolite Unit and STF (Figure from [32][7]).

Like many other fields, the volume of hot rock surrounding the Desert Peak geothermal field is far more extensive than the volume of hot *and* permeable rock. These circumstances have driven the need for an EGS experiment that can extend the reservoir into untapped hot rock to the north of the field, creating potential new injectors and increasing the residence time of the fluid.

Orientations of the horizontal principal stresses in well 27-15 were determined through analysis of drilling-induced tensile fractures visible in both high-temperature acoustic televiewer (ABI85) and formation micro-scanner (FMS) logs. These drilling-induced structures indicate that the azimuth of the minimum horizontal principal stress, S_{hmin}, is currently oriented 114 ± 17° (corresponding to a maximum horizontal principal stress of 024 ± 17°) [3]. Previous analysis of stress directions from borehole failure observed in well 23-1, located 2km E-SE of well 27-15, is

in excellent agreement with stress orientations inferred from well 27-15 [31], suggesting a regionally uniform stress field (Figure 2 and Figure 6).

A detailed 3D analysis of the EGS wellsite based on the geologic cross section and map introduced by Faulds et al., 2010 [9] (Figure 9 and Figure 11), suggests that EGS well 27-15 and injector well 22-22 encounter the same permeable horizon at about 1400 m depth, which is consistent with a moderate inter-well connection revealed by pressure interference testing (Figure 10) [40] and TPS logs [3].

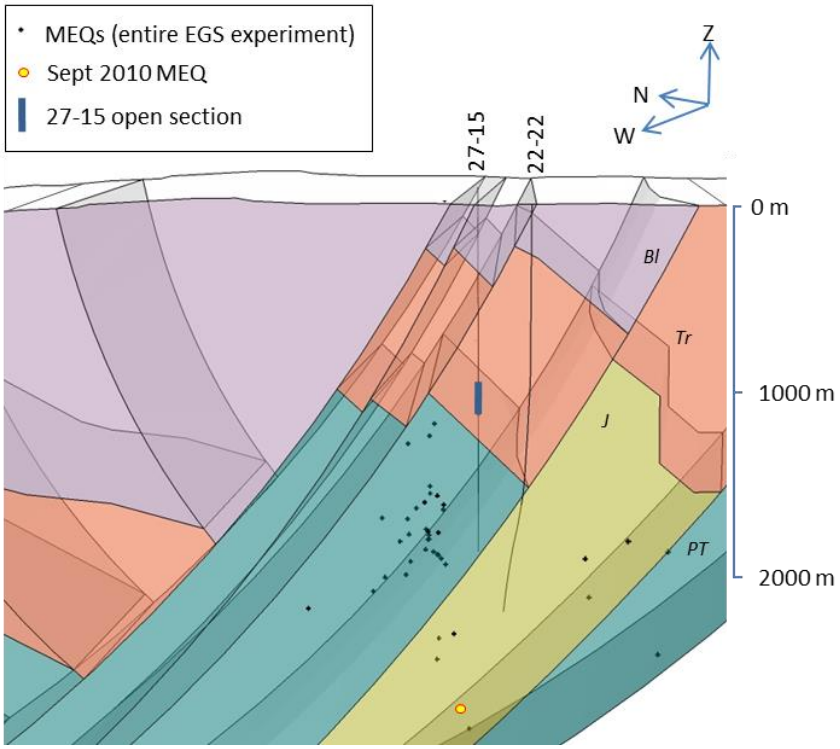

Figure 9 – Three-dimensional geologic model of EGS wellsite, derived from the geologic cross section and map of Faulds et al., 2010 [9], but with lithology simplified and grouped into fewer units to facilitate conceptual modeling and numerical simulation. Clustering of MEQs (shown from entire EGS experiment) mostly occurs within the Mesozoic and Jurassic metamorphic basement at depth. Unit abbreviations: J, Jurassic metamorphic basement; PT, Pre-Tertiary basement; Tr, Tertiary lavas and ash-flow tuffs; Bl, basalt lavas.

This horizon is the projection at depth of one of the main Rhyolite Ridge Fault Zone structures mapped at the surface, the Shearing Target Fault (discussed below; see Figure 12 and Figure 6), which is also approximately parallel to S_{Hmax}. This fault is near a dense cluster of MEQs associated with injection into well 27-15 and increases in injection rate that were occurring at about the same time into well 22-22.

The temporal association of high-pressure injection into 27-15 during the controlled hydrofrac phase and this cluster of seismicity suggest that the EGS stimulation caused some of this seismicity. However, concurrent increases in the injection rate into well 22-22 immediately before high-pressure injection makes it difficult to establish a unique causal link between most of this seismicity and the EGS stimulation. Also, this seismicity occurs at a depth of 1400 to 1600 m, which is significantly below the interval of fluid egress from well 27-15 at a depth of ~914 m [2] (Figure 9). At 1400 m depth, significant fluid loss associated with large-aperture fractures is observed in the deeper section of well 27-15 [3]. Also, in well 22-22, an active injection well located ~400 m south of 27-15, major feed zones are found at depths of 790 m and 1340 m.

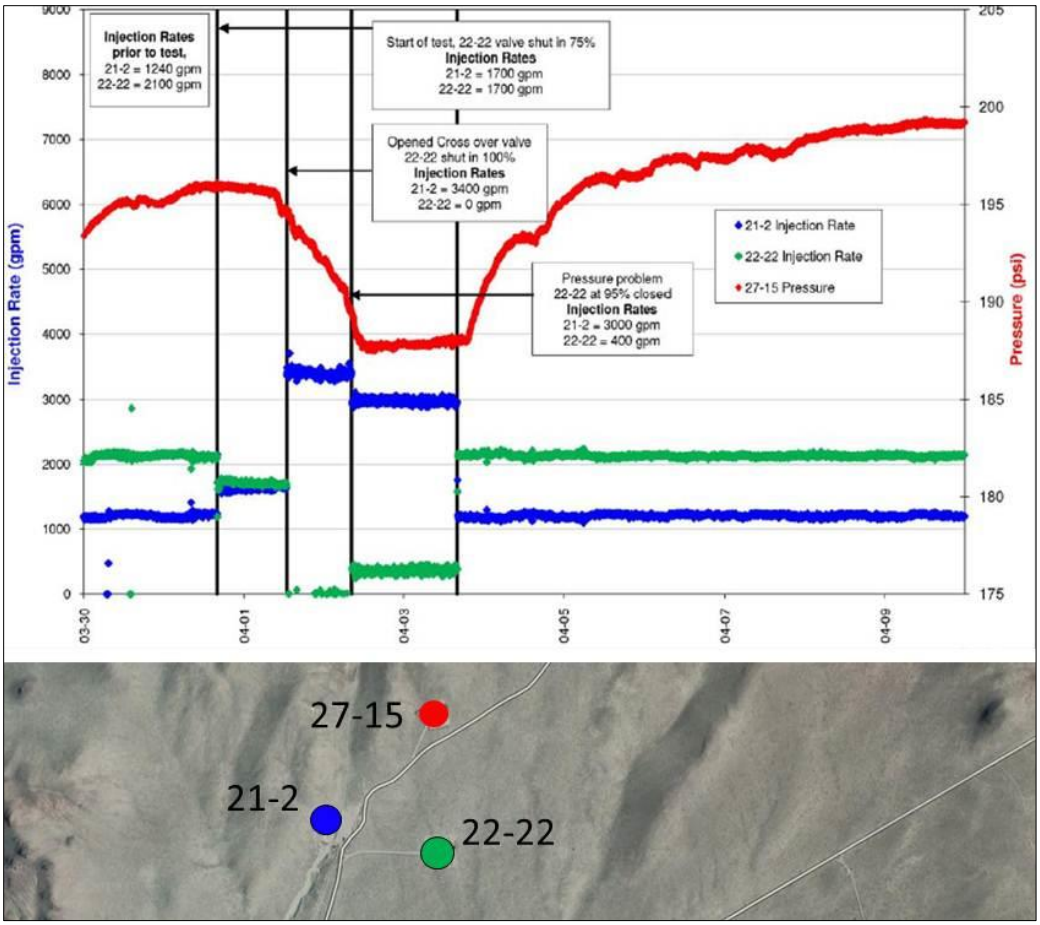

Figure 10 - Transient testing conducted by altering injection rates in wells 22-22 and 21-2 while observing pressure response in well 27-15. The test shows that well 27-15 is weakly but mainly connected with well 22-22 (Figure modified from [7]).

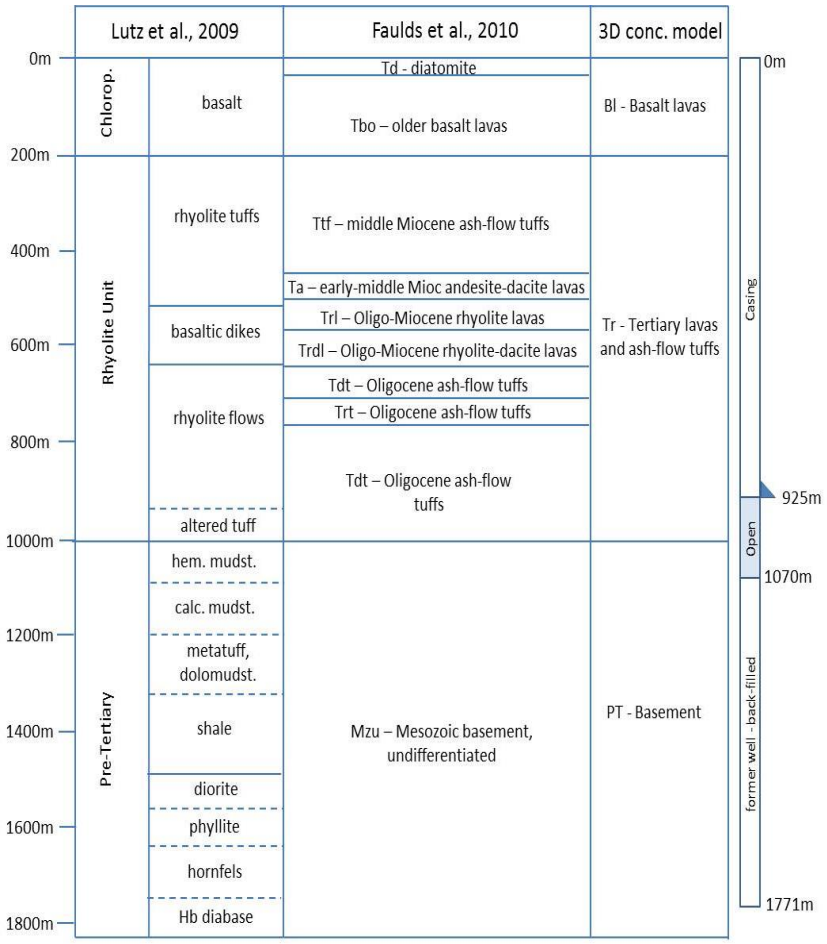

Figure 11 - Lithology correlations between available Desert Peak geological models and simplified lithological grouping used for the 3D conceptual model of the wellsite (Figure 9). Well 27-15 schematic diagram is also shown.

Weak connectivity between wells 27-15 and 22-22 is confirmed by transient hydraulic testing (Figure 10) [7], and may be occurring through these deeper fluid loss/feed zones.

Thus, a major NNE-SSW striking and WNW dipping segment of the Rhyolite Ridge Fault Zone might extend between wells 22-22 and 27-15 and establish a cross-formational hydraulic connection between these two wells (Figure 12). This structure appears to represent a preferential flow path for fluids circulating in its vicinity, in addition to being well oriented for shear failure in the current stress field [15] [37]. However, if this structure played a role during the EGS

stimulation – as suggested by the deep seismicity observed during both the low – and high-pressure stimulations - a hydrologic connection must have been established between the shallow stimulation interval in well 27-15 and this deeper fault zone. Pressure transient tests (discussed above) indicate that pumping in 22-22 could also contribute to pressurization of this structure (Figure 10), supporting the idea that injection rate changes into well 22-22 just prior to high-pressure (controlled hydraulic fracturing) stimulation might also have contributed to this deep seismicity. The tracer tests suggest that permeability along this structure decreases northward of the injectors (Figure 8), or with increasing distance from the most productive area in the field [32].

Based upon the deep seismicity observed, we propose that this fault segment might have played a significant role in all stages of the EGS stimulation. One purpose of the modeling presented here is to test this hypothesis to see if it is consistent with known structural and stress characteristics of the EGS site and with the pressure response observed during low-flow-rate (shear) stimulation. For simplicity, this fault-segment will be referred to as "STF" (Shearing Target Fault) throughout the paper (Figure 12). This conceptual model for a deep hydrologic connection between well 27-15 and wells to the SSW provides the basis to test potential mechanisms controlling permeability development during the Desert Peak EGS experiment. In particular, both the clustering of microseismicity (including the single event associated with shear stimulation) and the inferred location of the STF are ~400 m deeper than the open-hole section stimulated in well 27-15. Yet, migration of injected fluid from the formation surrounding this open-hole section toward the deeper STF might have been facilitated by existing well-oriented fractures. In this scenario, the resulting transmission of hydraulic pressure increase within the STF is presumed to have triggered shear failure of sufficient magnitude to result in observable MEQs, enhancing permeability and fluid pressure transmission along the STF.

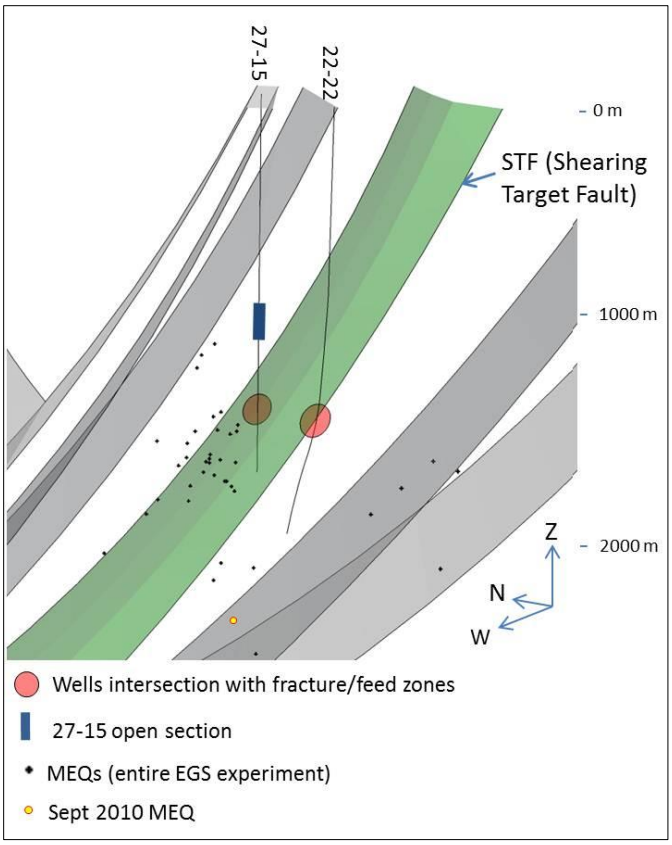

Figure 12 - Conceptual model of the major fault strands of the EGS wellsite (inferred from the geologic cross section and map introduced by Faulds et al., 2010 [9]). The three-dimensional geometry allows for a visualization at depth of MEQs (which occurred over the course of the entire EGS experiment) with respect to the structural setting. Both wells 27-15 and 22-22 encounter a highly-fractured and permeable horizon (Shearing Target Fault "STF") at about 1400m depth. Most of the MEQs recorded throughout the course of the EGS experiment are clustered at about 1400 m-1600 m depth, which coincides with the approximate projection at depth of the STF.

The single MEQ observed during the Sept 2010 phase is located deeper than the main cluster of MEQs observed throughout the entire EGS experiment (Figure 12). However, taking into account significant vertical errors on the order of hundreds of meters for this specific event, the most likely structure which generated the Sept 2010 MEQ remains the STF, which: is independently

identified from geological evidence; is known to contain some permeability from previous hydraulic tests; is also associated with other deep MEQ events during latter stimulation phases.

3 TECHNICAL APPROACH

We investigate whether or not the above conceptual model is consistent with observations made before and during the Desert Peak EGS stimulation by applying statistical and numerical methods to ascertain: 1) the connectivity, attitudes, and hydraulic apertures of pre-existing natural fractures controlling fluid circulation around the EGS stimulation interval, and 2) the potential for initiating shear failure due to fluid over-pressurization that reduces effective normal stress and thus frictional resistance to slip within the STF. This is accomplished through a combination of discrete fracture network (DFN) and hydro-mechanical modeling techniques.

3.1 Discrete Fracture Network Modeling

The study of fracture networks is typically restricted to small, localized sample volumes, and often simplified to 2D. These approaches can provide useful models of the actual fracture network, however, by deriving probabilistic descriptions of fracture location, attitude, spacing, length and aperture from borehole fracture data. The data set measured by *Davatzes and Hickman, 2009* [3] from FMS and ABI85 image logs in well 27-15 is used to generate a representative statistical fracture network to simulate the corresponding fluid flow in the rock volume containing the well. This fracture population spans the interval from 926 m to 1705 m, and thus extends beyond the limited stimulated open-hole interval (916 m to 1067 m). This allows us to probabilistically assess the fracture population that extends from the stimulation interval to the STF, which is presumed to host the hydrologic connection. The data set consists of a total number of 567 fractures with associated measured and true vertical depth, attitude (dip and dip direction), apparent aperture (i.e., thickness at the borehole wall in the image logs), and a ranking of the reliability of the fracture identification as well as an assessment of the quality of the image

log. The latter provides insight into whether variations in fracture density are related to changes in the fracture population or simply to the quality of the image log [3]. Fractures with immeasurably thin apparent apertures (typically the lowest quality picks), or with a <45° dip angle (probable bedding planes [9] with no preferred orientation) are not considered in this statistical fracture analysis, as they are less likely to contribute to fluid flow. This results in a total of 261 discrete fractures sampled over a length of 778m to yield a fracture frequency of 0.3 fractures/m and an average fracture spacing of 3 m. Table 1 shows the statistical analysis results for the two identified main fracture clusters, with the remaining 29.1% of fractures randomly distributed.

These two antithetic fracture sets are in agreement with structures observed at the field scale. In particular, the principal Cluster 2 is consistent with the main NNE-striking, WNW-dipping Rhyolite Ridge Fault Zone (Figure 13).

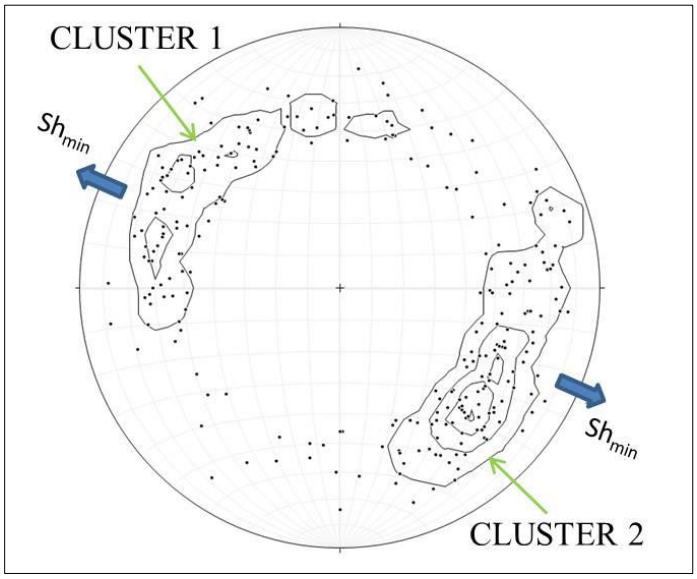

Figure 13 - Lower hemisphere, equal area stereographic projection of poles to natural fractures used as input for the DFN simulation (from analysis of image logs along the entire sampled well [3]). Fractures with negligible apparent aperture or with a < 45° dip angle are not shown since not considered in the analysis. The identified clusters show agreement with the observed stress field [15].

Table 1 - fracture network statistical parameters.

	CLUSTER 1	CLUSTER 2
Quantity	71	114
Cluster Probability	27.2 %	43.7 %
Mean Strike	28.6°	205.9°
Mean dip	58.0°	58.4°
kappa	16.9	12.0

The apparent apertures of fractures imaged in well 27-15 represent intervals of reduced resistivity at the borehole wall in the case of FMS images, and in the case of ABI85 images correspond to intervals in which the reflected acoustic pulse is scattered by irregularities in the borehole surface. Apparent aperture values range from millimeters to centimeters and are more representative of fault core thickness [35] than mechanical or hydraulic aperture, which are typically expected to be on the order of microns [22] [4]. Given the limitation of image logs to directly measure hydraulic aperture, we adopt a scaling approach that combines the total number of flowing fractures identified by temperature/spinner anomalies [3] with the permeability-thickness value measured during hydrologic tests to estimate the hydraulic fracture aperture [28].

Temperature/spinner anomalies show evidence of 28 flowing fractures along the entire sampled length (778 m), 8 of which are along the stimulated open-hole section of the well (152 m) [3]. Along the same open-hole section, a permeability-thickness of 60 mD-ft was determined [36], yielding an average permeability of 1.2e-16 m^2, a hydraulic conductivity of 4.7e-09 m/s (using reservoir fluid properties for a measured temperature of 120°C: fluid density ρ=948.7 kg/m3, fluid viscosity μ=2.35e-04 Pa-s) and a corresponding average transmissivity of 7.1e-07 m^2/s. Considering 8 flowing fractures along the current open-hole section of the well, the equivalent

average transmissivity T per flowing fracture becomes 8.9e-08 m^2/s. By applying the cubic law, $b = (12\mu T/\rho g)^{1/3}$, the mean hydraulic aperture b is therefore 30 μm.

Borehole data is also limited by the inability to directly measure fracture length, which is critical to assessing the connectivity of fracture networks. In the absence of reliable data relating fracture length to either mechanical aperture for tensile (Mode I) fractures or slip for shear (Modes II, III) fractures [33], fracture length is assumed to be distributed according to a power-law: $P(L > 1) = Cl^{-a}$, where the power-law exponent a typically ranges from 1 to 3 in naturally-fractured rock masses (e.g., [1] [30]) and C is related to the minimum fracture length. A power-law exponent of a=2, corresponding to the approximate average of power-law exponents measured in the field [30] was selected to represent fracture length in the DFN model. Fracture networks with a=2 consist of an approximately even mixture of short and long fractures [6][14][26][27]. The resulting fracture lengths are then scaled to the fracture heights using a relationship defined for normal faults in layered sequences [23]: $H = \frac{L}{2.2}$, where H and L are the fault height and length, respectively.

From the fracture analysis described above, a three-dimensional DFN is reproduced [29] where fractures are seeded as: 1) fracture location via a random point process, 2) orientation via a Fisher distribution consistent with prior probabilities for each set, 3) fracture lengths by input of the a=2 value through a Pareto distribution truncated to censor extreme values greater than 200 m; and 4) a lognormal distribution of fracture transmissivity. The 3D DFNs are then projected onto 3 planes (orthogonal to each other) aligned with the Cartesian coordinate system for computation of the conductivity tensor. The lognormal distribution of fracture transmissivity is derived from fracture aperture as follows. Only 8 of 261 fractures (~3%) were found to be significantly conductive, which we define as having a hydraulic aperture greater than 100 μm from the well-test analysis presented above. Using a mean fracture aperture of 30 μm derived from the well hydraulic test,

fracture variance is changed so that approximately 3% of the fractures have an aperture greater than 100 μm. The upper and lower bounds of the distribution are then censored to avoid computational problems with apertures being too small (< 2 μm) and to retain realness by not allowing apertures to be unreasonably large (>500 μm). This censoring affects less than 1% of all generated aperture values.

In order to compute a permeability tensor representative of the background natural fracture population, a 3D DFN was first generated until the fracture frequency of 0.3 fractures per meter derived from image log analysis was achieved within the DFN 200 m × 200 m × 200 m domain (computed along multiple scan lines), followed by projection of these fractures onto three 200 m × 200 m orthogonal planes aligned with the Cartesian coordinate system: *x*-*y*, *y*-*z*, *x*-*z*. Discrete fracture networks are analyzed for intersection with three fracture types: all fractures, hydraulic backbone fractures, and dominant fractures. "All fractures" refer to all fractures present in a rock mass, whereas "hydraulic backbone" fractures refer only to the interconnected fractures of the hydraulic backbone. The fracture backbone is thus computed for each Cartesian plane by eliminating dead-end segments and isolated clusters, as these cannot contribute to transmissivity. Two configurations of linearly decreasing head conditions are applied to compute each permeability tensor component, and flow is then solved iteratively via a biconjugate gradient method under specific boundary conditions at all internal nodes according to Darcy's law [5][17][25][28][24].

3.2 FLAC3D Fluid-Mechanical Response Model

The conceptual model is tested against the September 13 to 23, 2010, low-flow-rate injection phase (Figure 4) by numerical simulation with the mechanical-flow code FLAC3D.

FLAC3D is a three-dimensional explicit finite-difference program for continuum mechanics computation which also models fluid flow and its corresponding poromechanical effects. [11]

This simulation consists of two successive stages: (1) hydraulic-only computation of pressure gradients generated between the STF and the stimulation interval during fluid injection, and (2) a hydro-mechanically coupled calculation to estimate the mechanical deformation in response to increased hydraulic pressure within the STF, where changes in pore pressure generate deformation, and volumetric strain causes pore pressures to evolve.

As mentioned above, the simpler characteristics of the September 2010 phase make it a perfect candidate for model verification and calibration for subsequent simulation of more complex injection phases, given that: a) injection during the Sept 2010 phase occurs at pressures below S_{hmin}; and b) the injection rate climbs immediately after detection of a single, yet potentially significant, MEQ event. This suggests the process triggering the MEQ event plays a primary role in transmissivity development during this phase. The timing at which this single MEQ occurred represents a perfect reference for model calibration as it defines the diffusion time required by the hydraulic pressure to build-up to a value critical for triggering mechanical deformation (i.e. shear failure) in the rockmass. Therefore, we tune the model of pressure diffusion through the fracture network between the open-hole interval in 27-15 and the location of the MEQ, presumed to be on the STF, to determine the model parameters/conditions necessary to cause an MEQ 4 days after the initiation of injection into 27-15 at WHP fluid pressures of ~3.2 MPa. In this case, pressure sufficient to reduce effective normal stress must be communicated to the STF in order to satisfy the conditions for Mohr-Coulomb failure. The 27-15 Sept 2010 low-flow-rate injection is used to verify these conditions.

As introduced above, injection into 27-15 is not the only source of pressure perturbation in the studied area. Injection into 22-22 has also a potential connection to this volume, and flow was varied into this well during the EGS experiment. However, during the Sept 2010 low-flow-rate phase, fluid from 22-22 was transferred to 27-15, and thus injection in 22-22 consisted of about half the rate injected in 27-15, at approximately four times less than the 27-15 injection pressure.

In addition, this MEQ occurring approximately 4 days after the initiation of injection is a good reference when calibrating the model, as it represents the time over which the hydraulic pressure diffusion process builds up and triggers the shear mechanism. The 27-15 low-flow-rate phase allows for a sensitive and accurate calibration of the pressure gradient throughout the STF zone. Finally, influence from injection operations in well 22-22 is limited during this phase, consisting of about half the rate injected in 27-15, at approximately four times less than the injection pressure.

For both simulations, and as a general rule, the simplest possible geometry option is used to define the FLAC3D model, consistent with the reproduction of key physical processes. In the simplified representation of the wellsite, the model comprises a low permeability background formation, two injection points (wells 27-15 and 22-22) and a NNE-striking fault zone (STF) about 100m thick, dipping 70° WNW and located about 500m below the actual 27-15 injection point. The model domain extends for 3000 m in the x-direction, 700 m in the y-direction and 2600 m in the z-direction. The grid is discretized into regular cubic zones 100 m on a side. The STF - like the rest of the model - is currently assumed to be a fluid-saturated single-porosity media. Later modeling exercises involving coupling with TOUGHREACT may adopt a dual-porosity conceptualization.

A phreatic surface is initialized at 118 m depth, below which pore pressures have a constant gradient once the initial force-equilibrium state is reached. (in FLAC3D, force-equilibrium is assumed when the maximum unbalanced force and velocity vectors at each gridpoint are small compared to the representative zone forces in the problem). Realistic hydraulic conditions typical of a fractured reservoir are represented in the model by anisotropic permeability. For numerical purposes, the lithological units described in Section 2 are grouped into rock types (a) through (c) as: a) corresponding to both the basement and the rhyolite units and representing the background

rock mass; b) simulating the rock behavior in the vicinity of the open-hole section of the well, and c) representing the STF.

The permeability assigned to the formation surrounding well 27-15 in the FLAC3D model is guided by the DFN equivalent permeability tensors computed from site-specific fracture attributes. A higher vertical permeability (k_z) is used to simulate an assumed vertical connection between the open-hole interval of 27-15 and the underlying STF (rock type b). The highest permeability values are assigned to the STF, within which both the vertical and horizontal tensors vary according to a prescribed gradient between well 27-15 (STF north end) and well 22-22 (STF south end) (*Table 3*). The STF permeability gradient is being assigned and adjusted by calibration against: 1) instantaneous downhole pressure in well 27-15 and 2) pressure transient testing carried out between wells 27-15 and 22-22.

The low background permeability of the formation guarantees that fluid flows preferentially through the STF and eventually exits the model to the south, toward the productive area of the field. The model is set by using permeable boundary conditions (i.e., the pressure is set to remain constant at the boundaries of the model after the initial equilibrated pressure is reached). Velocity and displacements are fixed at the bottom and sides of the model (i.e., no velocity or displacement is allowed at the selected gridpoints).

Consistent with the normal faulting regime observed in the field and using the measured magnitude of S_{hmin} [15], xx, zz and yy stress components vary with depth following the relations between S_{hmin}, S_{Hmax} and S_v (vertical overburden): $S_{Hmax} = (S_{hmin} + S_v)/2$ [15]. A Mohr-Coulomb plasticity constitutive model is used in FLAC3D to properly represent the onset of shear (frictional) failure. The failure envelope for this constitutive model corresponds to a Mohr-Coulomb criterion (shear yield function with tension cutoff) which is expressed in terms of principal stresses σ_1, σ_2 and σ_3. For the Mohr-Coulomb plasticity model, the required properties defined for each material are: 1) bulk and shear moduli; 2) friction and dilation angles; 3)

cohesion; and 4) tensile strength. The constitutive behavior and associated material properties dictate the type of response the model will display upon disturbance by the injected fluid [11].

The mechanical parameters used in the model are derived from rock mechanical tests conducted on selected core samples representative of the stimulation interval in well 27-15 [20]. Mechanical properties for the Rhyolitic and Metamorphic Basement Units are averaged and assigned to rock types a, b and c. A lower friction angle of 22° is used for rock type c (Table 2). The latter is also set with zero cohesion, as in-situ stress measurements in a variety of tectonically-active geologic settings suggest that fracture planes well oriented with respect to the stress field are generally cohesionless [14][39].

Table 2 - Mechanical properties used in the FLAC3D hydro-mechanical model.

	Rock type a, b	Rock type c
Density [g/cm^3]	2.5	2.5
Shear Modulus [MPa]	1.0E+04	1.0E+04
Bulk Modulus [MPa]	1.7E+04	1.7E+04
Friction angle [°]	39.1	21.0
Cohesion [MPa]	20.6	0
Tensile strength [MPa]	1.0E+04	1.0E+04

Boundary and initial conditions define the *in-situ* state (i.e., the condition before a change or disturbance is introduced by injection). After these conditions are defined in FLAC3D and the initial equilibrium state is calculated for the model, an alteration is made (e.g., a change in pore pressure at selected points), and the resulting model response is computed. For both hydraulic-

only and hydro-mechanical simulations, a prescribed volumetric inflow of fluid varying with time is assigned to define the principal fluid sources in the model (wells 27-15 and 22-22).

Table 3 - Anisotropic permeabilities used in FLAC3D.

Rock Type	kx [m^2]	ky [m^2]	kz [m^2]
a	1.4e-16	1.4e-16	7.2e-18
b	1.9e-17	1.9e-17	7.0e-17
c (27-15 end)	7.0e-18	1.0e-17	1.9e-14
c (22-22 end)	7.0e-16	2.3e-14	9.4e-17

An average volumetric flow rate of 5e-5 m^3/s is applied to the gridpoints corresponding to the open-hole section in well 27-15. At the same time, an average volumetric flow rate of 2.5e-5 m^3/s is applied to the gridpoints corresponding to the two feed zones in well 22-22: 60% of the injected fluid is prescribed to the deep feed zone (basement), while the remaining 40% is applied to the shallower feed zone (rhyolite), which is consistent with temperature-pressure-flowmeter logs run in this well.

4 RESULTS

4.1 Discrete Fracture Network Modeling

Figure 14a provides a 3D representation of the discrete fracture network generated using the procedure described above from the site-specific statistics in well 27-15. The 3D DFNs are projected onto planes aligned with the Cartesian coordinate system for computation of the conductivity tensor. 2D illustration of the relative contribution to flow among fractures on the x-z plane is shown in Figure 14b. The DFN correctly reproduces the regional structural trends observed at the field scale from surface mapping, the fracture attitudes from borehole

observations, as well as the density of hydraulically-conductive fractures (i.e. 4/100 m) identified from TS anomalies in the borehole log data [9]. Geometric and flow techniques eliminate dead-end segments or isolated clusters, and identify the hydraulic backbone representing the interconnected subset of fractures responsible for conducting flow across the model [26][27]. By computing hydraulic conductivity from fracture apertures according to the cubic law for each principal direction (x, y and z), a total of 40 simulations of fluid flow through the generated DFN provide the following horizontal (k_x=east-west, k_y=north-south) and vertical (k_z) average equivalent permeabilities comprising, for the volume containing well 27-15, the permeability tensor k_x=2.50-17 m^2, k_y=1.83e-16 m^2, k_z=6.16e-17 m^2 respectively. The resulting permeability magnitude k is equal to 1.94e-16 m^2. Despite the lack of calibration of the DFN simulations to the measured permeability to date (i.e., only the permeability distribution is conditioned to general observations from hydraulic testing), the results are in very good agreement with the on-site measured permeability of 1.2e-16 m^2 for the formation surrounding the open-hole section of the well [36].

The results emphasize preferential flow through k_y and k_z relative to k_x, in accordance with the trends of the major structural features. The existing natural fracture network supports vertical fluid flow and represents a preferential pathway through which injected fluids can reach greater depths.

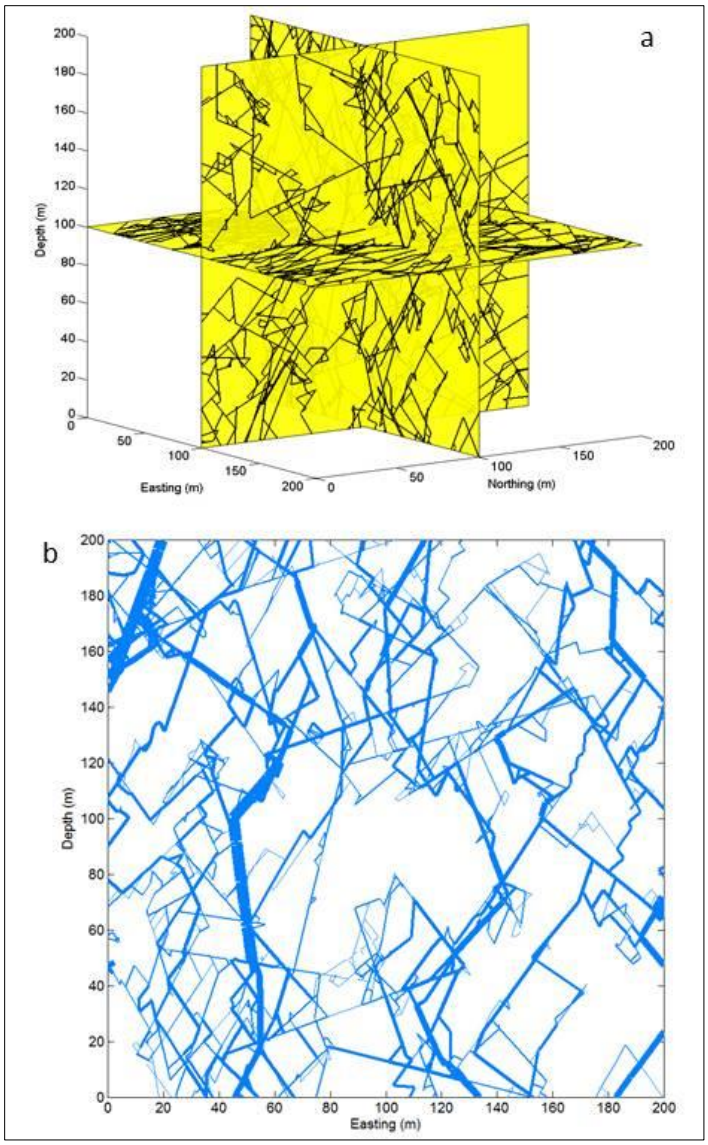

Figure 14 - a) Site representative 3D fault network mapped onto three orthogonal planes of a Cartesian coordinate system along with b) fault network projected onto x-z plane with line thickness proportional to flow. Only interconnected fault segments of the hydraulic backbone are shown. Note that the frequency of higher permeability fractures is consistent with that encountered in well 27-15 (i.e., approximately 7 fractures over a 200 m vertical length).

4.2 FLAC3D Modeling

In the first set of simple models, only fluid diffusion along fractures in a rigid rock mass was considered. The computationally-simpler hydraulic-only model was necessary in the first stage to estimate if a pressure gradient/incremental could be generated between the STF and the stimulation interval under the Sept 2010 injection phase conditions. The resulting computed pressure incremental was then analytically tested against a Mohr-Coulomb analysis to verify if the resulting pressure incremental could satisfy conditions for shear failure on well-oriented sets of fractures.

Under the prescribed conditions, the FLAC3D hydraulic-only (no deformation in a rigid rock mass) simulation shows that fluid diffusion throughout the STF generates a maximum pressure increase of ~1.8 MPa within the STF after about 4 days of injection (Figure 15).

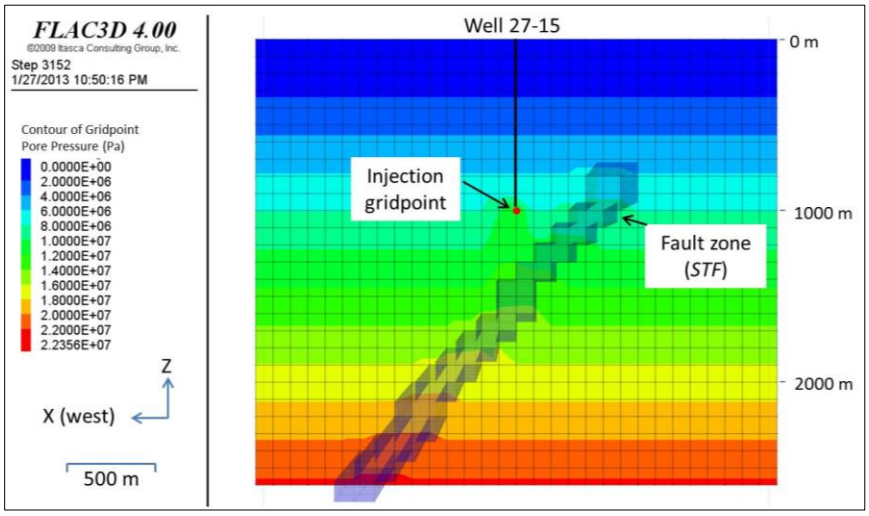

Figure 15 - The Sept 2010 low-flow-rate EGS injection phase is simulated in a FLAC3D hydraulic-only analysis by applying constant injection of fluid (5e-5 m^3/s) at the injection gridpoint (closest point to the casing shoe of the well) during the EGS stimulation. Fluid diffusion through natural fracture networks from the injection point toward greater depths increases the pore pressure within the more permeable STF. Maximum pressure increase (i.e., delta P) simulated within the STF is 1.80 MPa.

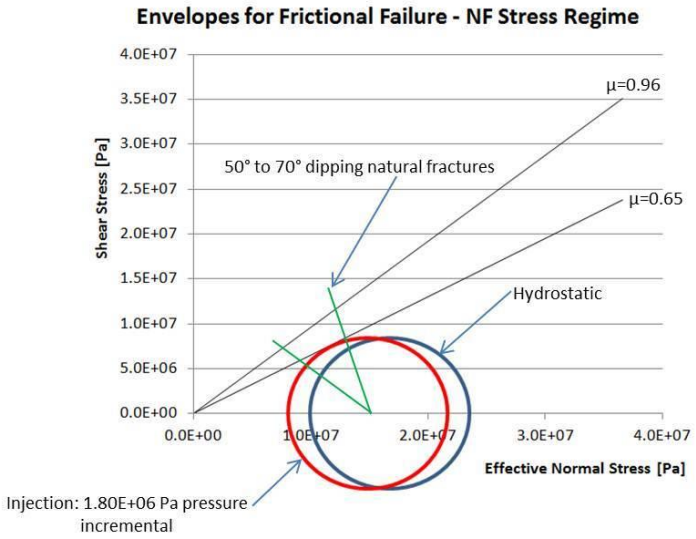

Figure 16 - Normal-stress regime Mohr circles showing shear and effective normal stress at 1600 m depth (location of MEQs and STF) under: 1) hydrostatic conditions defined by groundwater level at 118 m depth (blue circle) and 2) hydraulic pressure generated along the STF after 4 days of fluid injection in 27-15 (red circle), using pressure increase derived from the FLAC3D hydraulic model (Figure 15). Frictional failure lines are based on the coefficient of sliding friction derived from laboratory testing of rock samples from surrounding geologic units [20]. In-situ natural and cohesionless fractures are well-oriented and critically stressed for shear failure under the Sept 2010 low-flow-rate phase hydraulically-induced conditions.

A Mohr-Coulomb analysis suggests that this maximum pressure increase within the STF is sufficient to generate shear failure in well-oriented, cohesionless fractures (Figure 16). The timing required by the DHP to reach a steady value (instantaneous timing pressure response) as well as the maximum pressure, provide key information on the transmissivity of the formation surrounding the open section of the well. The instantaneous downhole pressure response measured in 27-15 during the injection test is simulated through inverse modeling exercises and variation of the formation permeability, until a good approximation is reached. This is a promising sign that the correct calibration of the FLAC3D model has been achieved (Figure 17). The FLAC3D hydro-mechanical coupled analysis predicts shear failure within the STF after

about 4 days of injection into the stimulation zone of well 27-15. This failure is manifest as a contiguous line of active shearing zones in which the stresses satisfy the yield criterion, denoting that frictional failure is occurring over a zone that is elongated in the down-dip direction (Figure 18).

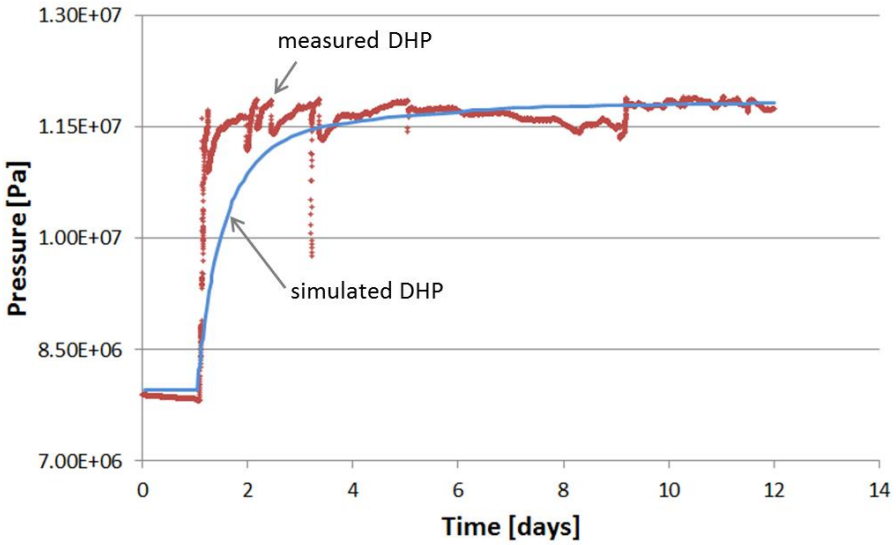

Figure 17 - FLAC3D simulated downhole pressure against downhole pressure response observed in well 27-15 during the Sept 2010 low-flow-rate EGS injection phase.

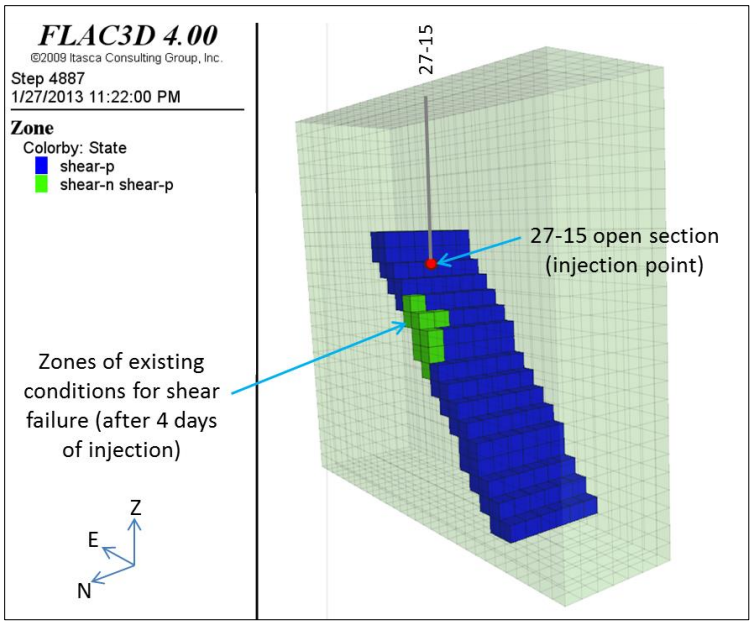

Figure 18 - FLAC3D coupled hydro-mechanical simulation of mechanical response as a result of pressure increase generated along the STF during the Sept 2010 low-flow-rate EGS injection phase. FLAC3D displays zones of the model (i.e. STF) where the pore pressure incremental establishes conditions for the initiation of plastic flow (i.e. shear-n > the zone is at active failure now, -n).

5 DISCUSSION AND CONCLUSIONS

In an attempt to offer a plausible explanation for the location of deep MEQs and to define plausible mechanisms governing the evolution of transmissivity during the EGS experiment, the present study analyzes: 1) 3D site-specific geometry of the key structures involved in the experiment, 2) 3D equivalent permeability tensors in a representative DFN consistent with observations of the fracture network and, specifically, hydraulically conductive fractures within well 27-15, 3) a hydraulic model of fluid pressure distributions within the STF, and 4) a hydro-mechanical simulation consistent with the activation of hydraulically-induced shear failure along the STF.

As introduced above, the MEQ cluster observed throughout the entire EGS experiment is mainly used for structural identification purposes here. The numerical simulation refers to the Sept 2010

injection phase only, when injection operations in 22-22 were reduced and only 1 MEQ was observed. The complexity resulting from combined injection operations at higher-flow-rates is not addressed here and may be discussed in a future study.

The conceptual and numerical modeling results reveal that conditions necessary for fluid "channeling" to depths below the stimulation interval during the Sept 2010 EGS injection phase in well 27-15 can lead to pressurization and poromechanical stressing of the STF. The computed DFN permeability tensors indicate that, within the background natural fracture network, fluid injected at the open section in well 27-15 flows preferentially toward the NNE and the vertical directions (in accordance with the regional structures observed on site).

Two FLAC3D simulations are carried out separately: 1) the hydraulic-only model is run to simulate fluid diffusion and STF pressurization under the Sept 2010 injection phase hydraulically-induced conditions, and the resulting pressure incremental is used as input to the Mohr-Coulomb analytical analysis; 2) the subsequent coupled hydro-mechanical model is run to test the mechanical response of the model and verify conditions for deformation and initiation of shear failure along the STF. The FLAC3D hydraulic-only model is initialized on the basis of the computed DFN permeability tensors and by assigning a higher permeability to the STF. With these conditions, the simulated injected fluid (Sept 2010 phase) migrates from the open section in well 27-15 toward greater depths and it diffuses within the STF. The FLAC3D hydraulic-only model shows localized pressurization of the STF and pore pressure incremental up to 1.8 MPa. Analysis of the resulting effective pressure through analytical Mohr-coulomb circles and FLAC3D hydro-mechanical modeling suggest that these pressures can establish conditions for shear failure within the STF. The injected fluid being colder and denser tends to flows toward the bottom of the STF, generating higher pressure at greater rather than shallower depth within the STF. The subsequent FLAC3D coupled hydro-mechanical numerical model demonstrates that effective stress changes induced by these fluid pressure increases and spatially variable

permeability along the STF are sufficient to produce slip and microseismicity within the STF itself. The activation of shearing after about 4 days of injection is also in good agreement with the time at which the single MEQ event is observed during the low-flow-rate injection phase, suggesting a correlation between slip on the deep STF and the Sept 2010 change in injectivity.

The modeling results (i.e. migration of injected fluid at depth, pressurization and shearing of the STF) appear to validate the hypothesis that the proposed framework (based on the identification of the STF) is a plausible explanation for the presumed correlation between the observed injection rate increase and the occurrence of microseismicity at depths greater than the open section. The parameters under which the models simulate this process for the Sept 2010 phase are listed in Table 2 and 3. Shear failure appears to be more sensitive to variations in the STF friction angle.

The identified STF satisfies some of the conditions that are necessary for shear failure initiation: 1) adequate initial transmissivity, (2) optimum orientation with respect to the local stress state, and (3) enhanced transmissivity with slip [21]. Related physical processes have been inferred in several injection-disposal operations, especially along faults that transit between basement rocks and overlying aquifers. Such a process may have been responsible for recent observations of injection-induced seismicity at Guy, Arkansas [16].

Both numerical (coupled hydro-mechanical) and analytical (mechanical Mohr-Coulomb analysis) results support the existence of regions in the STF which can undergo shear failure under the simulated injection-induced hydraulic pressure conditions. Given the non-uniqueness of the problem, the presented conceptual framework is one possible model for the Desert Peak EGS experiment. Future coupling of thermo-hydro-mechanical-chemical processes will be carried out to better understand the evolution of permeability throughout the Desert Peak EGS stimulation.

ACKNOWLEDGEMENTS

This work is supported by the Great Basin Center for Geothermal Energy under a Geothermal Technology Program (GTP) Faculty Seed Grant, Ormat Technologies, Inc., and Itasca through the Itasca Education Partnership program. The first two authors wish to acknowledge Belinda Poli for providing comments/feedback while reviewing the document.

REFERENCES

[1]. Bonnet, E., O. Bour, N.E. Odling, P. Davy, I. Main, P. Cowie, and B. Berkowitz (2001), Scaling of fracture systems in geologic media, Rev. Geophys., 39(3), 347-383.

[2]. Chabora, E., Zemach, E., Spielman, P., Drakos, P., Hickman, S., Lutz, S., Boyle, K., Falconer, A., Robertson-Tait, A., Davatzes, N.C., Rose, P., Majer, E., Jarpe, S., (2012), Hydraulic stimulation of well 27-15, Desert Peak Geothermal Field, Nevada, USA, *Proceedings, 37th Workshop on Geothermal Reservoir Engineering*, Stanford University, Stanford, California, January 30 - February 1, 2012, SGP-TR-194.

[3]. Davatzes, N.C. and Hickman, S., (2009), Fractures, stress and fluid flow prior to stimulation of well 27-15, Desert Peak, Nevada, EGS project, *Proceedings, 34th Workshop on Geothermal Reservoir Engineering*, Stanford University, Stanford, California, February 9-11, 2009 SGP-TR-187.

[4]. Davatzes, N.C., and Hickman, S.H. (2010), Stress, fracture, and fluid-flow analysis using acoustic and electrical image logs in hot fractured granites of the Coso geothermal field, California, U.S.A., *in M. Poppelreiter*, C. Garcıa-Carballido, and M. Kraaijveld, eds., Dipmeter and borehole image log technology: AAPG Memoir 92, Ch 24., p. 1 – 35.

[5]. de Dreuzy, J.R. & Erhel, J., (2003), Efficient algorithms for the determination of the connected fracture network and the solution to the steady-state flow equation in fracture networks, *Comput. Geosci.*, Vol. 29, No. 1, 107–111.

[6]. de Dreuzy, J.R.; Davy, P. O.and Bour, (2001), Hydraulic properties of two-dimensional random fracture networks following a power-law length distribution: 1. Effective connectivity, *Water Resour. Res*., Vol. 37, No. 8, 2065-2078.

[7]. Drakos, P., Ormat Nevada Inc., (2010), Desert Peak EGS Project, *Geothermal Technologies Program 2010 Peer Review*, DOE: DE-FC6-02ID14406, May 18, 2010.

[8]. Faulds, J.E., and Henry, C.D., (2008), Tectonic influences on the spatial and temporal evolution of the Walker Lane: an incipient transform fault along the evolving Pacific-North American plate boundary, *in Spencer, J.E., and Titley, S.R., eds., Ores and orogenesis: CircumPacific tectonics, geologic evolution, and ore deposits*, Arizona Geological Society Digest 22, p. 437-470.

[9]. Faulds, J.E., Coolbaugh, M.F., Benoit, D., Opplinger, G., Perkins, M., Moeck, I., Drakos, P., (2010), Structural controls of geothermal activity in the Northern Hot Spring Mountains, Western Nevada: the tale of three geothermal systems (Brady's, Desert Peak, and Desert Queen), *Geothermal Resources Council Transactions*, Vol. 34, 2010.

[10]. Faulds, J.E., Garside, L.J., Johnson, G.L., Muehlberg, J., Oppliger, G.L., (2002), Geologic setting and preliminary analysis of the Desert Peak-Brady Geothermal Field, Western Nevada, *Geothermal Resource Council Transactions*, 2002.

[11]. FLAC3D Fast Lagrangian Analysis of Continua in 3 Dimensions, (2009), *User's Guide,* Itasca Consulting Group Inc.

[12]. Goyal, K.P., Benoit, W.R., Maas, J.P., Rosser, J.R., (1983), Desert Peak: a geothermal field in Churchill County, Nevada, *Proceedings Ninth Workshop Geothermal Reservoir Engineering*, Stanford University, Stanford, California, December 1983 SGP-TR-74.

[13]. Hammond, W.C., and Thatcher, W., (2004), Contemporary tectonic deformation of the Basin and Range province, western United States: 10 years of observation with the Global Positioning System, *Journal of Geophysical Research*, v. 109, B08403, doi: 10.1029/2003JB002746.

[14]. Hickman, S. (1991), Stress in the lithosphere and the strength of active faults, *U.S. National Report to the International Union of Geodesy and Geophysics 1987-1990, Reviews of Geophysics*, v. 29, p. 759-775.

[15]. Hickman, S. and Davatzes, N.C., (2010), In-situ stress and fracture characterization for planning of an EGS stimulation in the Desert Peak Geothermal field, Nevada, *Proceedings, 35th Workshop on*

Geothermal Reservoir Engineering, Stanford University, Stanford, California, February 1-3, 2010 SGP-TR-188.

[16]. Horton, S., (2012), Disposal of hydrofracking waste fluid by injection into subsurface aquifers triggers earthquake swarn in central Arkansas with potential for damaging earthquake, *Seismological Research Letters*, Vol. 83, Number 2, March/April 2012.

[17]. Klimczak, C., Schultz R.A., Parashar R., Reeves D.M., (2010), Cubic law with correlated aperture to length and implications for network scale fluid flow, *Hydrogeology Journal*, doi:10.1017/s10040-009-0572-6.

[18]. Larsen, P.H., (1988), Relay structures in a lower Permian basement-involved extensional system, East Greenland, *Journal of Structural Geology*, v.10, p 3-8.

[19]. Lutz, S., Moore, J., Jones, C., Suemnicht, G., and Robertson-Tait, A., (2009), Geological and structural relationships in the Desert Peak Geothermal System, Nevada: Implications for EGS development, *Proceedings 34th Workshop on Geothermal Reservoir Engineering*, Stanford, University, Stanford, CA, SGP-TR-187.

[20]. Lutz, S.J., Hickman, S., Davatzes, N., Zemach, E., Drakos, P., Robertson-Tait, A., (2010), Rock mechanical testing in support of well stimulation activities at the desert Peak geothermal field, Nevada, *Geothermal Resources Council Transactions*, Vol. 34, 2010.

[21]. McClure, M., Horne, R., Is pure shear stimulation always the mechanism of stimulation in EGS?, *Proceedings, Thirty-eight Workshop on Geothermal Reservoir Engineering*, Stanford University, Stanford, California, February 11-13, 2013, SGP-TR-198.

[22]. National Research Council, (1996), Rock Fractures and Fluid Flow: Contemporary Understanding and Applications, *National Academy of Sciences*, New York, 551 p.

[23]. Nicol, A., Watterson, J., Walsh, J., Childs, C., (1996), The shapes, major axis orientations and displacement patterns of fault surfaces, *Journal of Structural Geology*, Vol. 18, No. 2/3, pp. 235 to 248, 1996.

[24]. Parashar, R. and Reeves D.M. (2012), On iterative techniques for solving flow in large two-dimensional discrete fracture networks, *Journal of Computational and Applied Mathematics*, doi:10.1016/j.cam.2012.02.038.

[25]. Priest, S.D., (1993), *Discontinuity Analysis of Rock Engineering*, Chapman and Hall, London.

[26]. Reeves, D.M., Benson, D.A., Meerschaert, M.M., (2008a), Transport of conservative solutes in simulated fracture networks: 1. Synthetic data generation, *Water Resour. Res.*, Vol. 44, No. W05401, doi:10.1029/2007WR006069.

[27]. Reeves, D.M., Benson, D.A., Meerschaert, M.M., Scheffler, H.-P, (2008b), Transport of conservative solutions in simulated fracture networks: 2. Ensemble solute transport and the correspondence to operator-stable limit distributions, *Water Resour. Res.*, Vol. 44, No. W05410, doi:10.1029/2008WR006858.

[28]. Reeves, D.M., Parashar, R., Zhang, Y., (2012), Hydrogeologic characterization of fractured rock masses intended for disposal of radioactive waste, *Radioactive Waste*, Dr. Rehab Abdel Rahman (Ed.), ISBN: 978-953-51-0551-0, InTech.

[29]. Reeves, D.M., Pohll, G., Lyles, B., Faulds, J., Louie, J., Ehni, B., Kratt, C., Cooper, C., Parashar, R., Pullammanappallil, S., Noel D., (2012), Geothermal resource characterization and evaluation at Astor Pass, Nevada, *Geothermal Resources Council Transactions*, 36, 1371-1376.

[30]. Renshaw, C.E. (1999). Connectivity of joint networks with power law length distributions, Water Resour. Res., 35(9), 2661-2670.

[31]. Robertson-Tait, A., Lutz, S.J., Sheridan, J., and Morris, C.L. (2004), Selection of an interval for massive hydraulic stimulation in well DP 23-1, Desert Peak East EGS project, Nevada, *Proceedings, 29th Workshop on Geothermal Reservoir Engineering*, Stanford University, Stanford CA, SGP-TR-175.

[32]. Rose, P., Leecaster, K., Drakos, P., Robertson-Tait, A., Tracer testing at the Desert Peak EGS Project, *Geothermal Resource Council Transactions*, Vol. 33, 2009.

[33]. Schultz, R.A., Soliva, R., Fossen, H., Okubo, C.H., Reeves, D.M., (2008), Dependence of displacement-length scaling relations for fractures and deformation bands on the volumetric changes across them, *Journal of Structural Geology* 30 (2008) 1405-1411.

[34]. Sherburn, S. and Quinn, R., (2012), An Assessment of the Effects of Hydraulic Fracturing on Seismicity in the Taranaki Region, *GNS Science Consultancy Report 2012/50*, February 2012.

[35]. Shipton, Z.K., Soden, A.M., Kirkpatrick, J.D., Bright, A.M., Lunn, R.J., (2006), How thick is a fault? Fault-Displacement-Thickness scaling revisited, in Abercrombie, R., (Eds) Earthquakes: Radiated energy and the physics of faulting, pp. 193-198, *AGU bulletin*, 2006.

[36]. Stacey, R.W., Robertson-Tait, A., Drakos, P., Zemach, E., (2010), EGS stimulation of well 27-15, Desert Peak geothermal field, Nevada, *Geothermal Resource Council Transactions*, Vol. 34, 2010.

[37]. Swyer, M.W., Davatzes, N.C., (2012), Using boundary element modeling of fault slip to predict patterns of stress perturbation and related fractures in geothermal reservoirs and explore parameter uncertainty, *Proceedings, Thirty-Seventh Workshop on Geothermal Reservoir Engineering*, Stanford University, Stanford, California, January 30 – February 1, 2012, SGP-TR-194.

[38]. Taron, J., Elsworth, D., Min, K.B., (2009), Numerical simulation of thermal-hydrologic-mechanical-chemical processes in deformable, fractured porous media, *International Journal Rock Mechanics & Mining Sciences 2009*, doi: 10.1016/j.ijrmms.2009.01.008.

[39]. Townend, J., and Zoback, M. D. (2000), How faulting keeps the crust strong, *Geology*, v. 28, p. 399–402.

[40]. Zemach, E., Drakos, P., Robertson-Tait, A., Lutz, S.J., (2010), Feasibility evaluation of an “in-field” EGS project at Desert Peak, Nevada, USA, *Proceedings World Geothermal Congress*, Bali, Indonesia, 25-29 April 2010.

4. MANUSCRIPT II - DESERT PEAK EGS PROJECT CONCEPTUAL MODEL AND NUMERICAL ANALYSIS: RESERVOIR RESPONSE TO THE SHALLOW MEDIUM FLOW-RATE HYDRAULIC STIMULATION PHASE

Stefano Benato[1,#], Stephen Hickman [2], Nicholas C. Davatzes [3], Joshua Taron[2], Paul Spielman[4], Derek Elsworth[5], Ernest L. Majer[6], Katie Boyle[6]

1 - Division of Hydrologic Sciences, Desert Research Institute, Reno, NV, 89512 USA

2 - U.S. Geological Survey, Menlo Park, CA, 94025 USA

3 - Temple University, Philadelphia, PA, 19122 USA

4 - Ormat Nevada Inc., Reno, NV, 89511 USA

5 - Pennsylvania State University, University Park, PA, 16802 USA

6 - Lawrence Berkeley National Laboratory, Berkeley, CA 94720 USA

Corresponding author: E-mail address: stefano.benato@gmail.com

ABSTRACT

A series of stimulation treatments performed as part of the Engineered Geothermal System (EGS) experiment in the shallow open-hole section of Desert Peak well 27-15 (September 2010 - November 2012) produced injectivity gains at variable wellhead pressures below and above the magnitude of the least horizontal principal stress (S_{hmin}), which is consistent with hydraulically-induced mechanical shear and tensile failure in the surrounding rock. A conceptual framework for the overall Desert Peak EGS experiment is developed and tested based on a synthesis of

previously acquired structural and geological data, down-hole fracture attributes, in-situ stress conditions, pressure interference tests, geochemical tracer studies, and observed induced seismicity. Induced seismicity plays a key role in identifying the geometry of large-scale geological structures that could potentially serve as preferential flow paths during some of the stimulation phases. The numerical code FLAC3D is implemented to simulate the reservoir response to hydraulic stimulation and to investigate in-situ conditions conducive to both tensile and shear failure. Results from the numerical analysis show that conditions for shear failure could have occurred along fractures associated with a large northeast-trending normal fault structure which coincides with the locations of most of the observed micro-seismicity. This structure may also provide a hydrologic connection between EGS well 27-15 and injection/production wells further to the south-southwest.

1 INTRODUCTION & BACKGROUND

The goal of an Engineered Geothermal System (EGS) is to develop a complex and extensive fracture network in hot, low permeability rocks lacking commercial-scale permeability. In these systems, a desired characteristic of the generated network is a large ratio of surface area to rock volume for optimal heat exchange. When applied to operational hydrothermal reservoirs, EGS stimulations are intended to convert low-permeability unusable wells into operational injectors or producers, thereby increasing field productivity. EGS experiments to date, such as the French-German Soultz-sous-Forêts [16][17], the US Desert Peak [4][43][51] and Newberry [5], and the Australian Habanero [50], have typically used hydraulic stimulation techniques to enhance the permeability and connectivity of preexisting and naturally tortuous fracture networks generally found to be ubiquitous within the crust.

The Desert Peak geothermal field is a successfully operating geothermal field with ~10 MWe output located in the northern portion of the Hot Springs Mountains of northwestern Churchill

County, Nevada, about 100 km northeast of Reno. Well 27-15 was selected to carry out a U.S. Department of Energy-supported EGS project with the intent of improving the hydraulic connection with the rest of the reservoir and enhancing overall injectivity (see [4] and references therein). Well 27-15 was originally drilled to a total depth of about 1771 m, with the completed open interval (914 m-1771 m) displaying a baseline injectivity of ~0.2 gpm/psi [51][43]. In 2010 it was plugged back to a total depth of about 1067 m, with the completed open-hole section available for stimulation extending from 914 m to 1067 m (here referred to as the "shallow" stimulation interval) and displaying a baseline injectivity of ~0.012 gpm/psi [4][43]. In November 2012, following the shallow stimulation treatment, the well was re-completed to the original depth (1771 m), resulting in a longer open-hole section extending from 914 m to 1771 m (here referred to as the "extended" stimulation interval) which was then subjected to a final phase of full-hole stimulation [22]. Only hydraulic stimulation treatments carried out in the shallow interval of well 27-15 are considered in this study.

The first series of hydraulic stimulations conducted in the shallow open interval of Desert Peak well 27-15 from September 2010 through April 2011 led to a nearly 60-fold increase in injectivity with respect to the shallow interval baseline value [4]. This stimulation was carried out using two different fluid pressure conditions relative to the least principal stress. An initial period of shear stimulation (September 2010), which increased injectivity from ~0.011 to ~0.15 gpm/psi (more than one order of magnitude), was conducted as a series of steps with fluid pressures less than, or equal to, a maximum of 4.5 MPa wellhead pressure (WHP). The maximum WHP was intentionally chosen to remain below the magnitude of the least horizontal principal stress (WHP ~5.2 MPa), which was measured in this well just below the casing shoe with a mini-hydraulic fracturing test [21]. This low flow-rate phase was immediately followed by a large-volume, controlled hydraulic fracturing operation (April 2011) that lasted more than 23 days and involved high injection rates and WHP in excess of the least principal stress. This hydraulic fracturing

stage resulted in a final ~0.54 gpm/psi injectivity (additional 4-fold increase) [4]. Temperature-Pressure-Spinner (TPS) logs show that the injected fluid exited and stimulated well 27-15 at two primary locations: (1) the bottom of the open-hole section during the low flow-rate injection phase and (2) the hydraulic fracture just below the casing shoe during the high flow-rate injection phase. Further stimulation phases – not considered here – were performed in the shallow open interval in May-June 2011 and October 2011, and in the extended open interval in January-March 2013 [22]. Stimulation operations along the extended open interval provided a final > 2.1 gpm/psi injectivity [22][3], though the analysis of this treatment is still in progress.

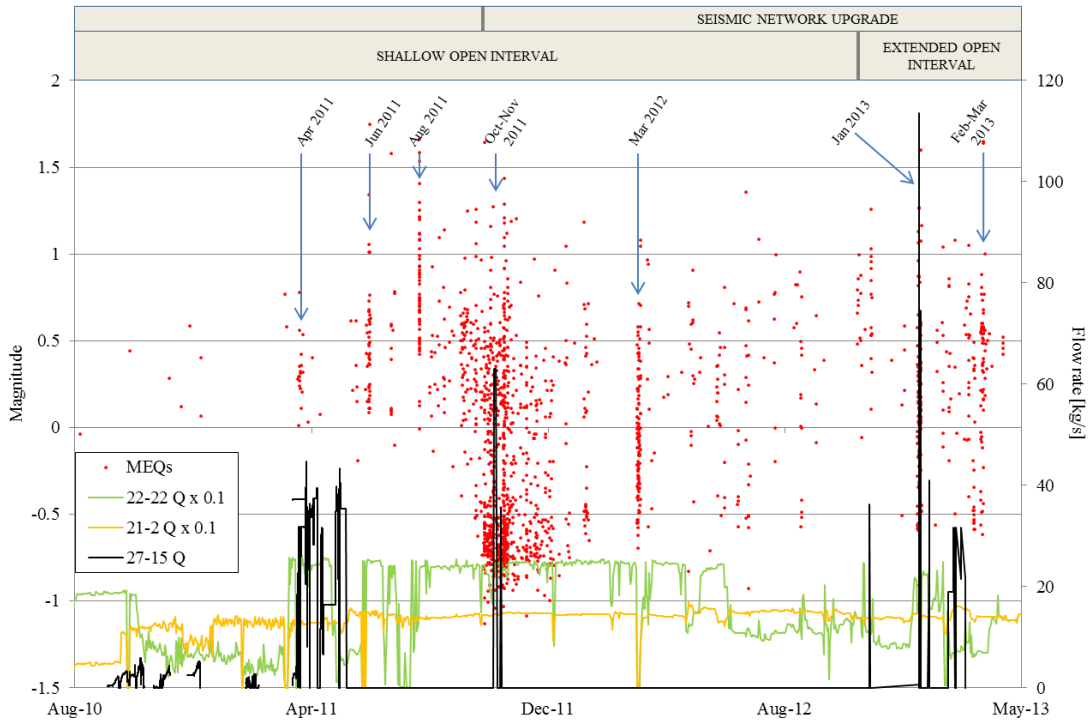

Figure 1 - Injection flow-rate history in wells 27-15, 22-22 and 21-2, and observed microseismicity throughout the EGS project. Flow-rates in wells 22-22 and 21-2 are reduced (10 times) for graphic purposes only. Different time windows in the upper part of the graph point at periods of higher density of microseismic activity. This activity appears to be associated with sudden changes in injection flow-rates in either or both wells 22-22 and 27-15.

Throughout the EGS experiment (2010-2013), a great number of micro-earthquakes (MEQs) with magnitudes ranging from -1.0 to +1.5 were recorded between EGS well 27-15 and injection/production wells to the south-southwest, including in proximity of injection wells 21-2 and 22-22. Some of these events appear to display a cause-effect relation between hydraulic stimulations performed in well 27-15 and deformation in the reservoir, although this relation was often complicated by injection operations being carried out simultaneously in injectors 21-2 and 22-22 (Figure 1).

A cause-effect relation between fluid injected in well 22-22 and the occurrence of microseismicity seems evident on a few occasions such as August 2011 (Figure 2) and March 2012 (Figure 3). Stimulation operations were then down in EGS well 27-15 and seismic swarms followed sudden injection changes in well 22-22, and clustered in the vicinity of well 22-22. In other instances such as in April 2011, microseismic events appear to have developed as a result of stimulation treatments in well 27-15 and their hypocenters clustered in volumes closer to well 27-15 (the majority in the same depth range as a deep fault zone discussed in paragraph 3) (Figure 4). For these reasons, the April 2011 stimulation phase is used for analysis and modeling purposes here (see below). Whether or not a cause-effect relation exists between fluid injected in well 21-2 and the occurrence of microseismicity is investigated and discussed below (see Par. 5).

During most of the stimulation stages, including April 2011, the MEQs appear to have occurred when the greatest injectivity gains – indicating permeability development/enhancement – were observed, and for this reason it is critical to correctly understand the implications the events may have had in the stimulation treatment (Figure 5).

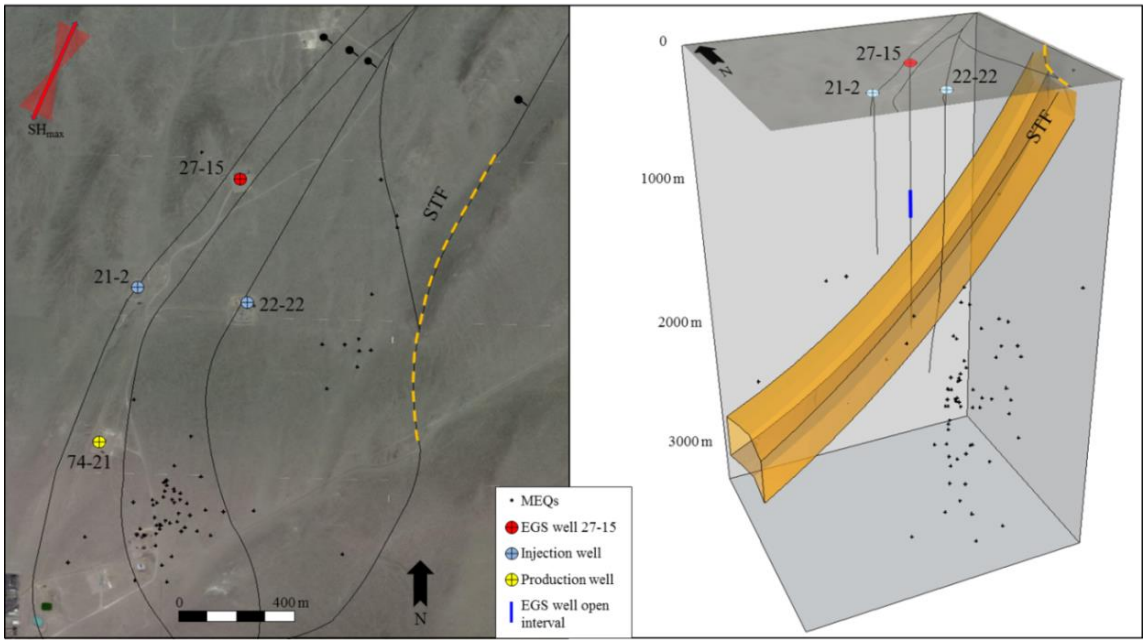

Figure 2 - Map & 3D view of the induced microseismicity observed in August 2011. Over this period, injection operations in EGS well 27-15 are down while injection in well 22-22 is being altered. The events appear located primarily around and south of well 22-22 and at the depth of a deep structural feature (STF discussed in paragraph 3). SHmax direction inferred from observation of borehole failures in well 27-15 [8][21]. Black lines show surface trace of interpreted faults [15]; larger black dots shown on downthrown sides of normal faults.

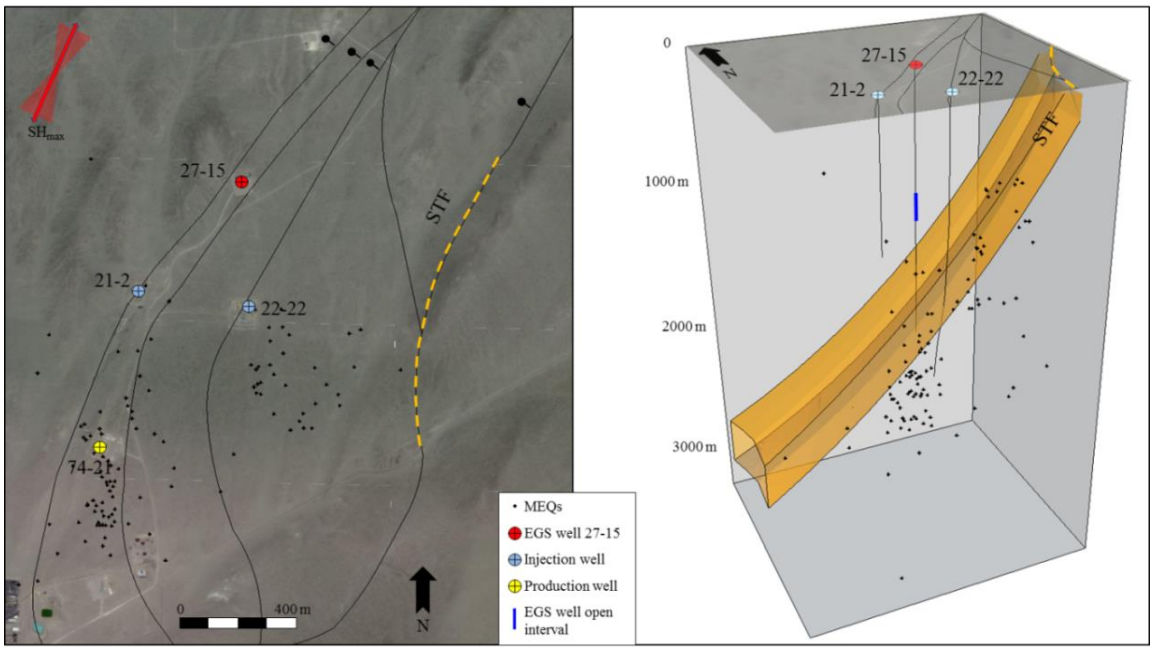

Figure 3 - map & 3D view of the induced microseismicity observed in March 2012. Over this period, injection operations in EGS well 27-15 are down while injection in well 22-22 is being altered. The events appear located primarily around and south of well 22-22 and at the depth of a deep structural feature (STF discussed in paragraph 3). SHmax direction inferred from observation of borehole failures in well 27-15 [8][21]. Black lines show surface trace of interpreted faults [15]; larger black dots shown on downthrown sides of normal faults.

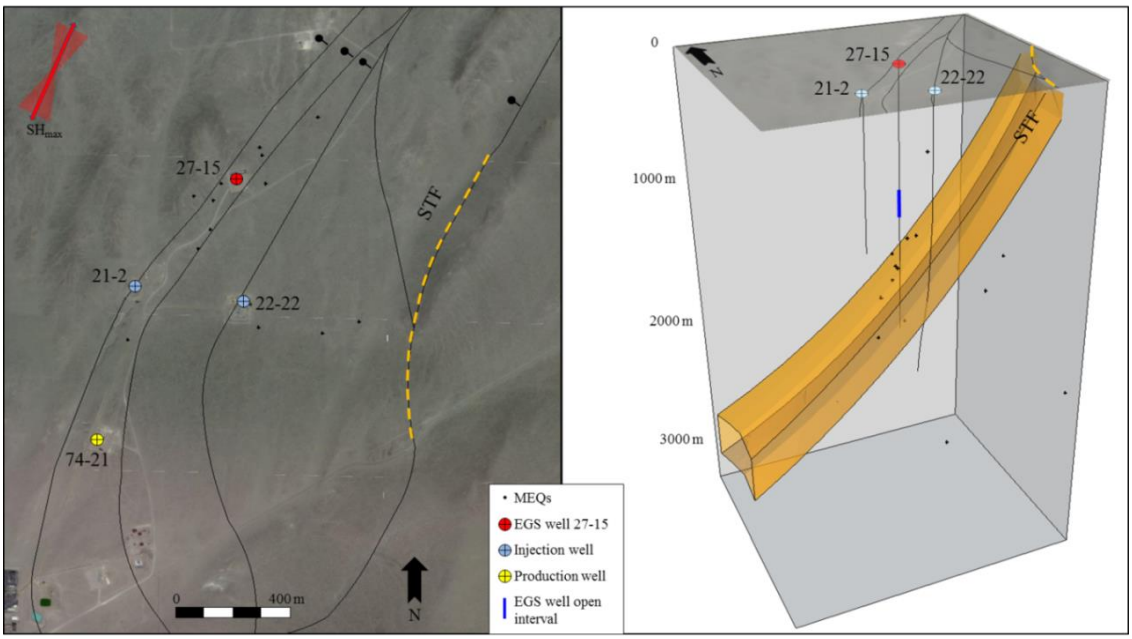

Figure 4 - map & 3D view of the induced microseismicity observed between April 2-6, 2011 (medium flow-rate phase). Over this period, the shallow open interval of EGS well 27-15 is being stimulated while injection in well 22-22 is relatively stable. The events appear primarily located around well 27-15 and at the depth of a deep structural feature (STF discussed in paragraph 3). SHmax direction inferred from observation of borehole failures in well 27-15 [8][21]. Black lines show surface trace of interpreted faults [15]; larger black dots shown on downthrown sides of normal faults.

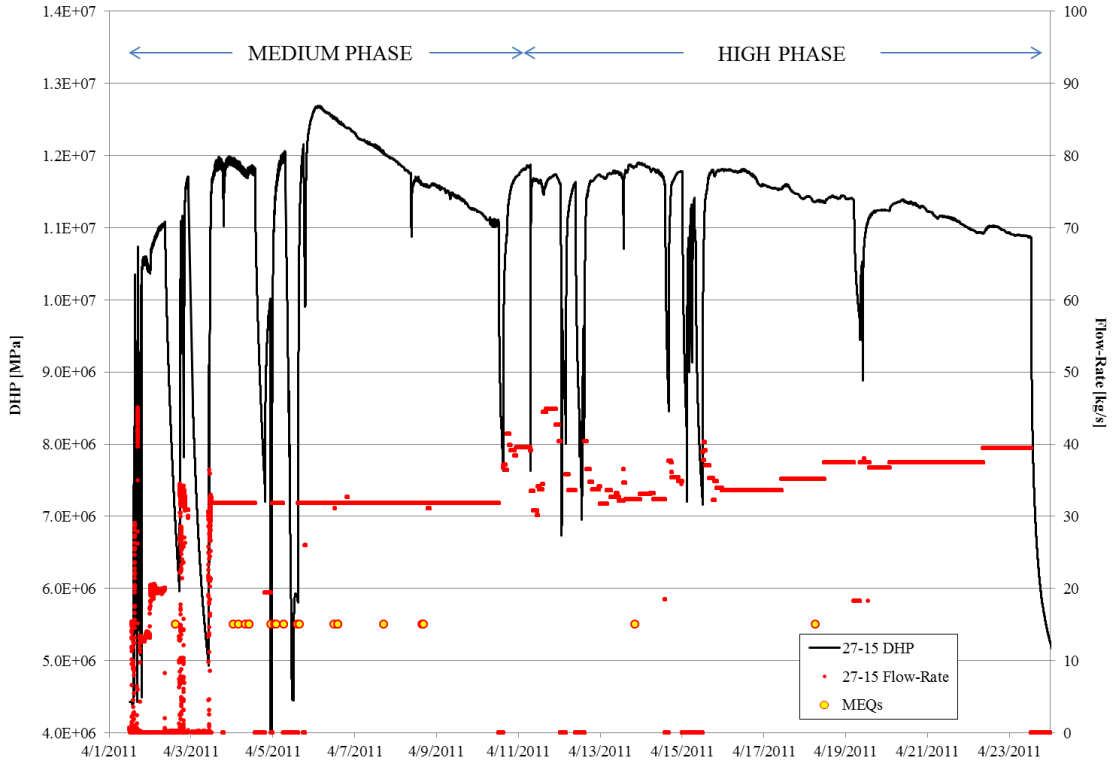

Figure 5 - Well 27-15 injection flow-rate and wellhead pressure (WHP) during the April 2011 medium to high flow-rate stimulation phases. Pressure declines under constant or increasing injection flow-rates indicate reservoir transmissivity enhancements. Microseismic activity precedes - or coincides with - the greatest injectivity gains.

Prior to the seismic network upgrade (November 2012), poor focal sphere coverage and limited constraints (signal-to-noise ratio) on the seismic velocity model made it difficult to: (1) derive the exact source mechanism for these MEQs, (2) detect events smaller than magnitude $M_w < +0.1$, and (3) define the location of individual events with precision. Regarding the detection of tensile failure during stimulation above S_{hmin}, relatively high frequency signals at the crack tip are usually produced – typically of $M << 0$ – which can only be detected with the use of specialized down-hole instruments [41]. Thus, it is likely that the primary process generating the observed MEQ events at Desert Peak was hydraulically-induced shear failure (Mode II-III) along pre-existing natural fractures and faults that were well-oriented within the regional stress field for

shear failure [8] [21]. Given that most of the MEQs occurred simultaneously with the greatest recorded injectivity gains, this may also indicate that some shear failure (i.e., hydro-shearing resulting in the generation of MEQs) could have contributed to reservoir transmissivity enhancement at Desert Peak (i.e., fluid supplied from well 27-15 → shear deformation → MEQs → reduction in resistance to flow → permeability gain), although this will be verified as part of a future study.

2 OBJECTIVES & ROADMAP

In this paper a conceptual model is developed from a comprehensive synthesis of all available geological, structural, hydrologic and seismic datasets. A hydro-mechanical, numerical framework is then implemented to test if the proposed conceptual model is generally able to reproduce observations from selected phases of the shallow stimulation experiment. The parameterization of the model is based on rock mechanics tests [30], formation permeability computed from the integration of analyses discussed in par. 4, and stress magnitudes from a mini-hydraulic fracturing experiment.

The first goal of this study is to identify any structure that (1) appears to be spatially associated with the development of microseismicity during the various stimulation operations, and (2) may also represent a permeability conduit enabling connection to the rest of the field.

The second goal of the study is to numerically simulate whether fluid pressure diffusion in the reservoir in response to selected injection phases into well 27-15 is sufficient to induce frictional failure within the identified structures. This simulation utilizes: (a) an assessment of permeability distribution based on the integration of injectivity tests, pressure response modeling, interference test modeling and statistical Discrete Fracture Network (DFN) analyses, (b) injection rates applied to well 27-15 during the April 2011 shallow, medium flow-rate stimulation phase (Figure 5), and (c) concurrent injection rates applied to nearby wells 22-22 and 21-2.

The April 2011 shallow, medium flow-rate phase is selected as a good candidate for numerical simulation because: (a) the time of the microseismic swarm observation appears to have coincided with the beginning of the hydraulic treatment in well 27-15 (Figure 1), (b) the MEQs clustered in volumes closer to well 27-15 (Figure 4), (c) the occurrence of MEQs preceded and coincided with injectivity gains observed in well 27-15 (Figure 5), and (d) the injection flow-rate applied to well 27-15 was relatively constant. For the purpose of this study and for simplicity, only the medium flow-rate is simulated here, as the overall down-hole conditions were similar to the subsequent high flow-rate stimulation phase.

3 RESERVOIR CONCEPTUAL MODEL

The Desert Peak geothermal field is located in the northern portion of the Hot Springs Mountains. Extensive drilling in the Desert Peak geothermal area has shown that the Hot Springs Mountains are mainly comprised of Tertiary volcanic and sedimentary rocks that lie directly on Mesozoic metamorphic and granitic basement [12][15][29].

A combination of ~2-3 km of volcanic and sedimentary rocks makes up the Tertiary section. These are often intruded by late Miocene basalt plugs, as in the case of Desert Peak, where a large basalt plug is capped by porphyritic basalt flow (8.9 Ma). The late Miocene section of the northern Hot Springs Mountains incorporates several ash-fall deposits (i.e., Tephras). These are key markers which ease and constrain the correlation of stratigraphic units and make the offset evaluation between fault blocks possible (i.e., offset magnitude on major faults) [44][12].

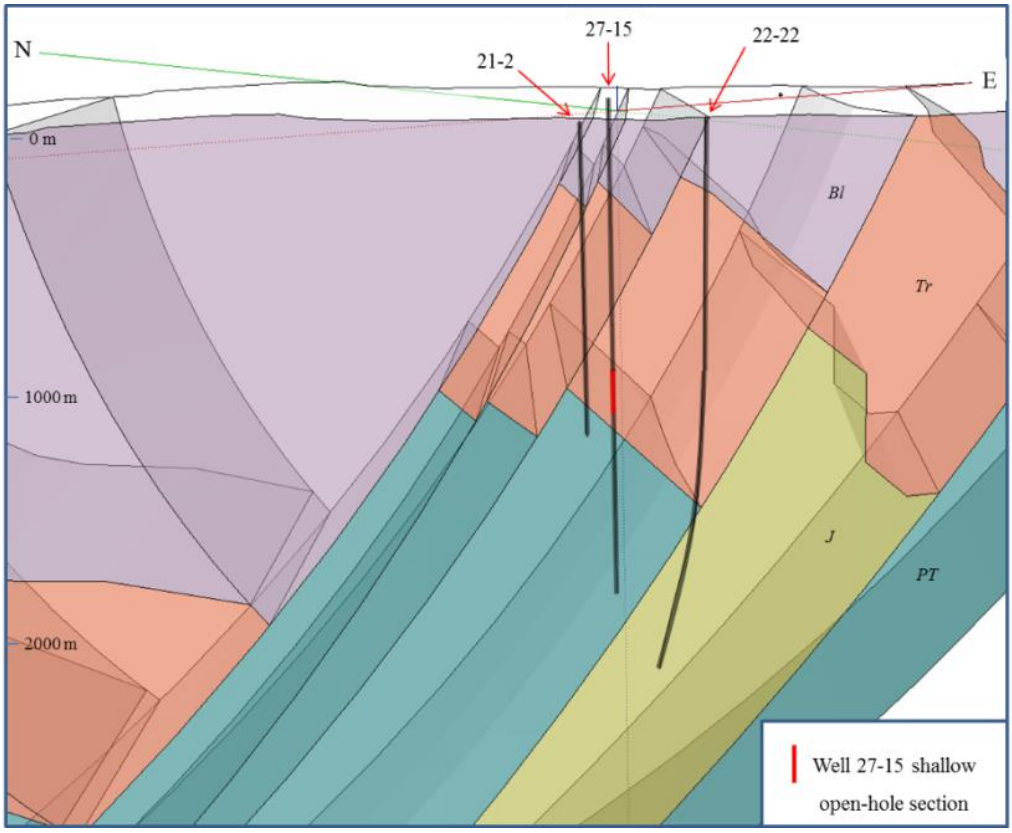

Figure 6 - Three-dimensional geological model of the EGS wellsite, derived from [15][12], but with a simplified lithology, grouped into fewer units (Figure 7) to facilitate conceptual modeling and numerical simulation. Unit abbreviations: J, Jurassic metamorphic basement; PT, Pre-Tertiary basement; Tr, Tertiary lavas and ash-flow tuffs; Bl, basalt lavas.

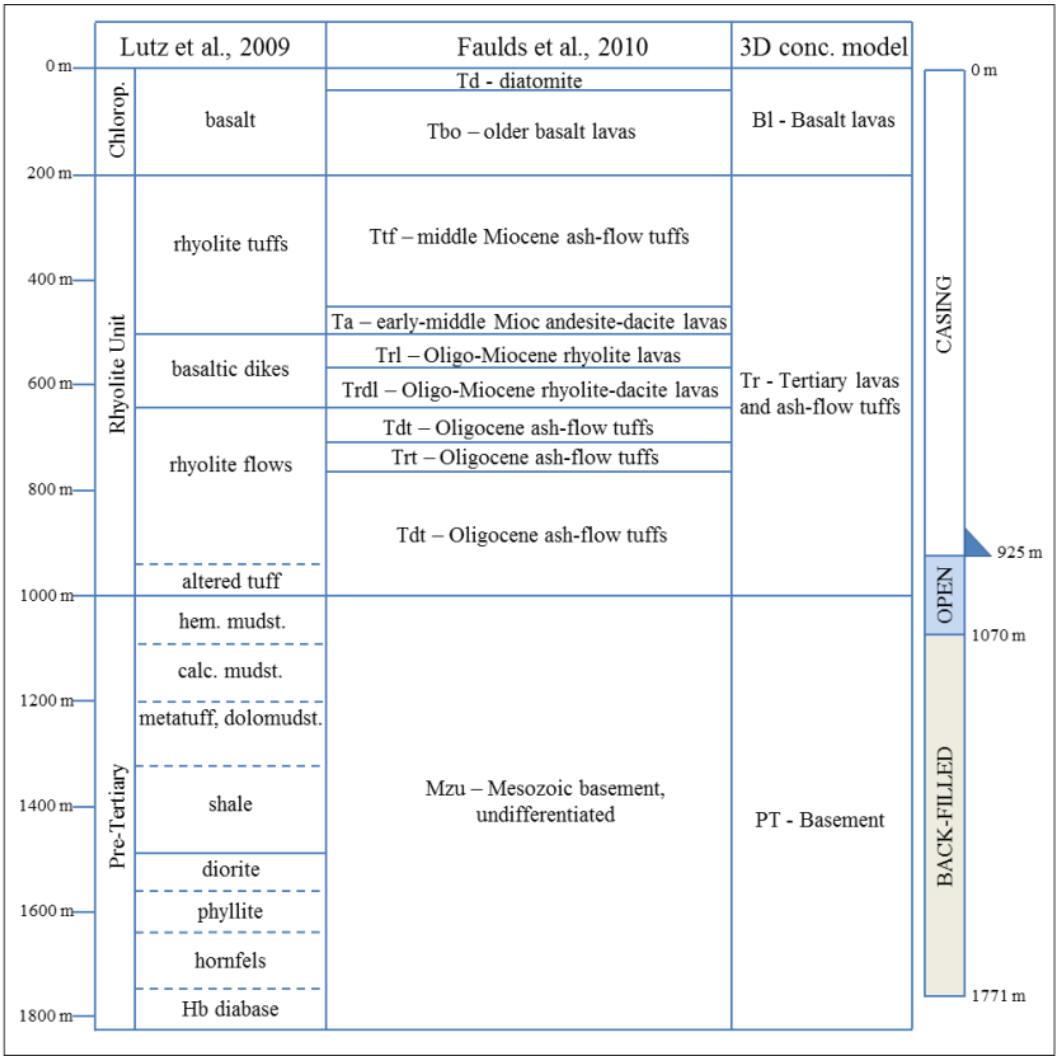

Figure 7 - Lithology correlations between available Desert Peak geological models [12] [15] [29] [30] and simplified lithological grouping used for the wellsite's 3D conceptual model (Figure 6). Well 27-15 schematic diagram (shallow interval completion) also shown.

The Desert Peak geothermal field and the Northern Hot Springs Mountains lie within the NNE-trending Humboldt structural zone, which is orthogonal to the extensional direction of the Walker Lane. On a large scale, the Walker Lane is a system of dextral faults that accommodates ~20% of the relative motion between the Pacific and North American plates [11].

Geodetic data indicate that about 1 cm/year of dextral motion is transferred from the north end of the Walker Lane into the WNW extension between the Sierra Nevada block and central parts of the Great Basin. This active extension and associated dilation is probably responsible for the recurrent geothermal systems in this region [13].

The dominant fault pattern trends about N25°E and appears to be related to Basin-and-Range tectonic stresses. The Humboldt structural zone may reflect both strain transfer and extension related to the Walker Lane. The most significant fault in the area is the WNW-dipping Rhyolite Ridge fault zone, which consists of several strands and steps to the left, in the vicinity of the Desert Peak geothermal field [12] (Figure 8). NW-trending gravity contours across the Desert Peak field may reflect a relay ramp [28] associated with southward-increasing displacement on the Rhyolite Ridge fault zone [12]. The role of the relay ramp in concentrating stress within the geothermal system based on fault geometry and local stress state is addressed in [45][46]. Kinematic data gleaned from fault surfaces indicate dip-slip normal displacement on the NNE striking faults and a WNW-trending extension direction, which is compatible with: (1) regional extension directions inferred from geodetic data [18], (2) borehole tensile failure data and stress magnitudes from a mini-hydraulic fracturing experiment, and (3) rock densities consistent with a normal faulting stress regime from wells in the area [8][21] (Figure 8). The current stratigraphy and structural conceptualization at Desert Peak is based on original core logs and on the interpretation mainly of concealed faults. The location of structures and units may be approximate. A more detailed geological and structural analysis together with a thorough re-logging of cuttings and core (as was done in the case of the neighboring Brady's field [14]) may provide further constraints on the Desert Peak reservoir conceptualization in future.

The most productive area in the system occupies left steps in the NNE-striking, W-dipping normal fault system [12]. Although left-stepping oblique or strike-slip faults are not required for the localization of high permeability (i.e., interaction among normal faults could also lead to

dilation and locally enhanced fracture permeability in this region), the potential for high fracture density in this step-over region could enhance permeability [12] and is consistent with modeled slips on the Rhyolite Ridge fault [46]. Tracer test returns in production well 74-21 from injection in both 21-2 and 22-22 confirm strong hydraulic connectivity in the productive area of the field [36] (Figure 9). In contrast, tracer tests conducted by injecting into well 27-15 and sampling in well 74-21 show only a modest connection between 27-15 and the rest of the reservoir [4].

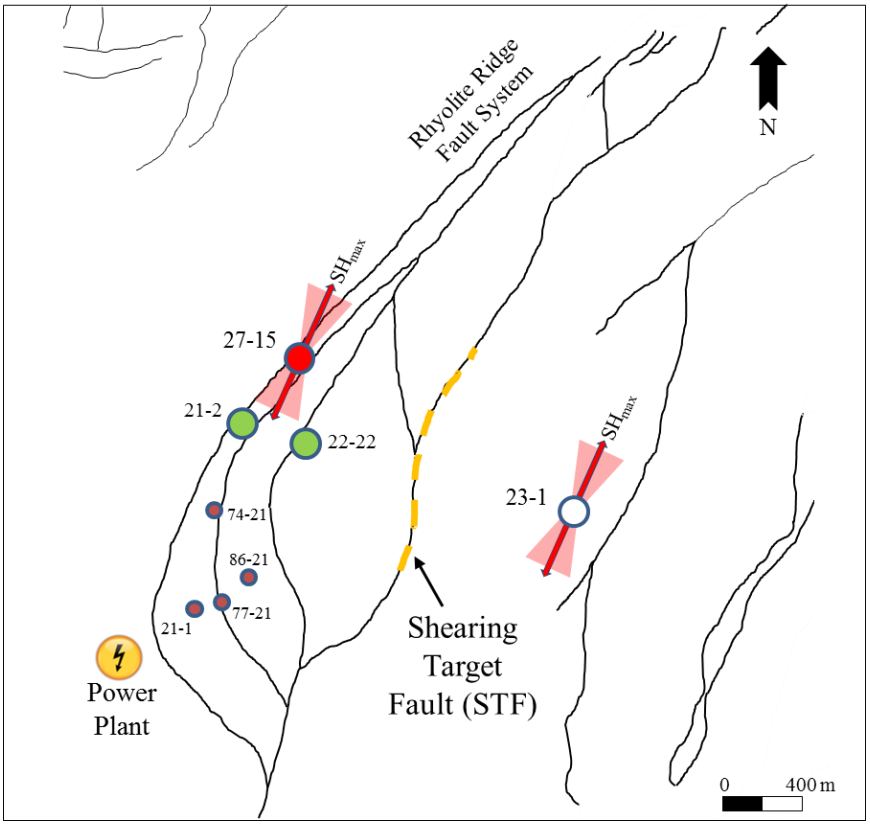

Figure 8 - Desert Peak Geothermal Field: a consistent orientation of S_{hmin} is inferred from observations of tensile fractures in wells 27-15 [8] and 23-1 [35]. Production wells are shown in dark red, injectors in green, EGS well 27-15 in light red, unused well 23-1 in white (Figure modified from [46] and [15]). The surface trace of the Shearing Target Fault (STF) inferred to intersect wells 22-22 and 27-15 at depth is shown with an orange dashed line.

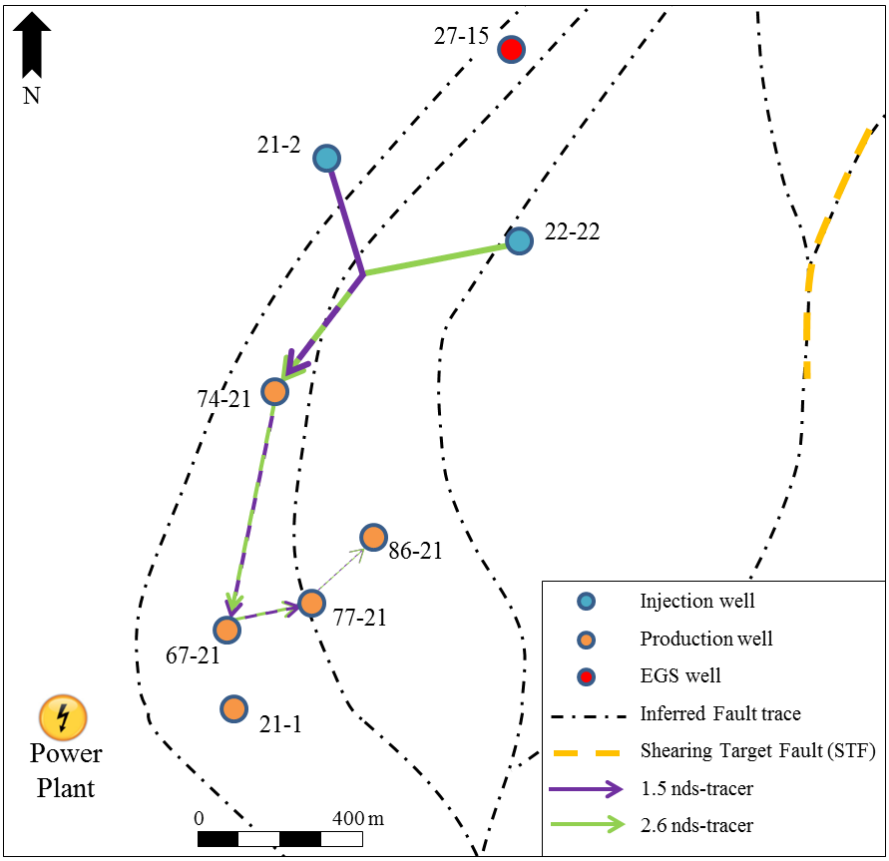

Figure 9 - Hydrologic connections (i.e., flow paths) inferred in 2009 by injecting tracers in injection wells 22-22 and 21-2 and by sampling in production wells. Results show strong returns nearest producer 74-21, and slower, weaker returns to other wells. A connection between reservoir and 22-22 occurs through the Rhyolite Unit base (Figure modified from [36][15]).

Like many other fields, the volume of hot rock surrounding the Desert Peak geothermal field is far more extensive than the volume of hot *and* permeable rock. These circumstances drove the need for an EGS experiment that could extend the reservoir into untapped hot rock to the north of the field, creating potential new injectors and increasing the residence time of the fluid.

The orientations of the horizontal principal stresses in well 27-15 were determined through the analysis of drilling-induced tensile fractures visible in both high-temperature acoustic televiewer

(ABI85) and formation micro-scanner (FMS) logs. These drilling-induced structures indicate that the azimuth of the minimum horizontal principal stress, S_{hmin}, is currently oriented 114 ± 17° (corresponding to a maximum horizontal principal stress of 024 ± 17°) [8]. Previous analysis of stress directions from borehole failure observed in well 23-1, located 2 km E-SE of well 27-15, is in excellent agreement with stress orientations inferred from well 27-15 [35], suggesting a regionally uniform stress field (Figure 8).

A detailed 3D analysis of the EGS wellsite, based on the Desert Peak geological cross section and map [12][15], suggests that EGS well 27-15 and injector well 22-22 encounter the same permeable horizon at about 1400 m depth, which is consistent with a moderate inter-well connection revealed by pressure interference testing (Figure 10) [51] and TPS logs [8]. Significant fluid loss associated with large-aperture fractures is observed at approximately 1400 m in well 27-15 [8] (prior to plugging back the borehole), and in well 22-22 a major feed zone is found at ~1340 m depth. The weak connectivity between wells 27-15 and 22-22 confirmed by the interference hydraulic testing (Figure 10) [51] may be occurring through this deeper fluid loss/feed zone (~1400 m). This horizon – striking approximately parallel to S_{Hmax} – appears to be the projection at depth of one of the main Rhyolite Ridge Fault Zone structures mapped at the surface (Figure 11, Figure 8), and coincides with the depth (1400 to 1600 m) at which several MEQs are observed during both shallow and extended stimulation operations in well 27-15 (Figure 4 and Figure 19).

Therefore, a major NNE-SSW striking and WNW dipping segment of the Rhyolite Ridge Fault Zone might extend between wells 22-22 and 27-15 and establish a cross-formational hydraulic connection between these two wells (Figure 11). This structure appears to represent a preferential flow path for fluids circulating in its vicinity and it is well oriented for shear failure within the current stress field [21] [46]. For these reasons it will be referred to as "STF" *(Shearing Target Fault)* throughout this paper. Tracer tests suggest that permeability along this structure decreases

northward of the injectors (Figure 9) or with increasing distance from the most productive area in the field [36]. In the vicinity of well 27-15, the STF is sub-parallel to the main Rhyolite Ridge Fault Zone, while it appears to slightly change its orientation and steps over south toward wells 22-22 and 21-2 (Figure 8). Among the many Rhyolite Ridge Fault strands, the STF shows one of the greatest throws, of the order of several tens of meters. Studies of surface outcrops and borehole logs of normal faults in similar settings suggest the damage zone associated to such throws may be of the order of tens of meters and even thicker where variations in dip and linkage occur [42].

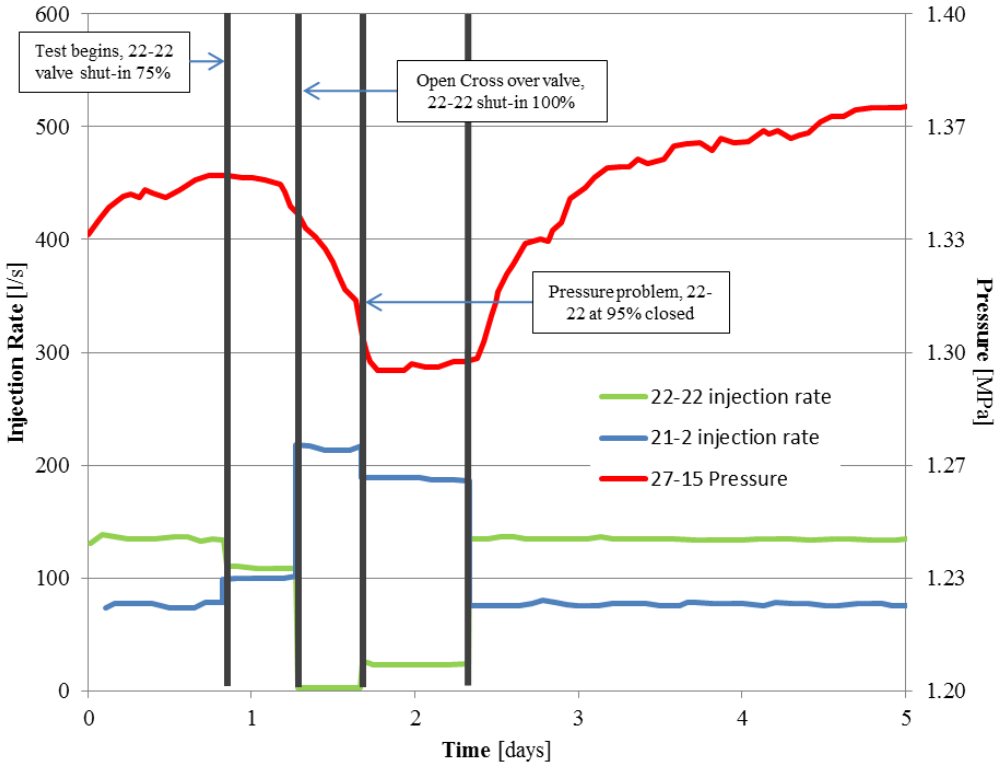

Figure 10 - 2009 interference test conducted by altering injection rates in wells 22-22 and 21-2 while observing pressure response in well 27-15 [51]. The test shows that well 27-15 is mainly (though weakly) connected with well 22-22 (Figure modified from [51]).

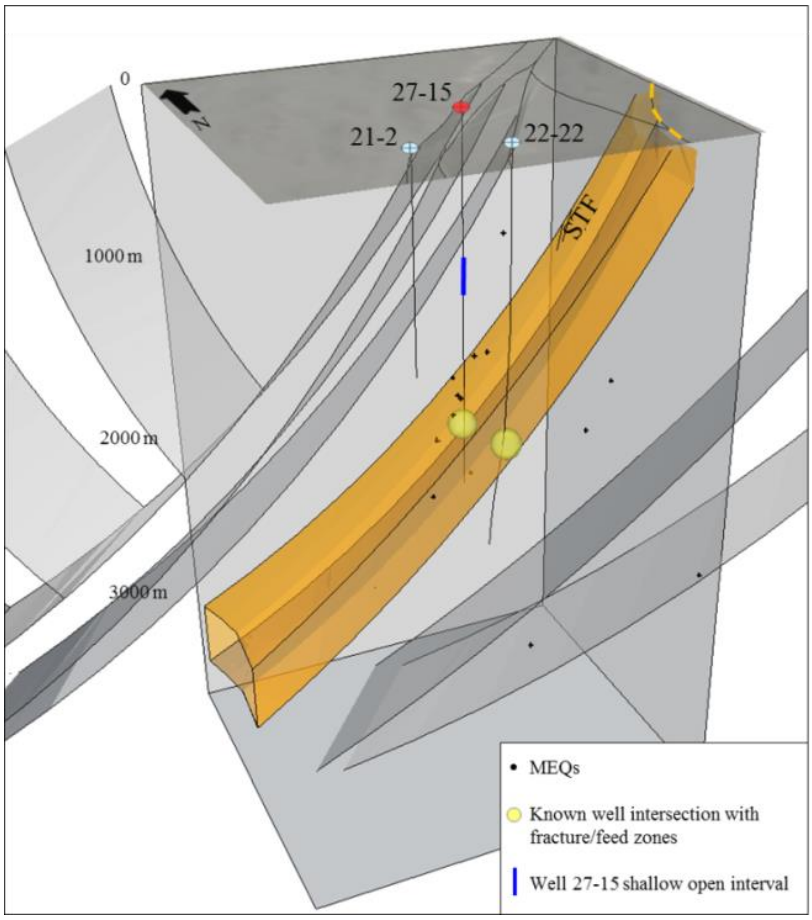

Figure 11 - Conceptual model of the major fault strands of the EGS wellsite (inferred from the Desert Peak geological cross section and map [12][15]). The three-dimensional geometry allows for a visualization at depth of MEQs (April 2-6 2011 - medium flow-rate, shallow stimulation) with respect to the structural setting. Both wells 27-15 and 22-22 encounter a highly-fractured and permeable horizon (Shearing Target Fault *"STF"*) at about 1400 m depth. Most of the MEQs are located at about 1400 m-1600 m depth, which coincides with the STF approximate projection at depth.

Based upon this wellsite conceptualization, we propose that some of the microseismicity observed as part of the EGS project may display shear deformation on the STF as a result of stimulation treatments carried out in well 27-15. As introduced above, injection operations into wells 21-2 and 22-22 also appear to have affected the reservoir pressurization and the development of microseismicity throughout the EGS project. In April 2011, however, the

hypocenters mainly clustered in the vicinity of well 27-15 (at the depth of the STF), suggesting that a cause-effect relation between stimulation operations in well 27-15 and the development of microseismicity primarily existed during the medium to high flow-rate stimulation phases. During the April 2011 medium flow-rate phase, ~15 events (out of 18) are located in the vicinity of the STF. Taking into account the hypocenter errors, the most likely structure which generated the majority of the observed MEQs remains the STF with its surrounding damaged rock volume (Figure 12). Toward the end of the April 2011 medium flow-rate phase, few MEQs (n. 3) appear closer to the open-hole section; their timing and location may be associated with a slight cooling/strain of the reservoir or a subordinate slip triggered by thermal damage on well-oriented sub-sets of existing natural fractures. It is difficult to define with certitude the role and origin of these (minor) events, though most of the permeability gain for this phase is observed prior to their occurrence. A more precise seismic velocity model derived from double-difference tomography (in progress) may better constrain their location and significance.

This conceptual model of a deep hydrologic connection between well 27-15 and wells to the SSW provides a basis on which to test potential mechanisms occurring during the Desert Peak EGS experiment and explains the relation between hydraulic treatment and observed microseismic response. Whether or not the deformation associated with the MEQs as a result of the stimulation treatment also caused the observed transmissivity enhancements needs to be demonstrated and is the subject of a parallel study. An element of note is that any hydraulically-conductive structural feature (which may provide a connection with the rest of the reservoir) potentially associated with MEQ occurrence (~400 m deeper than the shallow stimulation zone) would be isolated from the upper interval in the well because of the plug-back.

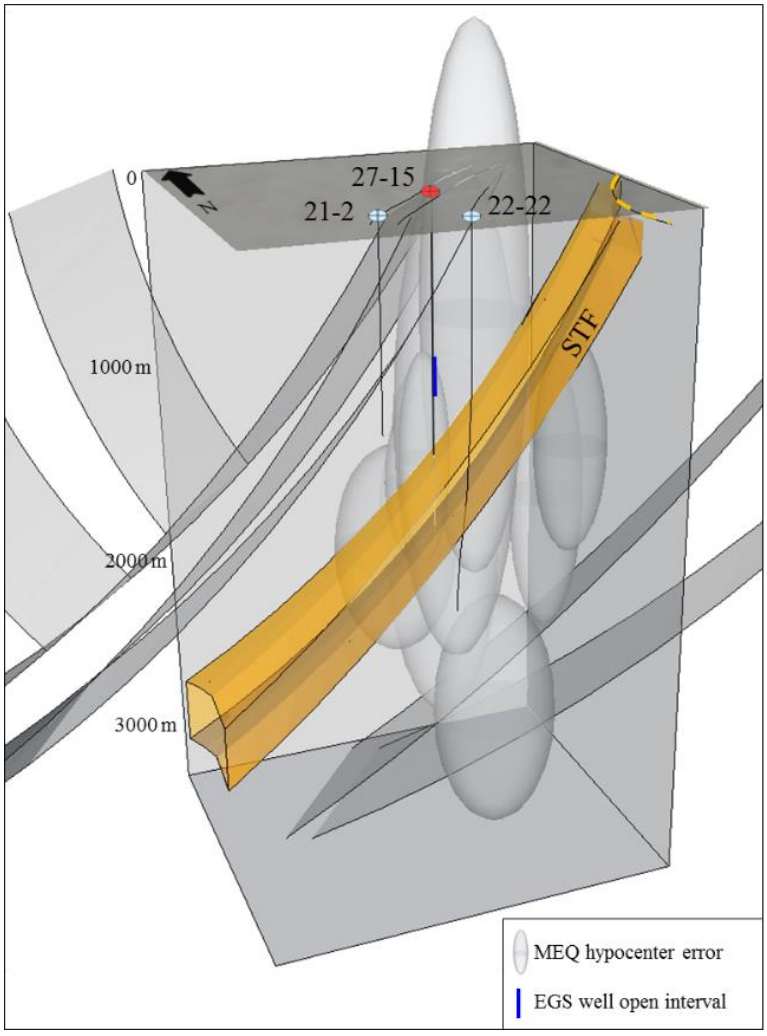

Figure 12 - Graphic representation of the hypocenter error for events observed during the April 2011 medium flow-rate stimulation phases. The structural feature most likely intersecting (thus probably generating) the majority of the MEQ hypocenter errors appears to be the STF (*Shearing Target Fault* discussed in paragraph 3).

However, it is critical to understand the significance of the observed microseismicity and whether it might have highlighted potential structures to target as part of the stimulation strategy. One purpose of the modeling presented here is to test this hypothesis to see if it is consistent with known structural and stress characteristics of the EGS site and with the pore pressure generated during the April 2011 stimulation operations. In this scenario, the resulting transmission of

hydraulic pressure increase within the STF is presumed to have triggered shear failure of sufficient magnitude to result in observable MEQs. This plastic deformation might in turn have enhanced permeability and fluid transmission along the STF, but – as mentioned above – this is verified in a companion study.

The STF is ~400 m deeper than the interval of fluid egress when injecting into the shallow open-hole section of well 27-15. Nevertheless, pore-pressure diffusion can interact with distant, pre-existing structures favorably oriented to failure within the regional stress field, and can initiate slip with associated microseismicity [23]. This possibility is assessed here through coupled hydro-mechanical numerical modeling. The migration of a pressure front through pore pressure diffusion is defined by many authors as *hydraulic diffusivity* [47] [33] [40] [37] [38]. As a general rule, the shape of induced seismicity appears to be controlled by hydro-mechanical coupling (i.e., pressure-fracture interaction) rather than by homogeneous hydraulic diffusivity through a rock mass [6].

4 TECHNICAL APPROACH

The above conceptual model is tested for consistency against observations made before and during the Desert Peak EGS shallow stimulation. Hydro-mechanical modeling techniques are employed to assess the permeability of the triple-well reservoir (27-15, 22-22 & 21-2), and to evaluate the potential for initiating shear failure along the STF due to fluid over-pressurization.

4.1 FLAC3D Coupled Hydro-Mechanical Response Model

The conceptual model is tested against the April 2011 shallow, medium flow-rate injection phase via a numerical simulation with the mechanical-flow code FLAC3D. FLAC3D is a three-dimensional explicit finite-difference program for continuum mechanics computation which also models fluid flow and its corresponding poromechanical effects [25]. The simulation consists of hydro-mechanically coupled calculations evaluating any expected mechanical deformation in

response to injection-induced pore pressure changes within the reservoir and the STF. The FLAC3D failure envelope corresponds to a Mohr-Coulomb criterion (shear yield function) with tension cutoff (tension yield function) and the position of a stress point on this envelope is controlled by a non-associated flow rule for shear failure, and an associated rule for tension failure [25]. Zones in the model behave according to mechanical parameters of the material they represent and following the FLAC3D yield criterion.

As introduced above, the April 2011 shallow, medium flow-rate stimulation phase is a good candidate for this simulation. Therefore, the pressure diffusion model through the reservoir is tuned to cause plastic deformation that could produce MEQs in response to the injection rates applied into 27-15, 22-22 and 21-2 during this phase. Sufficient pressure to reduce the effective normal stress must be communicated to the STF to satisfy the conditions for Mohr-Coulomb failure. The relative pressure perturbation effect from injection into each different well is investigated as part of the modeling exercise presented below.

As a general rule, the simplest geometry compatible with the geology and hypotheses being tested is used to define the FLAC3D model, consistent with the reproduction of key physical processes. In the simplified representation of the wellsite, the model comprises a uniform background formation, three injectors (wells 27-15, 22-22 and 21-2) and a fault zone (STF) dipping ~70° and located ~400 m below the actual 27-15 injection point (Figure 13). The fault zone (STF) in the model is set to be about 100 m thick in order to account for its damage zone (given a fault throw greater than several tens of meters [42]). The grid is aligned with the Rhyolite Ridge Fault Zone and the STF (i.e., with the known tectonic stresses), thus rotated ~20º clockwise from the north. In the vicinity of well 27-15 the STF is represented sub-parallel to the main Rhyolite Ridge Fault Zone, while it is slightly rotated toward wells 22-22 and 21-2 to account for the apparent step-over discussed in paragraph 3 (Figure 8, Figure 13). The model domain extends for 3000 m in the x-direction, 1800 m in the y-direction and 2600 m in the z-direction. The grid is discretized into

regular cubic zones (100 m per side). The model – as well as the STF – are currently assumed to be single-porosity media. Parallel modeling exercises involving coupling with TOUGHREACT adopt a dual-porosity conceptualization. A phreatic surface is initialized at a depth of 118 m. Below this surface pore pressures follow a linear gradient once the initial force-equilibrium state is reached, i.e., a force-equilibrium is assumed when the maximum unbalanced force and velocity vectors at each gridpoint are small compared to the representative zone forces in the problem.

For simplicity and numerical purposes, the lithological units described in Section 2 are grouped into rock types: *a* corresponding to the basement and rhyolite units (background rock mass), and *b* representing the STF (Table 1). The mechanical parameters used in the model are derived from rock mechanical tests conducted on selected core samples representative of the stimulation interval in well 27-15 [30]. In order to appropriately model the propensity for frictional failure in a fractured reservoir, Mohr-Coulomb properties (friction and cohesion) evaluated from residual compressive strength measurements (residual values after failure) for the Rhyolitic and Metamorphic Basement Units are averaged and assigned to rock type *a*. Elements pertaining to the STF are set with a lower friction angle of 28° and zero cohesion, as in-situ stress measurements in a variety of tectonically-active geological settings suggest that fracture planes well oriented with respect to the stress field are generally cohesionless [20][49] (Table 1).

The model is set with permeable boundary conditions, i.e., the pressure remains constant at the boundaries. Velocity and displacement are fixed at the bottom and sides of the model. Permeability is initialized as explained in par. 3.3 (see below). Consistent with the normal faulting regime observed in the field and using the measured magnitude of S_{hmin} [21], xx, zz and yy stress components vary with depth following the relations among S_{hmin}, S_{Hmax} and S_v (vertical overburden): $S_{Hmax} = (S_{hmin} + S_v)/2$, and $S_{hmin}/S_v \approx 0.61$ [21]. A Mohr-Coulomb plasticity constitutive model is set in FLAC3D to properly represent the onset of shear (frictional) failure. The failure envelope for this constitutive model corresponds to a Mohr-Coulomb criterion which

is expressed in terms of principal stresses σ_1, σ_2 and σ_3. For the Mohr-Coulomb plasticity model, the required properties defined for each material are: (1) bulk and shear moduli, (2) friction and dilation angles, (3) cohesion and (4) tensile strength. The constitutive behavior and associated material properties affect the model response as well as stress perturbations caused by fluid injection [25].

Table 1 - Mechanical properties used in the FLAC3D hydro-mechanical model (from [30]).

Parameter	Background (rock type a)	STF (Rock type b)
Density [g/cm^3]	2.7	2.7
Shear Modulus [MPa]	1.0E+04	1.0E+04
Bulk Modulus [MPa]	2.6E+04	2.6E+04
Friction angle [°]	39	28
Cohesion [MPa]	4.2	0
Tensile strength [MPa]	1.0E+04	1.0E+04

Boundary and initial conditions define the *in-situ* state (i.e., before a change or disturbance is introduced by injection). An initial equilibrium state – during which gravitational stresses develop – is obtained by running the model under dry conditions and through mechanical-only calculations. A second equilibration is then calculated by running flow calculations in parallel with the mechanical modeling, in order to capture the effects of solid-fluid interaction. An alteration is then made (e.g., fluid injection resulting in pore pressure change), and the resulting mechanical response throughout the model is computed. A prescribed volumetric inflow of fluid is assigned to wells 27-15, 22-22 and 21-2 to define the principal fluid sources in the model.

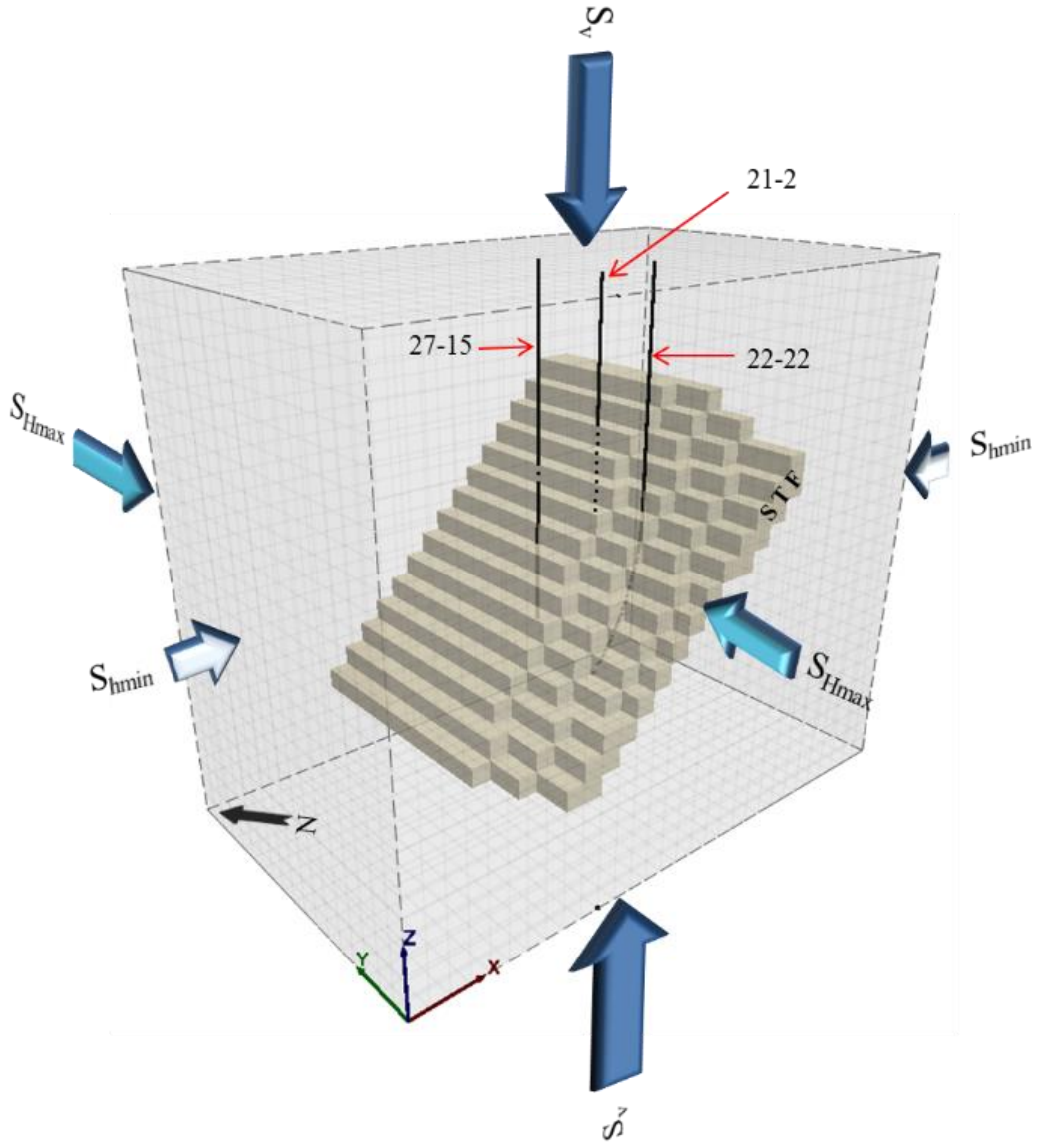

Figure 13 - FLAC3D model construction. The model comprises a uniform background formation, three injectors (27-15, 22-22 and 21-2) and a ~100 m thick NNE-striking, WNW-dipping (70°) Shearing Target Fault (STF). Stresses are applied according to the normal faulting regime observed in the field and using the measured magnitude of S_{hmin} (i.e., σzz>σyy>σxx).

The fluid-mechanical interaction is solved with a coupled approach where the mechanical process is the "slave" module to the master fluid flow process, given that the stress perturbation is pore-pressure driven.

The model simulates the flow-rates injected in: (a) wells 21-2 and 22-22 over the March 24 – April 10, 2011 period, and (b) well 27-15 over the April 01 – April 10, 2011 period. This is done in order to correctly reproduce reservoir pressurization conditions not only during, but also prior to the stimulation treatment of well 27-15. The average volumetric flow-rates applied to the corresponding open-hole sections of the wells are summarized in Table 2.

Table 2 - Average volumetric flow-rates applied to the corresponding open-hole sections in the model when simulating the April 2011 medium flow-rate phase.

Well	Avg. flow-rate [m3/s]	Open-hole section [m] (measured depth)
21-2	0.13	618 – 972
22-22	0.24	1270 – 2051
27-15	0.032	914 - 1067

4.2 Assessment of reservoir permeability

The incorporation of injectors 22-22 and 21-2 in the modeling study of EGS well 27-15 requires a permeability assessment for both the formation comprising well 27-15 (*lower k*) and that around wells 22-22 and 21-2 (*higher k*).

The permeability of the triple-well reservoir considered in this study (27-15, 22-22 and 21-2) is estimated by integrating: (1) pre-EGS baseline permeability-thickness values from injection tests carried out for both the shallow and the extended open interval of well 27-15 [43], (2) detailed, single-wellbore FLAC3D simulation of known wellhead pressure responses to fluid injection, (3) FLAC3D simulation of the 2009 interference test [51] (Figure 10), and (4) DFN analysis from a companion paper [2].

The permeability of the formation surrounding wells 21-2 and 22-22 is estimated by running single-wellbore FLAC3D simulations of the wellhead pressure response to fluid injection, which is best matched using a permeability of ~5.6e-13 m^2.

As per the formation surrounding well 27-15, pre-EGS injection tests revealed a permeability of 2.0e-15 m^2 (5600 md-ft) and of 1.2e-16 m^2 (60 md-ft) for the extended (850 m) and shallow (150 m) open intervals, respectively [43]. The lower permeability in the shallow interval is in agreement with the range of magnitudes obtained from measurements on core plugs under ambient stress conditions [30]. The higher permeability displayed by the extended interval is assumed here to be the result of higher hydraulic conductivity in the STF (intersected by this interval). With this in mind, the 2009 (pre-EGS) interference test [51] is simulated in FLAC3D by applying the permeability values described above to the background formation of well 27-15 (1.2e-16 m^2) and of wells 21-2 and 22-22 (5.6e-13 m^2). The STF permeability is then adjusted until a good fit with the pressure response observed during this test is reached. The best results are obtained when the STF permeability is ~3.0e-14 m^2. The ratio among the three components k_x, k_y and k_z of the permeability tensor computed through DFN analysis in a previous study [2] is maintained and applied to the background formation surrounding well 27-15 to retain the anisotropic permeability distribution of the wellsite (Table 3). The triple-well simulation results of the 2009 interference test – carried out by altering injection flow-rates in wells 21-2 and 22-22 and observing the pressure response in well 27-15 – suggest that the defined permeability is consistent with the reproduction of the field characteristics (Figure 14).

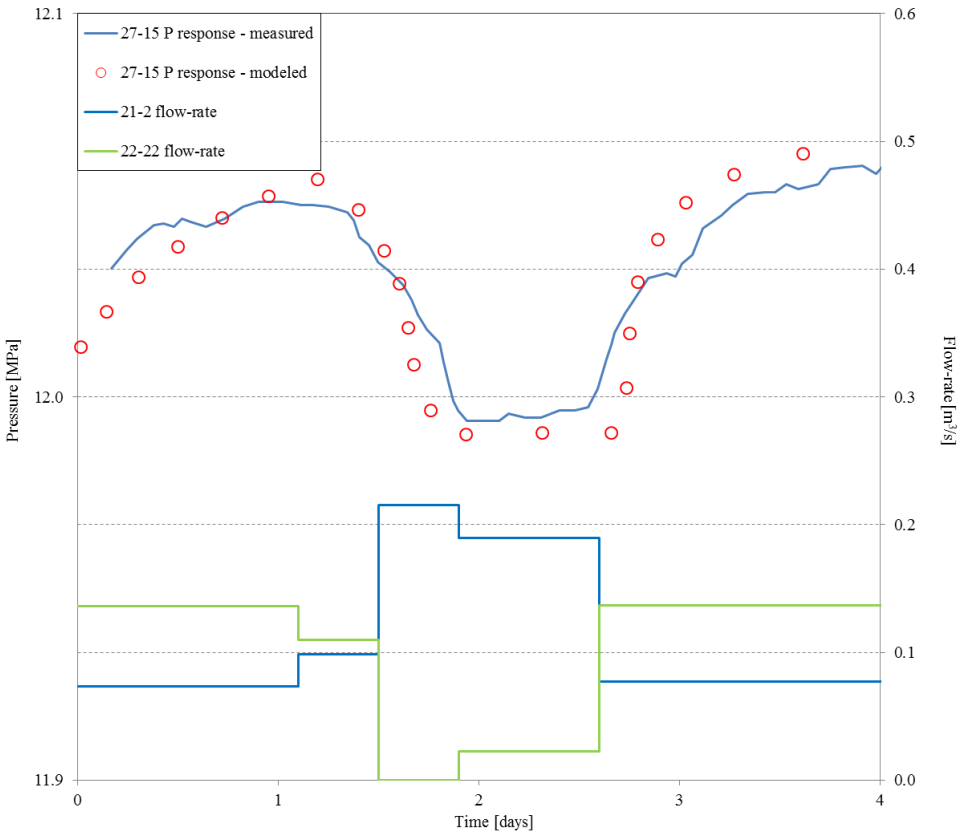

Figure 14 - FLAC3D simulation of the 2009 interference test [51] (Figure 10): pressure response observed in well 27-15 while varying injection flow-rates in wells 22-22 and 21-2. The good fit between measured and modeled pressure curves suggests the permeability field is appropriately initialized.

An element of note is that the April 2011 stimulation (considered in this study) follows the September 2010 phase, during which the permeability of the formation surrounding the well 27-15 shallow interval is considerably improved [4]. Here we estimate this enhanced permeability through single-wellbore FLAC3D simulations of the wellhead pressure response observed during the initial steps of the April 2011 medium flow-rate phase. We do so by increasing the pre-EGS permeability value (1.2e-16 m^2) in the formation surrounding the well 27-15 shallow open interval to ~1.1e-14 m^2, which provides an adequate match with the observed overpressure. This

value is integrated into the permeability field described above to set-up the initial conditions for the April 2011 phase simulation.

Table 3 - Summary of permeability values estimated for: (a) well 27-15 background formation, (b) volumes with permeability enhanced as part of the September 2010 low-flow-rate phase, (c) formation surrounding wells 22-22 and 21-2, and (d) Shearing Target Fault (STF). Anisotropic permeability - derived from DFN analysis [2] - is used for the well 27-15 background formation.

	Model Hydraulic Parameters			
	k [m^2]	*ky*	*kx*	*kz*
(a) Well 27-15 background formation	1.2E-16	1.83E-16	2.50E-17	6.16E-17
(b) September 2010 enhanced k	1.1E-14	-	-	-
(c) wells 22-22 and 21-2 formation	5.6E-13	-	-	-
(d) Shearing Target Fault (STF)	3.0E-14	-	-	-

5 RESULTS

Under the April 2011 shallow, medium flow-rate stimulation conditions, FLAC3D coupled hydro-mechanical simulations display conditions for shear failure pertaining to the stimulated reservoir volumes (i.e., around the open interval and at the depth of the STF). In the model, failure is manifested as a contiguous series of actively failing zones in which stresses satisfy the FLAC3D yield criterion (as defined in par. 4.1) (Figure 15 and Figure 18.A). Conditions for tensile failure also develop in volumes surrounding the well 27-15 open-hole section, in agreement with injection-induced fluid pressures exceeding S_{hmin} during the medium flow-rate phase (Figure 15).

With the parameterization listed in Table 1, results show that shear failure may occur at the depth of the STF (Figure 15) where injection-induced pore pressure increases by more than 1 MPa as a result of the stimulation operation (Figure 16).

Injection-induced pore pressure diffusion computed by FLAC3D is also tested with a Mohr-Coulomb analytical approach to verify if the resulting pressure incremental could satisfy conditions for shear failure on well-oriented sets of fractures at the depth of the STF. The Mohr-Coulomb analysis confirms that this pressure increase within the STF would create critical conditions for shear deformation on well-oriented, cohesionless fractures (Figure 17).

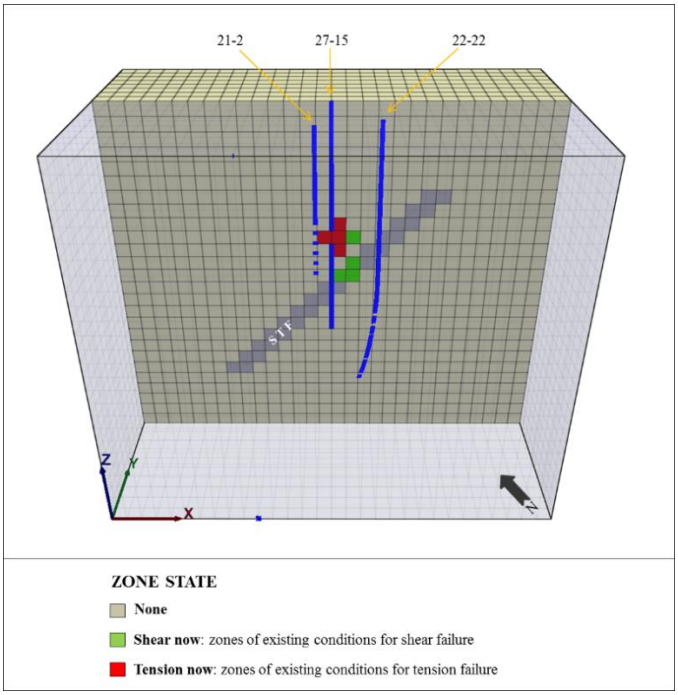

Figure 15 - FLAC3D coupled hydro-mechanical simulation and mechanical response as a result of fluid injection during the April 2011 medium flow-rate stimulation phase. FLAC3D displays conditions for: (1) tension failure in volumes surrounding the well 27-15 open-hole section (in agreement with fluid pressures exceeding S_{hmin}), and (2) shear failure mainly at STF depths. Limited conditions for shear failure also develop in the vicinity of the well 27-15 open interval.

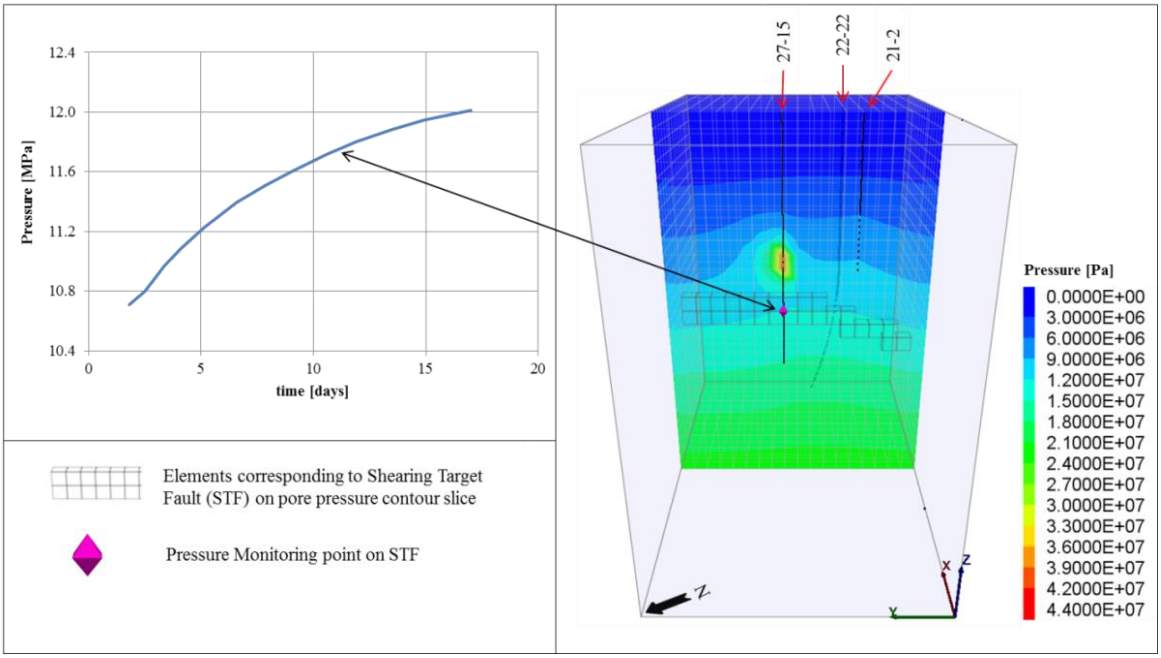

Figure 16 - The April 2011 medium flow-rate stimulation phase is modeled with FLAC3D by simulating fluid injection in the well 27-15 shallow open-hole section and in wells 21-2 and 22-22. Pore pressure diffusion from the well 27-15 shallow open interval combines with pressure from concurrent injection in wells 21-2 and 22-22 - increasing the pore pressure at the depth of the STF by about 1 MPa.

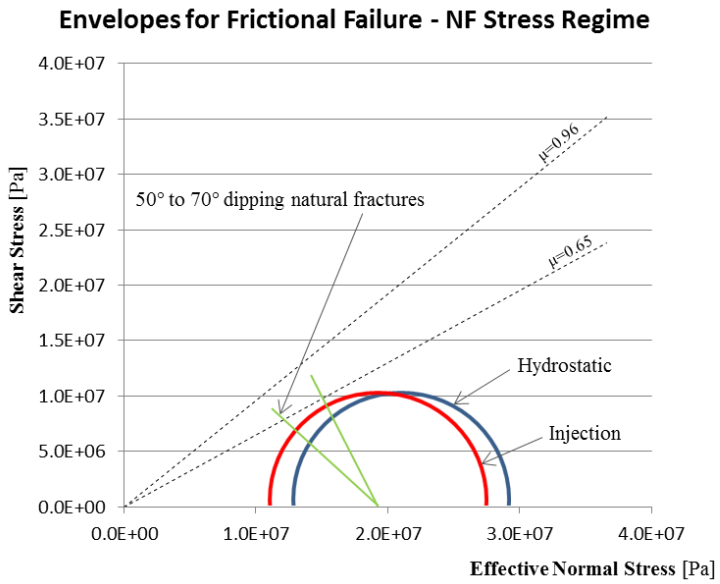

Figure 17 - Normal-stress regime Mohr circles showing shear and effective normal stress at ~1400 m depth (location of MEQs and STF) under: (1) hydrostatic conditions (blue circle) defined assuming a groundwater level 118 m below surface, and (2) April 2011 medium flow-rate injection-induced conditions (red circle) derived from FLAC3D simulation (Figure 16). Frictional failure lines are based on the sliding friction coefficient derived from rock sample laboratory testing from surrounding geological units [30]. In-situ natural and cohesionless fractures at the depth of the STF are close to being critically stressed for shear failure under the April 2011 medium flow-rate phase conditions.

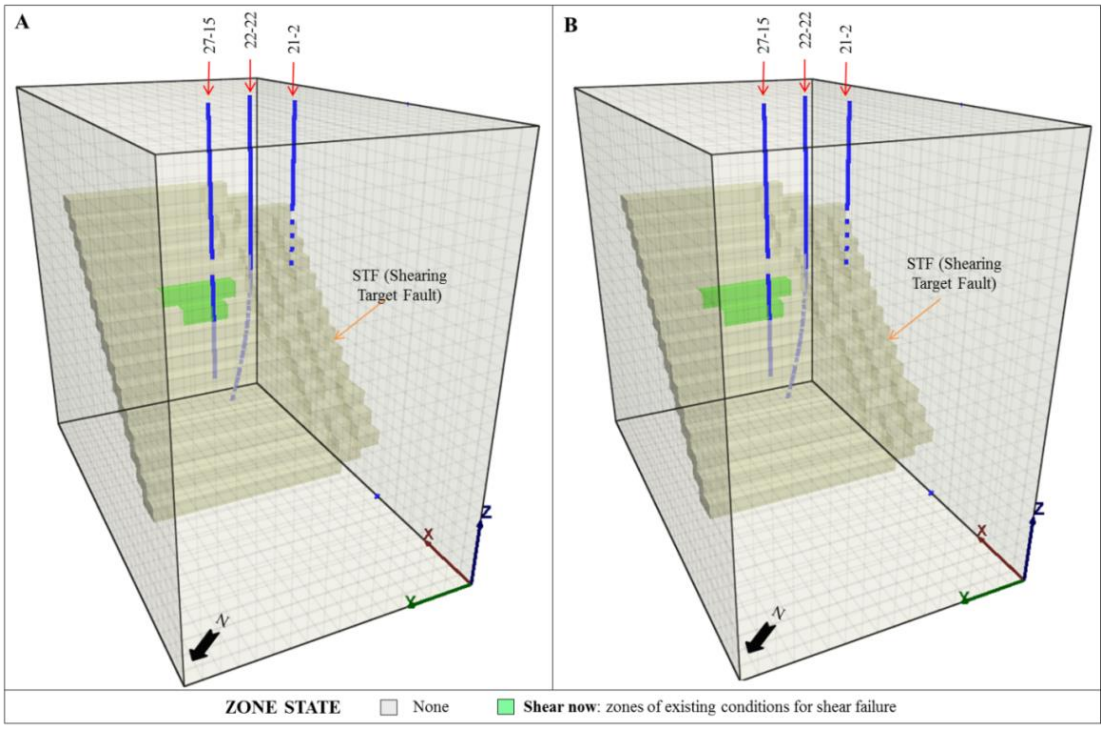

Figure 18 - FLAC3D coupled hydro-mechanical simulation and mechanical response resulting from injection-induced pressure diffusion generated during the April 2011 medium flow-rate stimulation phase. The results display conditions for shear failure developing on the STF in the case of: (A) injection in well 27-15 alone (or concurrent with injection in well 21-2), and (B) concurrent injection into wells 27-15 and 22-22. When the April 2011 phase injection rates are simulated, conditions for shear failure develop on the STF in the vicinity of well 27-15, where the bulk of microseismicity is observed during this phase. Fluid injected in well 21-2 does not seem to influence the development of shear deformation with the current model configuration.

With the current model configuration, simulation results show that shear deformation at the depth of the STF and toward well 27-15 is enhanced when both wells 27-15 and 22-22 are actively injecting fluid (Figure 18.B). Pore pressure diffusion from concurrent injection in wells 27-15 and 22-22 combine, further destabilizing the STF. Fluid injection simulation into well 22-22 alone or simultaneously into wells 22-22 and 21-2 is insufficient to develop conditions for shear failure.

Fluid injection into well 21-2 does not seem to impact the development of deformation on the STF.

Shear failure distribution shown in the modeling results is in agreement with the microseismicity observed during the April 2011 phase, which appears to cluster mainly in the same depth range of the STF below the shallow stimulated interval of well 27-15 (Figure 4).

6 DISCUSSION AND CONCLUSIONS

In order to define a possible connection between stimulation operations in well 27-15 and the development of the observed MEQs, as well as to offer a possible explanation for their deep location, the present study analyzes: (1) 3D site-specific geometry of the key structures involved in the experiment, (2) assessment of permeability distribution based on integrating DFN analysis, injectivity tests, pressure response modeling and interference test modeling, (3) hydro-mechanical simulation of pore pressure diffusion and resulting mechanical deformation consistent with the activation of hydraulically-induced shear failure in the reservoir.

The MEQ clusters observed during the EGS experiment are mainly used for structural identification purposes. The numerical simulation honors the April 2011 medium flow-rate injection phase, when MEQs appear grouped together in volumes closer to well 27-15, if compared to microseismic swarms observed at other times.

The reservoir's mechanical response resulting from injection operations into the well 27-15 shallow open-hole section (April 2011 conditions) is simulated in FLAC3D to verify possible conditions for deformation and shear failure initiation. The conceptual and numerical modeling results reveal that pore pressure diffusion to depths below the stimulation interval during the April 2011 EGS shallow injection phase in well 27-15 – especially if combined with injection operations in well 22-22 – can lead to pressurization and poromechanical stressing of the STF.

Modeling results display shear failure affecting reservoir volumes at depths associated with the STF. The location of zones indicating conditions for shear failure is in agreement with the microseismicity distribution observed during this phase: mainly clustered at the depth of – and aligned with – the STF. The model suggests that rapid and considerable changes in the injection flow-rates cause a sudden modification of the stress state, destabilizing the STF considerably.

These results (i.e., pressure diffusion → conditions for shear failure on the STF) support the proposed STF-based conceptual model framework, which correctly reproduces the cause-effect relation between well 27-15 stimulation operations and the development of microseismicity – especially when concurrent with injection in well 22-22. This interaction between well 27-15 and well 22-22 is in agreement with both (a) the 2009 pressure interference test, which suggests that well 22-22 can deliver some pressure towards well 27-15, and (b) the absence of microseismicity in the vicinity of well 27-15 prior to the stimulation treatment. This is consistent with the concept proposed in other experiments, e.g. Soultz, where simultaneous injection into adjacent wells (or "*focused stimulation*") delivered the most effective stimulation and hydraulic connection development [39][1][19].

The FLAC3D simulation indicates localized pore pressure incremental up to 1 MPa at the depth of the STF and suggests that effective stress changes induced by these fluid pressure increases are sufficient to produce slip (and possibly microseismicity) within the STF. This is also confirmed by evaluating the resulting effective pore pressure through a Mohr-Coulomb analysis (Figure 17). Both numerical (coupled hydro-mechanical) and analytical (Mohr-Coulomb) results support the existence of regions in the STF which can undergo shear failure under the April 2011 injection-induced hydraulic pressure conditions. Whether a correlation between shearing deformation and the observed changes in injectivity exists needs to be verified and is part of a parallel study.

The parameters under which the model simulates this process for the April 2011 medium flow-rate phase are listed in Table 1 and Table 3. The selected STF friction angle (Table 1) provides

the most realistic results; higher values involve no shear deformation on the STF, while lower values cause too large a failing STF surface. Future modeling work may attempt to further calibrate the simulated shear deformation with the magnitude of the observed microseismicity, in order to better constrain the model parameterization and the extent of reservoir volumes affected by plastic deformation.

The identified STF satisfies some of the conditions that are necessary for shear failure initiation: (1) adequate initial transmissivity, and (2) optimum orientation with respect to the local stress state [32]. The initial STF transmissivity may be further enhanced by slip [32]. Related physical processes have been inferred in several injection-disposal operations, especially along faults that transit between basement rocks and overlying aquifers. Such a process may have been responsible for the recent observation of injection-induced seismicity at Guy, Arkansas [24]. Several studies show that the injection-induced fluid pressurization can propagate through the reservoir at a kilometer scale and generate seismic events with time (including fault reactivation) [26][27]. The injected fluid pressure diffusion and fluid migration from the formation surrounding this shallow open-hole section toward the deeper reservoir might also have been facilitated by: (a) downward migration of cooler (denser) injected fluids [27][48], (b) natural fracture networks characterized by higher N-S and vertical permeability [2], and (c) leakage through the cement plug at the base of the shallow open-hole section or through the drilling-induced damage in the formation. A further element of note is that the pressure required to trigger slip on pre-existing fractures may decrease with depth [34].

The core theories of this study were laid out in the summer of 2012 [2]. Well 27-15 was afterwards re-completed to the original depth (about 1770 m) in November 2012 and a new, full-hole stimulation phase was performed between January and March 2013 [22]. Further injectivity gains (more than 10-fold increase since initial, pre-EGS conditions) associated with more than 200 MEQs were observed during this latest stimulation phase [22]. The MEQs recorded during

the 2013 extended open-hole section stimulation and during the previous shallow 2010/11 stimulation operations both display analogous orientation and location at depth (Figure 19). It appears that the 2013 extended open-hole section stimulation improved access to the deeper STF discussed in this study. Direct stimulation of the STF might have provided the final desired commercial injectivity, suggesting that targeting the STF was a key decision in the stimulation plan. This investigation is part of a parallel study.

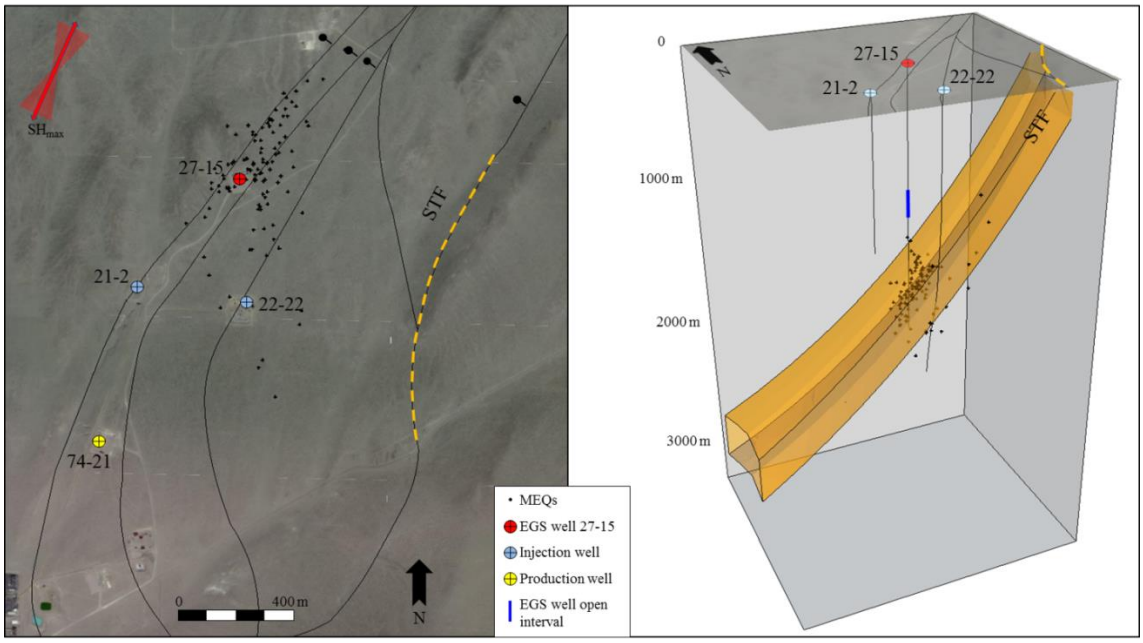

Figure 19 - Map & 3D view of the induced microseismicity observed between January 15-20, 2013. Over this period, the EGS well 27-15 extended open interval is being stimulated. The events appear located around well 27-15 and at the depth of the STF (*Shearing Target Fault*, discussed in paragraph 3). SHmax direction inferred from observation of borehole failures in well 27-15 [8][21]. Black lines show surface trace of interpreted faults [15]; larger black dots shown on downthrown sides of normal faults.

Thermal stresses and thermal damage may also have been generated by the injection of cooler fluid during the April 2011 stimulation phase. Thermal effects during the September 2010 low

flow-rate phase are discussed in [7], [31] and [10]. Thermal effects are considered when modeling all stages of the Desert Peak EGS stimulation as part of the ongoing FLAC3D-TOUGHREACT study, although their influence is believed to be small at the depth where the bulk of the microseismicity is observed. In this study, the simulation exercise is based on a comprehensive conceptual model which incorporates geological, structural and borehole data.

Given the non-uniqueness of the problem, the presented conceptual framework is one possible model for the Desert Peak EGS experiment. Coupling of thermo-hydro-mechanical processes are carried out as part of a parallel study to better understand the evolution of permeability throughout the Desert Peak EGS project. The distribution of induced microseismicity seems to be controlled in a complex way by concurrent injection operations in wells 27-15 and 22-22. The conceptual framework provides a geologically-reasonable model for the April 2011 Desert Peak EGS experiment in that it tests the role of the STF in focusing induced deformation manifested by MEQs. However, this type of model is inherently non-unique due to uncertainties in the geologic structure and physical properties that influence thermo-hydro-mechanical coupled processes.

ACKNOWLEDGMENTS

This work was supported by the Desert Research Institute through a DHS fund, by the Great Basin Center for Geothermal Energy under a Geothermal Technology Program (GTP) Faculty Seed Grant, by Ormat Technologies, Inc., and by the Itasca Education Partnership program. The first author wishes to acknowledge Prof. Jim Faulds and Prof. Greg Pohll for their comments/feedback while reviewing the document.

REFERENCES

[1]. Baria, R., Jung, R., Tischner, T., Nicholls, J., Michelet, S., Sanjuan, B., Soma, N., Asanuma, H., Dyer, B., Garnish, J., Creation of an HDR Reservoir at 5000 m Depth at the European HDR Project, Proceedings 31st Workshop on Geothermal Reservoir Engineering, Stanford University, Stanford, California, January 30 – February 1, 2006.

[2]. Benato, S., Reeves, D.M., Parashar, R., Davatzes, N.C., Hickman, S., Elsworth, D., Spielman, P., Taron, J., Computational Investigation of Hydro-Mechanical Effects on Transmissivity Evolution During the Initial Injection Phase at the Desert Peak EGS Project, NV, Proceedings, 38th Workshop on Geothermal Reservoir Engineering, Stanford University, Stanford, California, February 11-13, 2013, SGP-TR-198.

[3]. Chabora, E., Zemach, E., Desert Peak EGS Project, Geothermal Technologies Program 2013 Peer Review, DOE Award: DE-FC6-02ID14406.

[4]. Chabora, E., Zemach, E., Spielman, P., Drakos, P., Hickman, S., Lutz, S., Boyle, K., Falconer, A., Robertson-Tait, A., Davatzes, N.C., Rose, P., Majer, E., Jarpe, S., Hydraulic stimulation of well 27-15, Desert Peak Geothermal Field, Nevada, USA, Proceedings, 37th Workshop on Geothermal Reservoir Engineering, Stanford University, Stanford, California, January 30 - February 1, 2012, SGP-TR-194.

[5]. Cladouhos, T.T., Osborn, W.L., Petty, S., Bour, D., Iovenitti, J., Callahan, O., Nordin, Y., Perry, D., Stern, P., Newberry volcano EGS demonstration – phase I results, Proceedings, 37th Workshop on Geothermal Reservoir Engineering, Stanford University, Stanford, California, January 30 - February 1, 2012, SGP-TR-194.

[6]. Cornet, F.H., (2000), Comment on 'Large-scale in situ permeability tensor of rocks from induced microseismicity', Geophys. J. Int., 140.

[7]. Danko, G., Bahrami, D., Zheng, L., Coupled Multiflux-Tough2-Toughreact T-H-M-C model for EGS studies, Proceedings, TOUGH Symposium 2012, Lawrence Berkeley Laboratory, Berkeley, California, September 17-19, 2012.

[8]. Davatzes, N.C. and Hickman, S., Fractures, stress and fluid flow prior to stimulation of well 27-15, Desert Peak, Nevada, EGS project, Proceedings, 34th Workshop on Geothermal Reservoir Engineering, Stanford University, Stanford, California, February 9-11, 2009, SGP-TR-187.

[9]. Davatzes, N.C., and Hickman, S.H. (2010), Stress, fracture, and fluid-flow analysis using acoustic and electrical image logs in hot fractured granites of the Coso geothermal field, California, U.S.A.,

in M. Poppelreiter, C. Garcıa-Carballido, and M. Kraaijveld, eds., Dipmeter and borehole image log technology: AAPG Memoir 92, Ch 24., p. 1 – 35.

[10]. Dempsey, D., Kelkar, S., Lewis, K., Hickman, S., Davatzes, N., Moos, D., Zemach, E., Modeling Shear Stimulation of the Desert Peak EGS Well 27-15 Using a Coupled Thermal-Hydrological-Mechanical Simulator, Proceedings 47th US Rock Mechanics/Geomechanics Symposium, San Francisco, California, USA, 23-26 June 2013.

[11]. Faulds, J.E., and Henry, C.D., (2008), Tectonic influences on the spatial and temporal evolution of the Walker Lane: an incipient transform fault along the evolving Pacific-North American plate boundary, in Spencer, J.E., and Titley, S.R., eds., Ores and orogenesis: CircumPacific tectonics, geologic evolution, and ore deposits, Arizona Geological Society Digest 22, p. 437-470.

[12]. Faulds, J.E., Coolbaugh, M.F., Benoit, D., Opplinger, G., Perkins, M., Moeck, I., Drakos, P., Structural controls of geothermal activity in the Northern Hot Spring Mountains, Western Nevada: the tale of three geothermal systems (Brady's, Desert Peak, and Desert Queen), Geothermal Resources Council Transactions, Vol. 34, 2010.

[13]. Faulds, J.E., Hinz, N., Kreemer, C., Coolbaugh, M., Regional Patterns of Geothermal Activity in the Great Basin Region, Western USA: Correlation With Strain Rates, Geothermal Resources Council Transactions, Vol. 36, 2012.

[14]. Faulds, J.E., Hinz, N.H., Siler, D. L., Coolbaugh, M. F., Queen, J.H., Zemach, Ezra, Structural Controls on the Bradys Geothermal System, Western Nevada: Insights from Integrated Geologic, Geophysical, and 3D Characterization, 125th Anniversary Annual Meeting & Expo, The Geological Society of America, 27-30 October 2013, Denver, Colorado, USA.

[15]. Faulds, J.E., Ramelli, A.R., Garside, L.J., Coolbaugh, M.F., and Green, H.L., (2012), Preliminary geologic map of the Desert Peak Quadrangle, Churchill County, Nevada, Nevada Bureau of Mines and Geology Open-File Report 12-5, scale 1:24,000.

[16]. Genter, A., Cuenot, N., Melchert, B., Moeckes, W., Ravier, G., Sanjuan, R., Scheiber, J., Schill, E., Schmittbuhl, J., Main achievements from the multi-well EGS Soultz project during geothermal

exploitation from 2010 and 2012, Proceedings, European Geothermal Congress 2013, Palazzo dei Congressi - Pisa, Italy June 3-7, 2013.

[17]. Genter, A., Fritsch, D., Cuenot, N., Baumgartner, J., Graff, J.J., Overview of the current activities of the European EGS Soultz project: from exploration to electricity production, Proceedings, 34th Workshop on Geothermal Reservoir Engineering, Stanford University, Stanford, California, February 9-11, 2009, SGP-TR-187.

[18]. Hammond, W.C., and Thatcher, W., (2004), Contemporary tectonic deformation of the Basin and Range province, western United States: 10 years of observation with the Global Positioning System, Journal of Geophysical Research, v. 109, B08403, doi: 10.1029/2003JB002746.

[19]. Hettkamp, T., Baumgärtner, J., Baria, R., Gérard, A., Gandy, T., Michelet, S., Teza, D., Electricity Production from Hot Rocks, Proceedings, 29th Workshop on Geothermal Reservoir Engineering, Stanford University, Stanford, California, January 26-28, 2004.

[20]. Hickman, S. (1991), Stress in the lithosphere and the strength of active faults, U.S. National Report to the International Union of Geodesy and Geophysics 1987-1990, Reviews of Geophysics, v. 29, p. 759-775.

[21]. Hickman, S. and Davatzes, N.C., In-situ stress and fracture characterization for planning of an EGS stimulation in the Desert Peak Geothermal field, Nevada, Proceedings, 35th Workshop on Geothermal Reservoir Engineering, Stanford University, Stanford, California, February 1-3, 2010 SGP-TR-188.

[22]. Hickman, S., Davatzes, N.C., Zemach, E., Chabora, E., Lutz, S., Majer, E., Spielman, P., Robertson-Tait, A., Rose, P., Dempsey, D., Kelkar, S., Moos, D., Stress and Fracture Characterization for EGS Stimulation: The Desert Peak Project, Abstract Volume 2013, International Conference on EGS, Potsdam, Germany, May 27, 2013.

[23]. Holland, A., Examination of Possibly Induced Seismicity from Hydraulic Fracturing in the Eola Field, Garvin County, Oklahoma, Oklahoma Geological Survey Open-file, OF1-2011.

[24]. Horton, S., Disposal of hydrofracking waste fluid by injection into subsurface aquifers triggers earthquake swarn in central Arkansas with potential for damaging earthquake, Seismological Research Letters, Vol. 83, Number 2, March/April 2012.

[25]. Itasca FLAC3D manual, Fast Lagrangian Analysis of Continua in 3 Dimensions - version 4.0. Minneapolis, MN, Itasca Consulting Group Inc., 2011.

[26]. Izadi, G., Elsworth, D., The influence of thermal-hydraulic-mechanical- and chemical effectson the evolution of permeability, seismicity and heat production ingeothermal reservoirs, Geothermics 53 385–395, 2015.

[27]. Jeanne, P., Rutqvist, J., Vasco, D., Garcia, J., Dobson, P.F., Walters, M., Hartline, C., Borgia, A., Development of a 3D hydrogeological and geomechanical model of an Enhanced Geothermal System using microseismic and ground deformation data from a 1-year injection program, Proceedings, 39th Workshop on Geothermal Reservoir Engineering, Stanford University, Stanford, California, February 24-26, 2014, SGP-TR-202.

[28]. Larsen, P.H., (1988), Relay structures in a lower Permian basement-involved extensional system, East Greenland, Journal of Structural Geology, v.10, p 3-8.

[29]. Lutz, S., Moore, J., Jones, C., Suemnicht, G., and Robertson-Tait, A., Geological and structural relationships in the Desert Peak Geothermal System, Nevada: Implications for EGS development, Proceedings 34th Workshop on Geothermal Reservoir Engineering, Stanford University, Stanford, California, February 9-11, 2009, SGP-TR-187.

[30]. Lutz, S.J., Hickman, S., Davatzes, N., Zemach, E., Drakos, P., Robertson-Tait, A., Rock mechanical testing in support of well stimulation activities at the Desert Peak geothermal field, Nevada, Geothermal Resources Council Transactions, Vol. 34, 2010.

[31]. McClure, M., Horne, R., Characterizing Hydraulic Fracturing with a Tendency for Shear Stimulation Test, The Society of Petroleum Engineers Annual Conference and Exibition, New Orleans, Louisiana, USA, 30 September–2 October 2013, SPE 166332-MS.

[32]. McClure, M., Horne, R., Is pure shear stimulation always the mechanism of stimulation in EGS?, Proceedings, 38th Workshop on Geothermal Reservoir Engineering, Stanford University, Stanford, California, February 11-13, 2013, SGP-TR-198.

[33]. Nicholson, C., Wesson, R.L., (1990), Earthquake Hazard Associated With Deep Well Injection - A Report to the U.S. Environmental Protection Agency, U.S. Geol. Surv. Bull, 1951, pp. 74.

[34]. Pine, R.J., Batchelor, A.S., (1984), Downward Migration of Shearing in Jointed Rock During Hydraulic Injections, Int. J. Rock Mech. Min. Sci. & Geomech. Abstr. Vol. 21, No. 5, pp. 249-263, 0148-9062/84.

[35]. Robertson-Tait, A., Lutz, S.J., Sheridan, J., and Morris, C.L., Selection of an interval for massive hydraulic stimulation in well DP 23-1, Desert Peak East EGS project, Nevada, Proceedings, 29th Workshop on Geothermal Reservoir Engineering, Stanford University, Stanford, California, January 26-28, 2004, SGP-TR-175.

[36]. Rose, P., Leecaster, K., Drakos, P., Robertson-Tait, A., Tracer testing at the Desert Peak EGS Project, Geothermal Resource Council Transactions, Vol. 33, 2009.

[37]. Rothert, E., Shapiro, S.A., (2003), Microseismic monitoring of borehole fluid injections: Data modeling and inversion for hydraulic properties of rocks, Geophysics, 68(2**)**, p. 685-689.

[38]. Rozhko, A.Y., (2010), Role of seepage forces on seismicity triggering, J. Geophys. Res., 115, doi:10.1029/2009JB007182.

[39]. Schlinder, M., Baumgärtner, J., Gandy, T., Hauffe, P., Hettkamp, T., Menzel, H., Penzkofer, P., Teza, D., Tischner, T., Wahl, G, Successful Hydraulic Stimulation Techniques for Electric Power Production in the Upper Rhine Graben, Central Europe, Proceedings World Geothermal Congress, Bali, Indonesia, 25-29 April 2010.

[40]. Shapiro, S.A., Audigane, P., Royer, J.J. , (1999), Large-scale in situ permeability tensor of rocks from induced microseismicity, Geophys. J. Int., 137, p. 207-213.

[41]. Sherburn, S. and Quinn, R., An Assessment of the Effects of Hydraulic Fracturing on Seismicity in the Taranaki Region, (2012), GNS Science Consultancy Report 2012/50, February 2012.

[42]. Shipton, Z.K., Soden, A.M., Kirkpatrick, J.D., Bright, A.M., Lunn, R.J., How thick is a fault? Fault-Displacement-Thickness scaling revisited, in Abercrombie, R., (Eds) Earthquakes: Radiated energy and the physics of faulting, pp. 193-198, AGU bulletin, 2006.

[43]. Stacey, R.W., Robertson-Tait, A., Drakos, P., Zemach, E., EGS stimulation of well 27-15, Desert Peak geothermal field, Nevada, Geothermal Resource Council Transactions, Vol. 34, 2010.

[44]. Stewart, J.H., and Perkins, M.E., (1999), Stratigraphy, tephrochronology, and structure of part of the Miocene Truckee Formation in the Trinity Range- Hot Springs Mountains area, Churchill County, east-central Nevada: USGS Open-File Report 99-330.

[45]. Swyer, M.W., Davatzes, N.C., Evaluating the Role of the Rhyolite Ridge Fault System in the Desert Peak Geothermal Field with Robust Sensitivity Testing Through Boundary Element Modeling and Likelihood Analysis, Proceedings, 38th Workshop on Geothermal Reservoir Engineering, Stanford University, Stanford, California, February 11-13, 2013, SGP-TR-198.

[46]. Swyer, M.W., Davatzes, N.C., Using boundary element modeling of fault slip to predict patterns of stress perturbation and related fractures in geothermal reservoirs and explore parameter uncertainty, Proceedings, 37th Workshop on Geothermal Reservoir Engineering, Stanford University, Stanford, California, January 30 – February 1, 2012, SGP-TR-194.

[47]. Talwani, P., Acree, S., Pore Pressure Diffusion and the Mechanism of Reservoir-Induced Seismicity, Pageoph, 122, p. 947-965.

[48]. Taron, J., Hickman, S., Ingebritsen, S.E, and Williams, C., Using a fully coupled, open-source THM simulator to examine the role of thermal stresses in shear stimulation of enhanced geothermal systems, 48th US Rock Mechanics / Geomechanics Symposium held in Minneapolis, MN, USA, 1-4 June 2014, ARMA 14-7525.

[49]. Townend, J., and Zoback, M. D., (2000), How faulting keeps the crust strong, Geology, v. 28, p. 399–402.

[50]. Wyborn, D., Hydraulic Stimulation of the Habanero Enhanced Geothermal System (EGS), South Australia, 5th BC Unconventional Gas Technical Forum April 2011, Geodynamics Limited.

[51]. Zemach, E., Drakos, P., Robertson-Tait, A., Lutz, S.J., Feasibility evaluation of an “in-field” EGS project at Desert Peak, Nevada, USA, Proceedings World Geothermal Congress, Bali, Indonesia, 25-29 April 2010.

5. MANUSCRIPT III - DESERT PEAK EGS: MECHANISMS INFLUENCING PERMEABILITY EVOLUTION INVESTIGATED THROUGH DUAL-POROSITY SIMULATOR TFREACT

Stefano Benato[1,#] and Joshua Taron[2]

1 - Division of Hydrologic Sciences, Desert Research Institute, Reno, NV, 89512 USA

2 - U.S. Geological Survey, Menlo Park, CA, 94025 USA

Corresponding author: E-mail: stefano.benato@gmail.com

ABSTRACT

The reservoir response associated with selected phases of the hydraulic stimulation conducted as part of the 2010-2013 Desert Peak Enhanced Geothermal System (EGS) project is investigated through the dual-porosity numerical simulator TFReact v2.0 introduced by *Taron et al., 2009.* TFReact couples the solid mechanics (M) analyses of FLAC3D with the multiphase, non-isothermal and reactive capabilities (THC) of TOUGHREACT, and allows for a comprehensive investigation of the major thermal-hydraulic-mechanical-chemical (THMC) physical processes occurring in deep, tight rock masses subject to circulation of pressurized fluids. Numerical simulations are performed to determine: a) pore pressure diffusion and stress field modifications, b) development of mechanical deformation, and, above all c) relative impact of tensile vs. shear deformation on the evolution of the reservoir permeability. A triple-well reservoir model is implemented to account for the combined influence of concurrent injection in wells 27-15 (EGS well), 22-22 and 21-2 (active injectors). This study simulates selected stimulation treatments

carried out from 914 m to 1067 m (*shallow* stimulation interval) and from 917 m to 1771 m (*extended* stimulation interval). Alternative hydraulic stimulation schemes/scenarios (by assuming diverse varying injectate properties and injection durations) are modeled over the two stimulation intervals to test if and how the final permeability could have been further improved.

Simulated permeability modifications appear to be predominantly governed by thermo-hydro-mechanical dilation (elastic) during stimulation of the *shallow* interval and by hydro-mechanical deformation (inelastic shear) during stimulation of the *extended* interval. Inelastic shear deformation delivers higher permeability gains, and in the shortest time, only if hydraulically-conductive and well-oriented features are targeted with the stimulation treatment. TFReact numerical simulations combined with a detailed site conceptualization and microseismicity interpretation provide further understanding of injection-induced mechanisms.

1 INTRODUCTION & BACKGROUND

A series of stimulation treatments were carried out in Desert Peak well 27-15 as part of a DOE-funded EGS (Enhanced Geothermal System) project over a time-frame that stretched from Sep 2010 to Mar 2013. The overall approach involved injecting spent brines at different temperatures with variable wellhead pressures into well 27-15 over different durations of time with the intent of enhancing the formation permeability and improving the connection to the rest of the reservoir [4][17].

Well 27-15 was originally drilled to a total depth of about 1771 m, with the completed open interval (914 m-1771 m) displaying a baseline injectivity (*flow-rate/pressure*) of ~1.8 kg/s/MPa (~0.2 gpm/psi) [40][51]. In 2010 it was plugged back to a total depth of about 1067 m, with the completed open-hole section available for stimulation extending from 914 m to 1067 m (here referred to as the "*shallow*" stimulation interval) and displaying a baseline injectivity of ~0.1 kg/s/MPa (~0.012 to 0.04 gpm/psi) [40][17]. In November 2012 the well was then re-completed

to the original depth (1771 m), resulting in a longer open-hole section extending from 914 m to 1771 m (referred to here as the "*extended*" stimulation interval).

Hydraulic stimulations were operated through both *shallow* and *extended* intervals, from 920 m to 1070 m (*shallow* interval - September 2010 to November 2012) and from 920 m to 1770 m (*extended* interval - January 2013 to March 2013) respectively [5][17][4].

Stimulation operations in the well 27-15 *shallow* interval unfolded as follows: an initial period of low flow-rate stimulation (Sep 2010) which increased injectivity from ~0.1 to ~1.4 kg/s/MPa (0.012 to 0.15 gpm/psi) was conducted as a series of steps with wellhead (WHP) fluid pressures between 1.7 and 3.8 MPa or below the magnitude of the least horizontal principal stress S_{hmin} (WHP ~5.2 MPa) [16]. Afterwards, a medium flow-rate phase with WHP fluid pressures of 6.9 MPa (or above S_{hmin}) was conducted from April 1 to 10, 2011, and was immediately followed by a high flow-rate phase from April 11 to 23, 2011 characterized by WHP fluid pressures of 6.6 to 6.9 MPa. A final Pulse stimulation with WHP pressures in excess of 9.0 MPa was then carried out on October 28-29, 2011. Further stimulation treatments were attempted in 2011 (i.e. February 2011 chemical stimulation, March 2011 low flow-rate and May-June 2011 high flow-rate), though no significant injectivity gain was recorded [5].

The stimulation treatment for the *extended* interval was conducted applying an initial high flow-rate fluid injection between January 15-20, 2013, with WHP pressures of 4.1 to 5.2 MPa, followed by a long-term, low flow-rate phase from February 17 to March 17, 2013, characterized by WHP pressures of 1.4 to 2.8 MPa [17][4].

The injectivity of the *shallow* open interval improved ~70 fold from a pre-stimulation value of ~0.1 kg/s/MPa (0.012 gpm/psi) to ~7.3 kg/s/MPa (0.8 gpm/psi), while the injectivity of the *extended* open interval improved ~2.6 times, from ~7.3 kg/s/MPa (0.8 gpm/psi) to ~19.2 kg/s/MPa (2.1 gpm/psi) [5][4][17]. The injectivity improvement observed during the *extended*

interval stimulation is only apparently smaller as it actually involves a higher range of permeability. The final injectivity qualifies the well as a commercial injector, which contributes to an extra power plant output of ~1.7MW [17][4].

A great number of micro-earthquakes (MEQs) were recorded during the various stimulation phases [5][17][4] (Figure 1), some of which appear to display a correlation between the hydraulic treatments performed in well 27-15 and the development of deformation in the reservoir, although this correlation was often complicated by concurrent injection operations carried out in injectors 22-22 and 21-2 further south (as introduced and analyzed in [1]).

Poor focal sphere coverage and limited constraints on the seismic velocity model made it difficult to: (1) derive the exact source mechanism for these MEQs, (2) detect events smaller than magnitude $M_w < +0.1$, and (3) define the location of individual events with precision, especially prior to the seismic network upgrade (November 2012). Nevertheless, tensile failure produces relatively high frequency signals at the crack tip – typically of $M<<0$, which are usually only detected with the use of specialized down-hole instruments [37]. Therefore, it is likely that the primary process generating the observed MEQ events at Desert Peak (before November 2012 especially) was hydraulically-induced shear failure (Mode II-III) along pre-existing natural fractures and faults that were well-oriented within the regional stress field for shear failure [7][16].

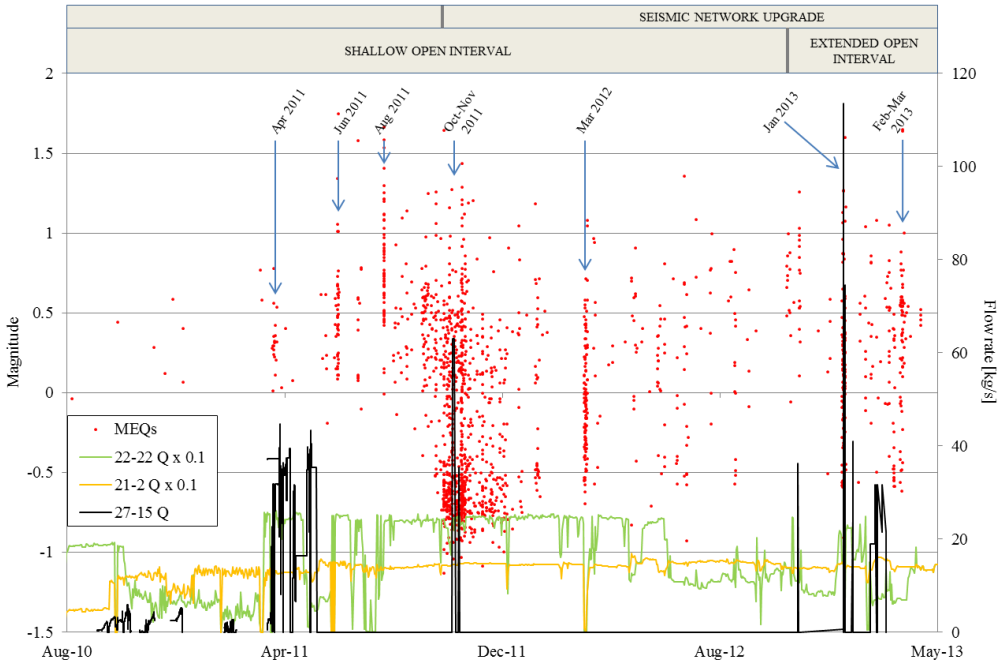

Figure 1 - Microseismicity (MEQs) and injection rate history in Desert Peak wells 27-15 (EGS), 22-22 and 21-2. Flow-rates (Q) in injectors 22-22 and 21-2 are reduced (10 times) for graphical purposes only. Different time windows in the upper part of the graph point to periods of higher density of microseismic activity. This activity appears to be associated with sudden changes in injection flow-rates in either or both wells 22-22 and 27-15 (see [1] for in-depth analysis).

As discussed in detail in a previous study [1], a cause-effect relation between fluid injected in well 27-15 and microseismicity occurrence seems evident during selected *shallow* injection phases (i.e., April 2011, Figure 2) and during the *extended* injection phases (i.e., January 2013, Figure 3). Throughout these phases, the spatial distribution and magnitude of some of the observed microseismicity appear to be consistent with the activation of shear failure (motion) in some areas of a deep fault segment of the main Rhyolite Ridge Fault Zone, in the vicinity of well 27-15 [2][1][12][11]. This fault segment − defined as *Shearing Target Fault* (STF) in [1][2] − is well-oriented for shear failure with respect to the existing stress field and it is supposed to

intersect both injectors 27-15 and 22-22 at ~1400 m depth, representing a potential cross-formational hydraulic connection.

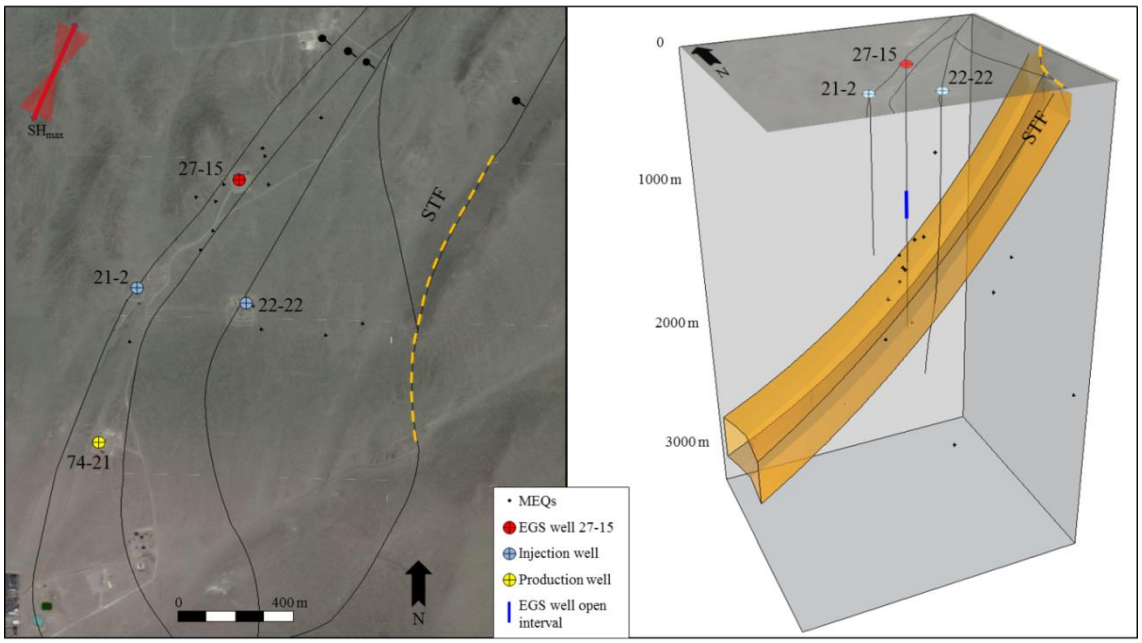

Figure 2 - Induced microseismicity observed between April 2-6, 2011. Over this period, the EGS well 27-15 shallow open interval is being stimulated while injection in well 22-22 is relatively stable. Microseismic events (MEQs) appear mainly located around well 27-15 and at the depth of the STF (Shearing Target Fault) [1], shown in orange. SHmax direction inferred from observation of borehole failures in well 27-15 [7][17]. Black lines show surface trace of interpreted faults; larger black dots shown on downthrown sides of normal faults [12].

Although the STF is ~400 m deeper than the well 27-15 *shallow* interval, numerical simulations carried out as part of a previous study [1] and confirmed here (see below) showed that fluid injection in the *shallow* interval (especially when combined with injection in well 22-22) and the associated pressure diffusion can trigger shear deformation on the deep STF. At any stage in the EGS development, the occurrence of microseismicity and the greatest injectivity gains appear to

be simultaneous. Whether the injection-induced shear deformation on the STF had an implication on the evolution of permeability observed during either/both the *shallow* or/and *extended* phase(s) of the EGS project is to be determined through this investigation.

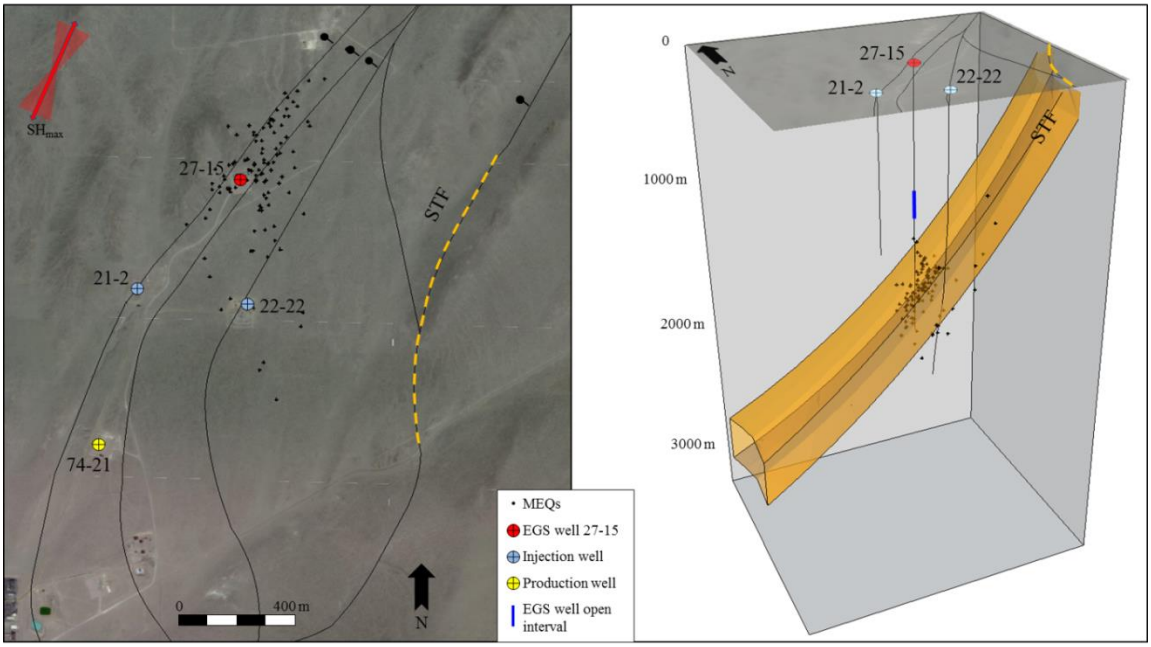

Figure 3 - Induced microseismicity observed between January 15-20, 2013, while the EGS well 27-15 extended open interval was being stimulated. Microseismic events (MEQs) appear mainly located around well 27-15 and at the depth of the STF (Shearing Target Fault) [1], shown in orange. SHmax direction inferred from observation of borehole failures in well 27-15 [7][17]. Black lines show surface trace of interpreted faults; larger black dots shown on downthrown sides of normal faults [12].

Only the stimulation phases carried out between April 2011 and March 2013 (i.e., *shallow* medium/high flow-rate and pulse, and *extended* low/medium flow-rate) are considered and modeled as part of this study (see Table 4), as the relation between injection operations in well 27-15 and the occurrence of microseismicity is evident then. The September 2010 low flow-rate phase − discussed in [9] − is not modeled here.

During this study we will often refer to a conceptual model of the EGS well-site introduced in two companion papers [1][2], which covers all available geological, structural, hydrologic, rock mechanics and seismic data sets, including in situ stresses and fracture network characterization.

2 OBJECTIVES AND APPROACH

The two main probable physical processes responsible for most of the observed permeability gains recorded in well 27-15 between April 2011 and March 2013 were: 1) THM shear-induced dilation, the observed microseismicity (i.e., shear deformation) being concurrent to stimulation operations and to the greatest injectivity/permeability gains, and/or 2) THM tension-induced dilation, cool brines occasionally being injected at pressures equal or higher than the minimum horizontal principal stress (S_{hmin}). It is possible that these processes interplayed/overlapped from time to time, yet distinguishing their relative occurrence is complex and still unclear. However, part of the success of EGS greatly relies on the ability to identify the exact combination of stimulation techniques that can activate either or both of these processes and their subsequent impact on permeability.

So far, chemical precipitation/dissolution is not thought to have had a major influence on the permeability enhancement, given the observed quick reservoir response to stimulation operations (instead chemically-driven permeability modifications occur over months to years [44][42]), and considering that spent brines from the same field were being re-injected.

In order to answer the above premise, the present study puts forth the following main objectives:

a) To understand which set of stimulation choices brings about the conditions that trigger specific physical processes;
b) To recognize which process generates the observable permeability change and provides the best results (highest injectivity/permeability gain/improvement), and to identify its signature at the wellhead;

c) To simulate alternative stimulation scenarios that might yield greater permeability gains;

d) To assess changes in the permeability field (values and distribution) for the main phases of the EGS project.

Despite the challenge it poses, a logical assessment of the characteristics of the injection tests, an appropriate site conceptualization, and the observation of key parameters can be integrated into coupled THMC simulations to help distinguish the complex physical processes generated during the circulation of high-pressure fluids in deep, tight formations. For a given set of injecting conditions (i.e., pressure, flow rate, temperature, duration and well completion) a very specific pressure response can be observed at the wellhead. The shape and value of the wellhead pressure (WHP) curve contain critical information (including pressure fall-off curves) about the formation's permeability, the physical processes that control it and the way they evolve over time. THM fracture dilation processes (tension) behave linearly as they depend on pressure and/or temperature fields diffusing radially from the wellbore toward the reservoir. On the other hand, shear deformation processes are highly non-linear as they reflect the sudden release of energy taking place on inhomogeneous, highly localized and tortuous fault surfaces [28].

With this in mind, a dual-porosity TFReact model (see par. 3) is implemented to simulate the injection-induced physical processes, associated permeability modifications and corresponding pressure response. For the main stimulation phases (April 2011 to March 2013) the model pressure response is continuously calibrated against the monitored site WHP until an optimal match/fit guarantees the correct physical process is replicated, ensuring the permeability change is appropriately represented.

Stimulation operations at Desert Peak were carried out over two distinct intervals (*shallow* and *extended*) with fluid injected at pressures below, equal and above S_{hmin} for varying temperatures and lengths of time. This range of stimulation techniques applied during different phases provides

an excellent opportunity to identify the conditions for the occurrence of each permeability change mechanism.

3 METHODS

In this paper we first explore the features of the numerical simulator TFReact (par. 2) and describe the initial condition and setup of the models utilized; this includes a detailed account of the choices made in order to best assess the reservoir's initial permeability field (par. 4.2). The simulation runs (characteristics, setup and logic) are then illustrated, and the outcomes (interpreted mechanisms, resulting permeability field modifications and alternative simulated scenarios) are discussed (par. 5). Further simulations (pressure falloff, unloading) and considerations on the permeability change mechanisms reversibility are put forth in paragraphs 6.3.1 and 6.3.2, respectively. Alternative injection schemes/scenarios are shown in paragraph 6.4. Comprehensive results and conclusions are finally summarized in paragraphs 7 and 8.

Two TFReact models are built and presented here in order to simulate the stimulation treatments carried out over two distinct well completion schemes, *shallow* and *extended*, respectively. Each of the two models is initially calibrated against the baseline injectivity recorded prior to any stimulation (i.e., pre-EGS). For the purpose of this study, only the stimulation phases which provided observable injectivity gains, and during which a cause-effect relation with the development of microseismicity is observed, are considered. With respect to the *shallow* interval the phases are: 1) April 2011 medium flow-rate; 2) April 2011 high flow-rate, and 3) October 2011 pulse. As concerns the *extended* open interval the phases are: 1) January 2013 high flow-rate, and 2) February/March 2013 long-term low flow-rate. Relatively stable injecting conditions (constant flow-rates) make these phases good candidates for the numerical simulations presented here.

Beginning with the April 2011 medium flow-rate, each phase is simulated and any resulting permeability modification reassigned as initial condition for the following phase. Some of the permeability acquired from one phase to another − particularly during prolonged injection shutoff periods − may be partially lost, as the permeability change mechanisms are/may be to some extent reversible. Nonetheless, as addressed in paragraph 6.3.2, the time in between major phases at Desert Peak is short enough that the permeability loss is negligible.

3.1 TFReact functions and logic

TFReact v2.0 − introduced by *Taron et al., 2009* [43][45] − is a modular THMC simulator that works by coupling the thermal, hydraulic, and chemical (THC) capabilities of TOUGHREACT [50] with the mechanical (M) calculations of Itasca's FLAC3D [18]. The coupling of fluid and mechanical system is undrained (i.e. fluid diffusion relative to mechanical equilibrium is slow enough that fluid pressure dissipation may be ignored over a single mechanical equilibration) [43]. TFReact models the evolution of the permeability field through a continuum approach, and evaluates relationships between plastic failure processes, shear dilation, thermo-mechanical compression, and chemical-mechanical processes, simulating fracture dilation and shear through plastic strain. The energy balance equation is carried out in TOUGHREACT [43]. A separate code (interpolation module) converts data output from either TOUGHREACT or FLAC3D as input to the other, and performs permeability evolution, dual-porosity poroelastic response to stress and fluid compressibility calculations. TOUGHREACT central node data are interpolated to corner node input to FLAC3D (Figure 4) [43].

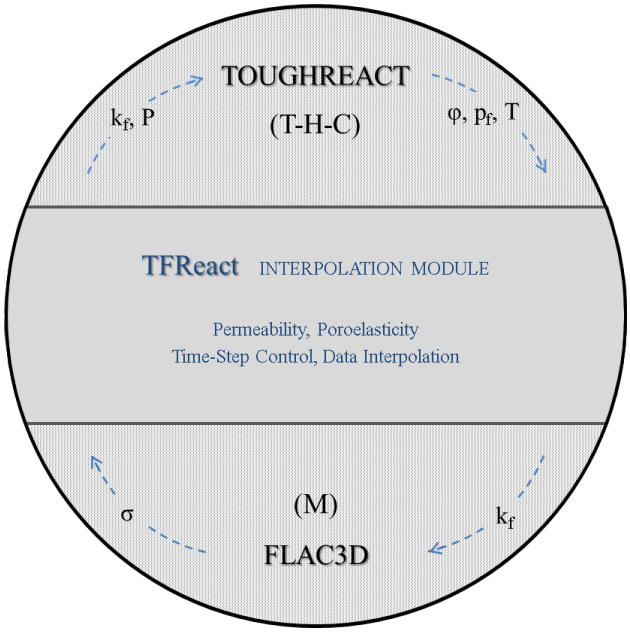

Figure 4 - TFReact simulation and coupling logic between TOUGHREACT, FLAC3D and the interpolation module (modified from [43]). The interpolation module converts data output from either TOUGHREACT or FLAC3D as input to the other, and performs permeability evolution, dual-porosity poroelastic responses to stress and fluid compressibility calculations [43].

The reactive component (C) of the simulator is not utilized here, as chemical dissolution/precipitation mechanisms are not believed to have influenced the permeability field over the short time that characterized the stimulation operations at Desert Peak. It may, however, be switched on at any time in order to evaluate the reservoir response to tracer testings and to long-term production/injection operations. By appropriately sub-gridding the matrix, blocks of low permeability are embedded in a network of interconnected fractures (treated as continua), following the double porosity concept developed by [48]. Pressure, temperature and composition changes propagate rapidly through the fracture system (continuum 1) but slowly the matrix blocks (continuum 2) [30].

3.2 Composite failure criterion and flow rule

The continuum mechanics calculations of TFReact are carried out in FLAC3D through the use of constitutive equations that define the medium for a given set of properties, boundary and initial conditions. Although several constitutive models are available in FLAC, only the Mohr-Coulomb plastic model group - used in this study - is briefly described here. The Mohr-Coulomb is the typical model used for simulating shear failure in soils and rocks. Strain hardening/softening tables are integrated in TFReact to appropriately represent the medium's non-linear behavior, for which the prescribed Mohr-Coulomb properties vary as a function of the deviatoric plastic strain. The position of a stress point on the failure envelope for this model is controlled by a flow rule for both shear and tension failure [18]. In a graphical representation of the FLAC/Mohr-Coulomb failure criterion (Figure 5), the failure envelope is $f_s = 0$ from A to B and $f_t = 0$ from B to C, with $f_s = \sigma_1 - \sigma_3 N_\varphi + 2c\sqrt{N_\varphi}$ and with $f_t = \sigma_3 - \sigma^t$, where φ is the friction angle, *c* is the cohesion, σ^t is tensile strength, and $N_\varphi = \frac{1+\sin(\varphi)}{1-\sin(\varphi)}$ [18]. Two potential functions, g^s and g^t, determine the occurrence of shear or tension failure with $g^t = \sigma_1 - \sigma_3 N_\psi$, where ψ is the dilation angle and $N_\psi = \frac{1+\sin(\psi)}{1-\sin(\psi)}$ [18]. The function $h = \sigma_3 - \sigma^t + a^P(\sigma_1 - \sigma^P)$ identifies two domains, positive and negative, respectively. The constants are $a^P = \sqrt{1 + N_\varphi^2} + N_\varphi$ and $\sigma^P = \sigma^t N_\varphi - 2c\sqrt{N_\varphi}$. If the stress point in the σ_1-σ_3 plane falls within the negative domain, conditions for shear failure are established, and the position of the stress point on the $f_s = 0$ curve is given by the potential function g^s. On the contrary, if the stress field falls within the positive domain, conditions for tension failure exist and the position of the stress point on the $f_t = 0$ curve is given by the potential function g^t [18].

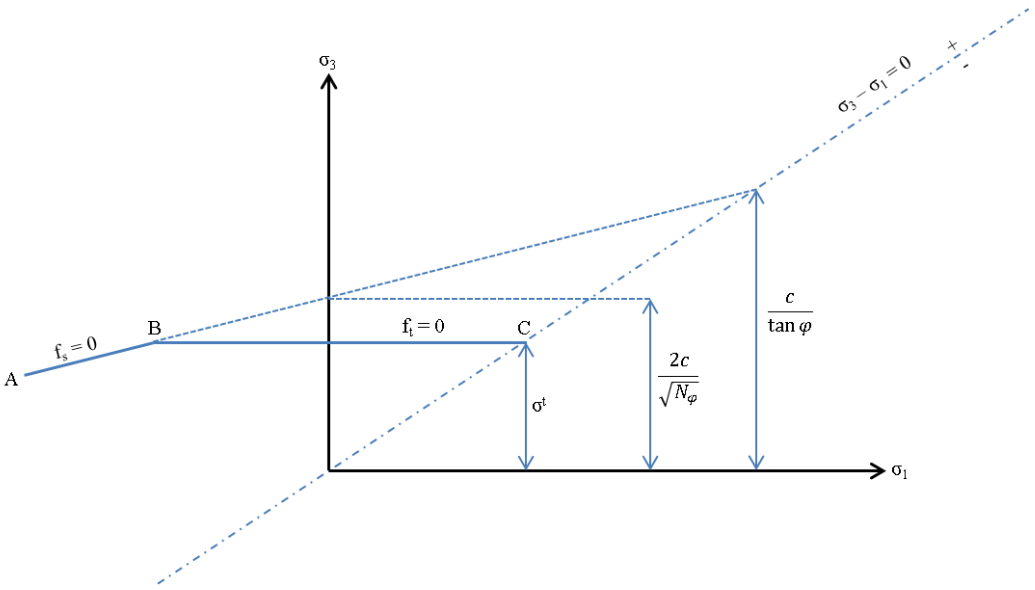

Figure 5 - FLAC3D Mohr-Coulomb failure criterion diagram (modified from [18]). f_s and f_t represent the envelopes for shear and tensile failure, respectively. Thorough explanation available in the text.

3.3 Permeability change calculations

T-H-M permeability changes in TFReact are calculated by taking into account the combined action of thermo-hydro-mechanical dilation/contraction and shear dilation mechanisms, all of which strongly depend on temperature and effective stress changes. Chemical (C) mechanisms for permeability change (available in TFReact) are not implemented in this study for the reasons explained earlier. All simulations are run on a composite fracture/matrix system where permeability changes associated with both shear and tensile failure are governed by dynamic changes in fracture apertures. Fracture permeability is generally calculated as a function of fracture aperture (b) and spacing (s) from the cubic law $k = \frac{b^3}{12s}$ [38][49]. To evaluate fracture aperture changes (i.e., permeability changes), a few constitutive relationship choices − based on laboratory results of fracture behavior under hydrothermal conditions [43][26] − are available in TFReact.

Specifically, an empirical non-linear fracture stiffness relation is adopted here to calculate changes in the hydraulic aperture of a fracture under an applied effective stress (i.e., mechanical dilation/contraction) [43]:

$$b = br + (b_{max} - b_r)\exp(-\alpha(\sigma' - \sigma'_0))$$

where,

σ' = Effective stress

σ'_0 = Effective stress at which zero deformation occurs

α = Non-linear fracture stiffness [1/MPa]

b_r = Residual fracture aperture [m]

b_{max} = Maximum (at σ'_0) fracture aperture [m]

When temperature gradients between injected fluid and host rock evolve, thermal effects on the final hydraulic aperture take place through the development of thermal strain. Because the injected fluid pressure is in fact an applied stress, this approach effectively describes thermo-hydro-mechanical (tension-induced) permeability changes.

Permeability modifications related to shear mechanisms are computed in the model by altering the fracture aperture as a function of plastic strain (which obeys the FLAC3D flow rule) and dilation angle [43][41] as follows:

$$db_i = du_i \, tan(\alpha)$$

Where subscript *i* stands for the three coordinate directions and,

u = plastic deformation/displacement

b = fracture aperture

α = dilation angle

The role of the dilation angle is to update stresses in the plastic flow rule and control the rate of permeability change through aperture dilation [43] and it may reflect the fracture surface roughness (Figure 6) [31]. Both permeability change models (tension and shear dilation) may, independently of each other, be switched on and off anytime depending on what is to be analyzed.

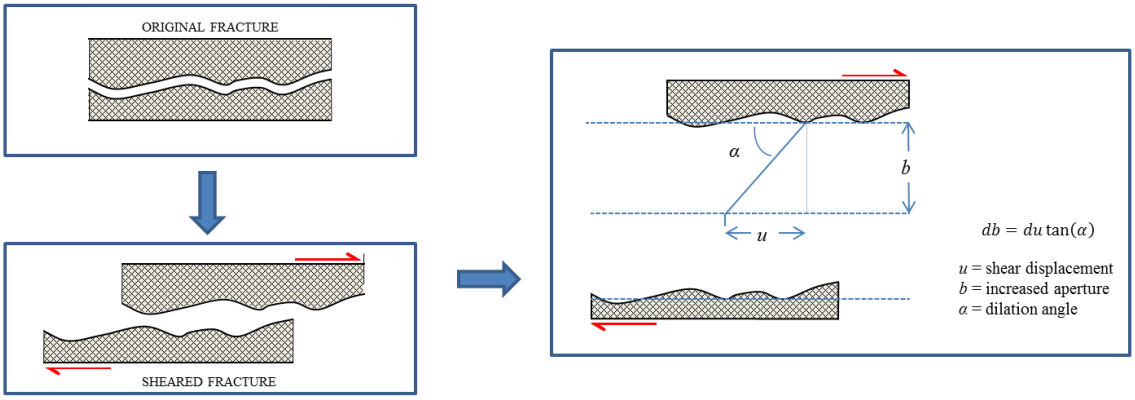

Figure 6 - Shear displacement and dilation angle-derived fracture aperture as used in TFReact to evaluate permeability changes resulting from plastic (shear) deformation.

4 MODEL CONFIGURATION

4.1 Mesh construction, initial and boundary conditions

The simulated domain size is x = 800 m, y = 900 m and z = 1430 m, large enough to encompass the reservoir volumes and wells that potentially interact with, and are affected by, stimulation operations in EGS well 27-15. A triple-well radial mesh (becoming regular with distance from the wells) is generated to account for the effects of fluid being injected simultaneously in EGS well 27-15 and nearby injectors 21-2 and 22-22. A simple geometry option − yet consistent with orientation (NNE) and thickness − is used to reproduce the STF. The grid is aligned with the Rhyolite Ridge Fault Zone (i.e., the STF), hence rotated ~20º clockwise from the north. The mesh discretization is finer near the wells (injection points) and coarsens with distance, and it is finer

for the volumes surrounding well 27-15 (compared to wells 21-2 and 22-22) as this well is the subject of the analysis (Figure 7). This radial symmetry model allows for an analysis of formation behaviors both near and far from the wellbore.

The injectors are simulated through the definition of "dummy" (or boundary) elements, which − though not part of the primary mesh − are used in TFReact to assign Dirichlet boundary conditions (in this case, a constant source of mass flow-rate). These dummy elements have a volume comparable to the mesh elements representing the open-hole sections of the wells, and are connected to all elements in the inner radius. The injection dummy element for well 27-15 is applied over a length of 150 m when simulating the *shallow* open interval phases, and over 850 m when simulating the *extended* open interval phases. It is always applied over a length of 780 m and 350 m to simulate the open interval of wells 22-22 and 21-2, respectively (Figure 8).

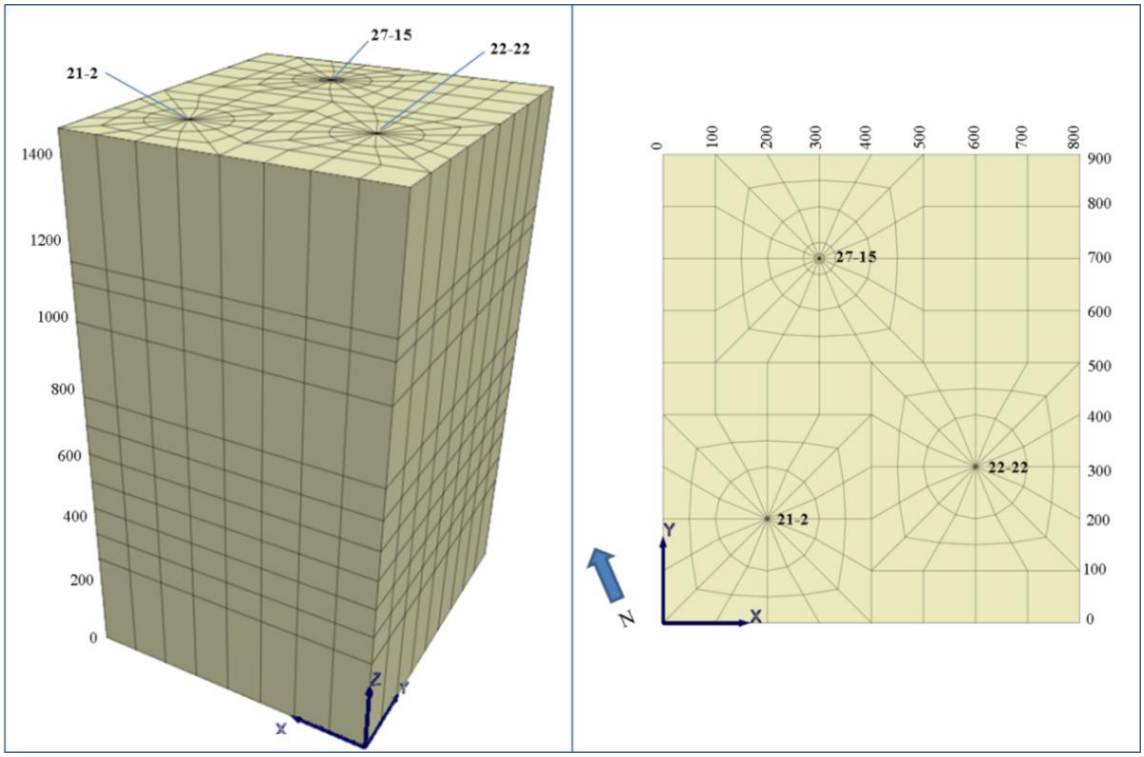

Figure 7 - TFReact triple-well mesh construction diagram. Initial and boundary conditions are described in the text. The mesh is aligned with the orientation of known structural features (i.e., STF) and approximate stress field. Top and bottom of the model at approximately 620 m and 2050 m below surface.

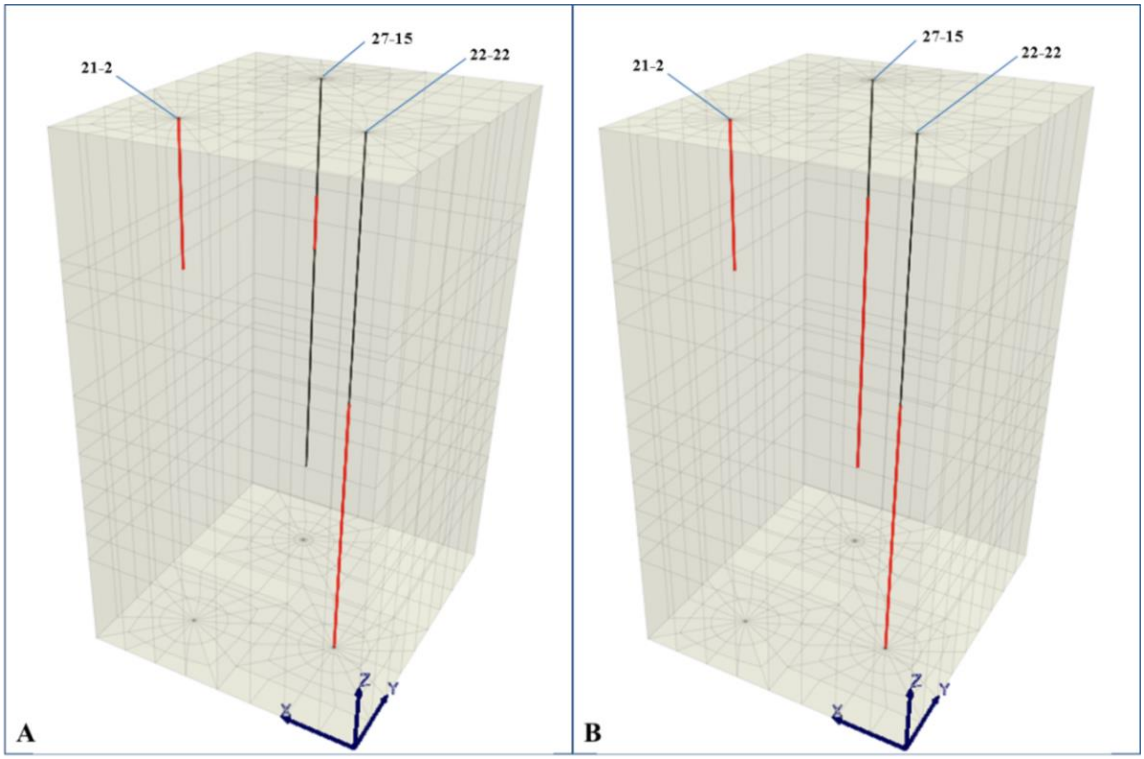

Figure 8 - Completion schemes adopted in TFReact for the simulation of hydraulic treatments performed in: (A) the *shallow* (920-1070 m below surface), and (B) *extended* (920-1770 m below surface) open intervals of EGS well 27-15. Open-hole sections in red. Top of the model at approximately 620 m below surface. Well 21-2 open-hole section extends from 620 m to 970 m below surface. Well 22-22 open-hole section extends from 1270 m to 2050 m below surface.

Figure 9 illustrates the STF location with respect to the open interval of well 27-15. The model elements corresponding to the injection dummies are set with a very high fixed permeability. This way, the permeability modifications in the model are governed by all the other elements and are not influenced by the conditions of the volumes relative to the injection dummies. The pressure of the injection elements is output to monitor the reservoir response to fluid injection (i.e. down-hole pressure or DHP). The high permeability of the injection elements ensures that the output pressure within any of the injection elements is uniform (i.e, even when the open-hole interval intersects different layers with multiple permeability values).

The initial reservoir temperature is set to 200°C. According to the relations $S_{Hmax} = (S_{hmin} + S_v)/2$ and $S_{hmin} \approx 0.61 \cdot S_v$, and using a vertical overburden gradient of ~20 kPa/m and a pore pressure gradient of ~8.5 kPa/m [16], stress and pressure in the model are initialized using the depth of the central point of the relative simulated injection interval (Table 1, Figure 15).

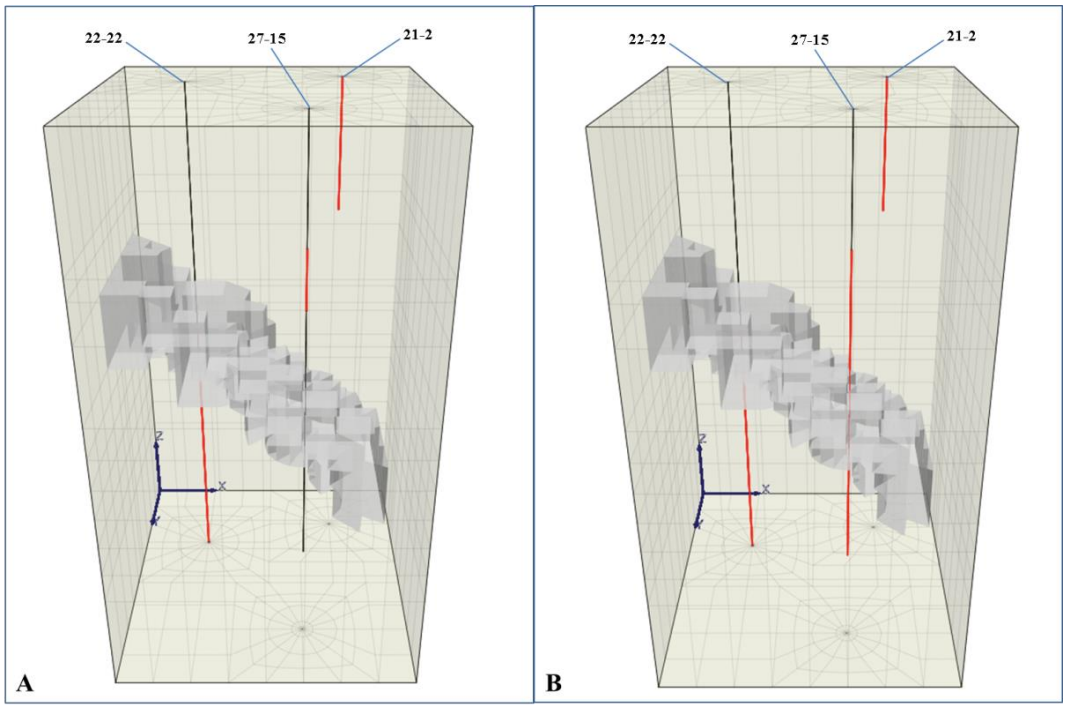

Figure 9 - Shearing Target Fault (STF) location in TFReact with respect to different EGS well 27-15 completion schemes: the STF is ~400 deeper than the *shallow* open-hole section (A), while it is fully intersected by the *extended* open interval (B).

Table 1 - Reference depths and corresponding ambient formation fluid pressure and stress employed for the TFReact simulation of the *shallow* and *extended* hydraulic treatments.

REF. OPEN INTERVAL	open		simulated depth [m]	Fuid Pressure [MPa]	σ_{xx} (S_{hmin}) [MPa]	σ_{yy} (S_{hmax}) [MPa]	σ_{zz} (S_v) [MPa]
	from [m]	to [m]					
shallow	920	1070	995	8	15.0	19.8	24.6
extended	920	1770	1345	11	20.3	26.8	33.3

Outermost boundaries are specified by fixing pressure (free draining conditions on the edges) and temperature through four large-volume planar dummy elements connected to the lateral sides of the model.

The model is set to plastic and it is run with a partially undrained methodology, i.e. FLAC3D uses zone-wise Biot constant and Biot modulus to find undrained equilibrium with fluid [43]. All simulations are non-isothermal, thus thermal strains resulting from temperature gradients between the injectate and the host rock are evaluated in the mechanical equilibrium. The material properties used in the model are derived from the Desert Peak rock mechanical testing and petrologic analysis [23], and Mohr-Coulomb parameters correspond to the average residual mechanical values for the formations involved. The Biot coefficient is set to 0.8 and the bulk modulus to 8.0 GPa. The dilation angle is set to 20° and the fracture stiffness to 1.36e-1. The STF elements have a friction angle of 29°, and 0 cohesion, as in-situ stress measurements in a variety of tectonically-active geological settings suggest that fracture planes well-oriented with respect to the stress field are generally cohesionless [15][47] (Table 2). All of these values are within the ranges also adopted in similar modeling studies of fractured rock masses/fault zones [13][25][34][2][35][32][46], and are here mainly determined by fitting the modeled reservoir response (i.e., volumes displaying conditions for shear failure and WHP) with field observations (i.e., approximate locations of microseismic events and monitored WHP).

Dual permeability is set with a classic double porosity methodology, thus flow only occurs in the fractures with communication to the matrix domain [43]. As introduced in Paragraph 3.3, fracture permeability is calculated as a function of fracture aperture (b) and spacing (s) from the cubic law $k = \frac{b^3}{12s}$. Fracture apertures are set with ranges that allow to reproduce the desired permeability in the model (see par. 4.2 and Table 3). The spacing of fractures that are likely to

contribute to fluid flow is set to 3.0 m, following the analysis of well 27-15 FMS and ABI85 image logs [7] described in [2].

Table 2 - Solid medium properties and parameters as used in both *shallow* and *extended* TFReact models.

PARAMETER	UNIT	Background	STF
Residual friction angle	°	42	29
Residual linear cohesion	MPa	7	0
Tensile strength	Pa	1e10	1e10
Dilation angle	°	20	20
Thermal expansion	$°K^{-1}$	1.5e-5	1.5e-5
Solid density	kg/m^3	2500	2500
Bulk Modulus	GPa	8.0	8.0
Poisson Ratio	-	0.22	0.22
Biot Coeff.	-	0.8	0.8

Fracture aperture and spacing are uniformly initialized in the three Cartesian directions x, y, z. Nevertheless, the model's initial response to the applied differential (tectonic) stresses produces anisotropic permeability distributions consistent with the permeability tensors calculated for the EGS well 27-15 formation [2], where flow occurs preferentially through k_z and k_y (NS), relative to k_x (EW) (i.e., k_z and $k_y > k_x$), in agreement with the trend of the major structural features at Desert Peak.

4.2 Assessment of baseline permeability

Appropriately representing the permeability (*k*) of the modeled reservoir is essential in order to correctly simulate the processes with which we are concerned. As a general rule, the simplest possible geometry option − yet consistent with key observations − is used to define the permeability field.

With respect to the permeability field, the general approach here is to define four principal domains representing: (1) high-*k* reservoir volumes pertaining to wells 22-22 and 21-2 (k_{af}, active field), (2) low-*k* reservoir volumes concerning the formation surrounding well 27-15 (k_{tf}, tight formation), (3) high-*k* layers for the STF [2] (k_{STF}), and (4) volumes with *k* enhanced as part of the treatments carried out prior to April 3, 2011 (i.e., September 2010 low flow-rate phase, and April 1-2, 2011 two-step rate injection test) (k_{lfr}), with $k_{af} > k_{STF} > k_{lfr} > k_{tf}$ (see Table 3 and Figure 10 for a summary and visual diagram). Throughout the simulation of all the EGS phases, k_{tf}, k_{lfr} and k_{STF} evolve, while k_{af} remains constant (i.e., only the domains pertaining to well 27-15 will be affected by the hydraulic stimulation treatment) (see par. 5).

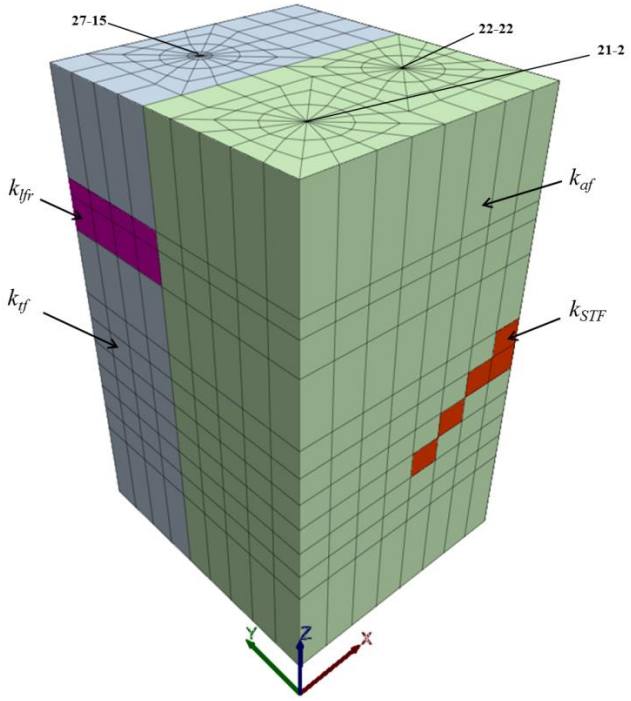

Figure 10 - TFReact baseline permeability diagram: k_{af} (active field) represents highly permeable volumes pertaining to wells 22-22 and 21-2; k_{tf} (tight formation) is the low permeability that characterizes the formation surrounding well 27-15; k_{STF} represents the STF high permeability; k_{lfr} (low flow-rate) are enhanced-permeability volumes resulting from any hydraulic treatment carried out prior to the April 2011 stimulation phases.

k_{af} is evaluated by simulating the pressure response (overpressure) resulting from operational fluid injections in wells 21-2 and 22-22, and by adjusting it to a value of 5.6e-13 m^2 which provides the best match with the site WHP.

k_{tf} is initialized on the basis of the pre-EGS injection test carried out along the *shallow* open section of well 27-15, which revealed an injectivity of about 0.1 kg/s/MPa (0.012 gpm/psi) [17], corresponding to a permeability of about 1.20e-16 m^2. Probabilistic discrete fracture network assessment (DFN) of the sampled fracture population derived from FMS and ABI85 image logs in well 27-15 over the same *shallow* interval also confirmed this permeability value [1].

k_{STF} is estimated by simulating the pressure response of the 2009 pre-EGS injection test carried out along the *extended* open interval of well 27-15. This test shows an injectivity of ~1.8 kg/s/MPa (0.2 gmp/psi), corresponding to a permeability of about 5.17e-15 m^2. The higher permeability displayed by this test for the *extended* interval is assumed to be the result of higher hydraulic conductivity in the STF intersected by this open interval. Using k_{tf} and k_{ar} as evaluated above, k_{STF} is therefore adjusted to a value of 5.2e-15 m^2, which ensures the best fit with the 1.8 kg/s/MPa baseline injectivity value (Table 3).

Finally, k_{lfr} is evaluated by increasing k_{tf} for the layers pertaining to the *shallow* open interval of well 27-15 until a good match with the pressure response observed at the start of the April 2011 medium flow-rate phase is reached. This requires k_{lfr} to be equal to 1.1e-14 m^2.

Clearly, the spatial assignment of hydraulic properties is non-unique, due to the complex, real-world geologic setting. Yet, constraints on the spatio-temporal evolution of a 2009 pressure transient testing [10] modeled in a companion paper by using a similar permeability assessment [1] support the field permeability adopted here.

Table 3 - TFReact initial permeability zones and corresponding fracture parameterization (see Figure 10 for diagram).

Permeability zones	k [m^2]	k_x [m^2]	k_y [m^2]	k_z [m^2]	b_{min} [m]	b_{max} [m]	Fracture Spacing [m]	Fracture Stiffness
k_{af}	5.6e-13	5.6e-13	5.6e-13	5.6e-13	2.73e-4	2.73e-4	3.0	1.36e-1
k_{tf}	1.2e-16	2.6e-17	1.6e-16	1.8e-16	1.00e-7	5.80e-5	3.0	1.36e-1
k_{STF}	5.2e-15	5.2e-15	5.2e-15	5.2e-15	5.71e-5	5.71e-5	3.0	1.36e-1
k_{lfr}	1.1e-14	9.8e-15	1.1e-14	1.2e-14	6.52e-5	1.00e-4	3.0	1.36e-1

5 SIMULATION RUNS

Injection-induced deformation mechanisms, stress/strain and permeability modifications are all explored here through sequential simulations of the main EGS stimulation phases. The simulated phases are: for the *shallow* interval 1) April 2011 medium flow-rate, 2) April 2011 high flow-rate, and 3) October 2011 pulse; while for the *extended* interval, 1) January 2013 high flow-rate and 2) February/March 2013 long-term low flow-rate (Table 4). Overall, we only simulate the sections where observable permeability changes are recorded, as the goal of this study is to capture and model the mechanisms for permeability change under different injection conditions. With the exception of minor differences (see below), all simulations are initialized following the conditions and set-up logic introduced in paragraphs 4.1 and 4.2.

Table 4 - Modeled injection phases and characteristic time-window, flow-rate, temperature, pressure and resulting injectivity. Temperature of injected fluid during extended interval stimulation is approximate (P.Spielman, Ormat, personal communication, July 3, 2014).

	Phase modeled	From	to	Q [kg/s]	T [°C]	WHP [MPa]	DHP [MPa]	Final Injectivity [kg/s/MPa]
shallow	Medium Q	04/05/11	04/10/11	31	50	6.8	15.0	4.6
	High Q	04/15/11	04/23/11	36	54	6.5	14.5	5.5
	Pulse	10/28/11	10/29/11	63	60	8.2	17.5	7.3
extended	High Q	01/19/13	01/20/13	100	55	4.6	15.6	22.0
	Long-term low Q	02/22/13	03/04/13	31	55	1.4	12.3	22.0

6.1 *Shallow* open interval

The *shallow* open interval of well 27-15 is used for the initial series of hydraulic stimulation from September 2010 up to November 2012. It extends from ~920 m to ~1070 m in depth. When modeling the injection phases relative to this *shallow* interval, a temperature of 200º C and pressure of 8 MPa (corresponding to a hydraulic head of ~995 m, evaluated for the mid-point of this open-hole section) are set as initial conditions. The stresses applied to the model are also calculated using a depth of 995 m (mid-point of the *shallow* open interval), with σ_{xx} = 15 MPa, σ_{yy} = 19.8 MPa, and σ_{zz} = 24.6 MPa (see Table 1).

6.1.1 April 2011 medium flow-rate phase

The medium flow-rate phase (controlled hydraulic fracturing) is performed in the *shallow* section of well 27-15 from April 1 to April 10, 2011, with fluid flow rates of ~31 kg/s and well-head pressures of ~6.9 MPa, exceeding the minimum principal horizontal stress for the formation at the depth of the *shallow* open interval ($S_{hmin} \approx$ 5.2 MPa WHP or ≈ 13.9 MPa DHP). Approximately

between April 5 and April 10, 2011, the main permeability enhancement is evident from a decreasing wellhead pressure under a constant 31 kg/s injection rate (permeability gain → reduction in resistance to flow → pressure decline). During this time fluid injection is continuous as no pump interruptions occur while the injectivity grows from ~3.8 kg/s/MPa to ~4.6 kg/s/MPa (0.4 gpm/psi to 0.5 gpm/psi). This time window (April 5-10) is modeled here with the aim to investigate the processes that caused the monitored injectivity (permeability) enhancement.

A cause-effect relation between the fluid injected into the *shallow* interval during this phase and the development of microseismicity on the STF is evident from both simulations carried out in FLAC3D [2] and TFReact (this study), especially when the hydraulic stimulation in 27-15 is concurrent with injection operations in well 22-22. Pore pressure diffusion resulting from injection operations impacts STF stability − its orientation and stress state are already in critical condition for shear failure − triggering some shear deformation. Although the observed microseismicity (suggesting shear motion at the depth of the STF) is concurrent with the measured WHP decline, it is unclear whether this shear motion was the actual cause of the observed permeability gain, given that the STF is ~400 m deeper than the *shallow* open interval. To answer this question we first run a long series of simulation exercises of the medium flow-rate phase by turning off every permeability change mechanism but the shear dilation in the model. During this process, several mesh configurations and sets of parameters are employed within realistic margins, in order to simulate if an alteration in the WHP response is observable when shear motion occurs along the STF. This analysis suggests that the observed shear failure of the STF resulting from *shallow* interval stimulation operations does not result in an observable wellhead injectivity gain. The slight permeability improvement observed at the depth of the STF during this phase is too far and disconnected from the *shallow* open interval of the well to cause the measured pressure decline. Shear failure in volumes surrounding the open interval of the well does not occur / is not declared in FLAC3D for the given mechanical parameters. Some shear

may develop on smaller sets of fractures (see par. 8) but it is not considered to be a major process in the observed development of permeability here. The non-occurrence of major shear failure is in accordance with: (1) the FLAC3D flow rule (for the mechanical and hydraulic conditions of the elements nearby the open interval) (Figure 11), and (2) the non-occurrence of microseismicity in this area.

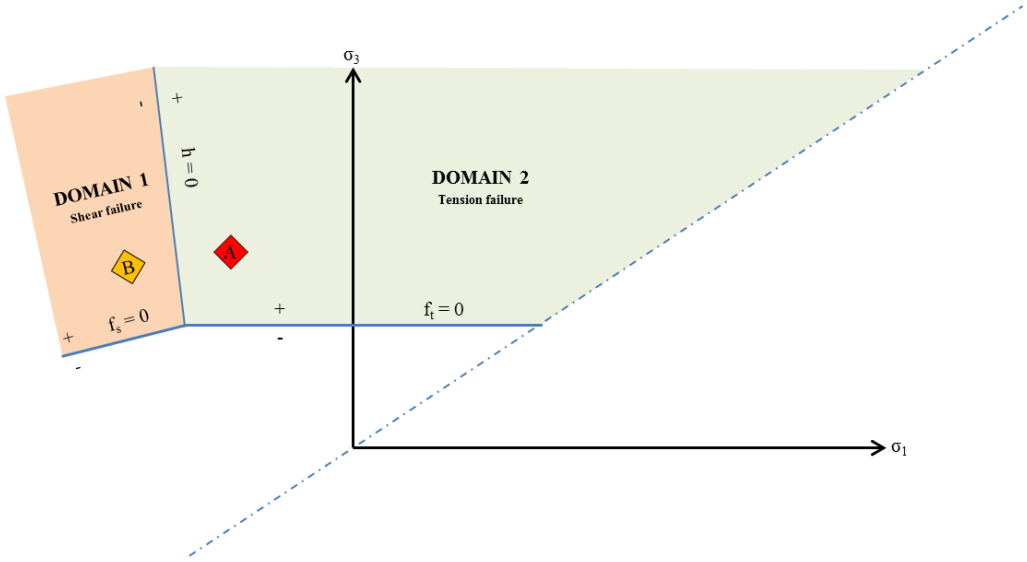

Figure 11 - FLAC3D flow rule and failure conditions for simulated volumes surrounding well 27-15 open intervals during: (A) the Apr 2011 *shallow* medium flow-rate → the stress point falls within the positive domain 2 indicating mainly conditions for tension failure; and (B) the Jan 2013 *extended* high flow-rate stimulation phase (monitored on STF, see below par. 6.2) → the stress point falls within the positive domain 1 indicating predominantly conditions for shear failure. These conditions, calculated analytically, are confirmed by the numerical results.

After this initial analysis, the mechanical dilation/contraction permeability model (tension-induced) is switched on in TFReact, and the non-linear fracture stiffness relation is selected (see par. 3.3) to describe permeability changes due to stress-induced fracture aperture modifications. Although a long series of trial simulations are run in order to find the appropriate combination of

fracture parameters, the thermo-hydro-mechanical dilation/contraction (tension) permeability change model appears to correctly reproduce the slow and constant site WHP drop shown during this phase. Several mesh configurations are also implemented as part of these simulation exercises, though only the one described in paragraph 108 offers more stable and discretization-independent results. Therefore, the permeability changes observed for this phase appear to be mainly caused by a combination of: 1) hydro-mechanical fracture dilation (due to injected fluid pressures in excess of S_{hmin}), and 2) thermo-mechanical fracture dilation (due to the development of thermal strain induced by the gradient between injected fluid (~50º C) and reservoir (~200º C)). Figure 26 shows the modeled relation between injection-induced temperature front and the development of volumetric strains for this phase. Though several tests on fracture parameterization sensitivity are conducted, only the set listed in Table 3 provides the modeled pressure curve for the applied boundary conditions. The satisfactory match between the resulting modeled and measured pressure responses (Figure 12) is a good indication that the permeability mechanisms are correctly captured and the model parameters appropriately defined.

Table 5 shows the simulated permeability modifications as a result of this hydraulic treatment for radially-distributed selected elements around the open-hole section. Permeability modifications resulting from this phase are re-assigned as initial conditions for the simulation of the next high flow-rate phase. Figure 13 shows the development of temperature, pressure, volumetric strain and permeability during the simulated medium flow-rate phase.

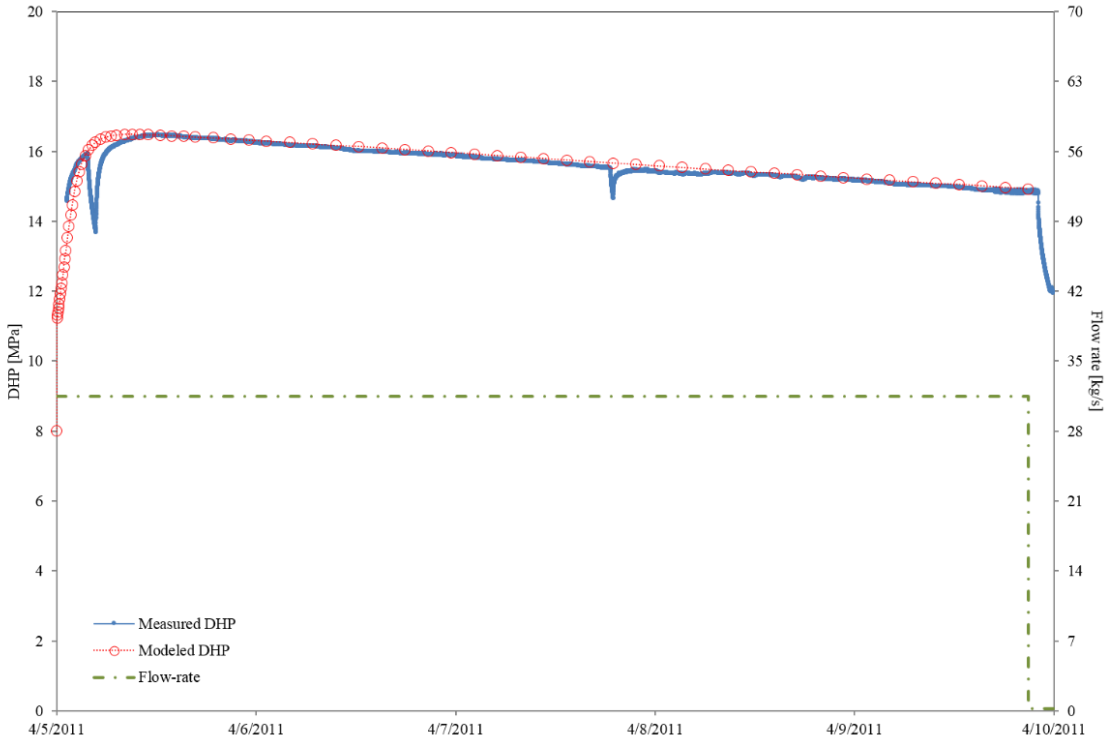

Figure 12 - Measured and TFReact-modeled down-hole pressure (DHP) evolution during the April 2011 medium flow-rate phase, evaluated for the mid-point of the *shallow* EGS well 27-15 open interval (corresponding to ~995 m depth). A constant 31 kg/s flow-rate is injected in EGS well 27-15 to simulate this phase.

Table 5 - Well 27-15 *shallow* open interval stimulation phases (~995 m depth) and corresponding TFReact-modeled injectivity gains as a function of wellbore distance.

Radial distance from wellbore [m]	Medium Q (Apr 2011)		High Q (Apr 2011)	Pulse (Oct 2011)
	Initial k [m^2]	Final k [m^2]	Final k [m^2]	Final k [m^2]
0 (wellbore)	2.3e-10	2.3e-10	2.3e-10	2.3e-10
1	1.1e-14	1.9e-14	2.0e-14	2.2e-14
2	1.1e-14	1.8e-14	1.9e-14	2.2e-14
6	1.1e-14	1.5e-14	1.6e-14	2.0e-14
20	1.1e-14	1.2e-14	1.3e-14	1.4e-14
66	1.1e-14	1.1e-14	1.1e-14	1.1e-14

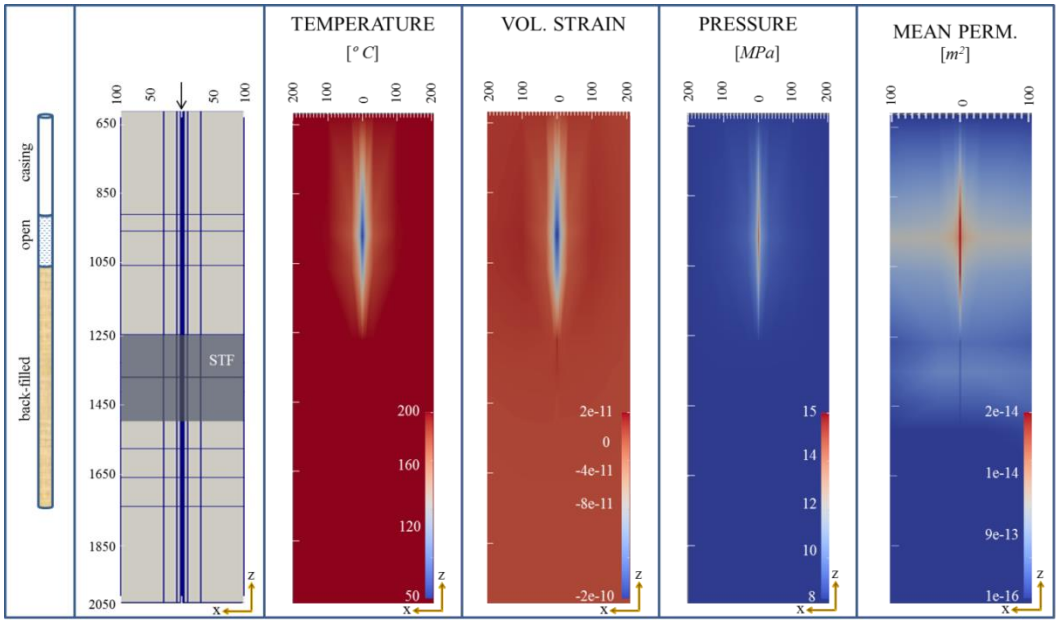

Figure 13 - TFReact output Temperature, Volumetric Strain, Pressure and average Permeability fields at the end of the April 2011 *shallow* medium flow-rate phase simulation. x-z (EW) model slice, depth and horizontal distance from wellbore in meters. Cooler temperatures and thermally-induced volumetric strains only diffuse up to ~10 meters around the wellbore. Fluid pressure drops below S_{hmin} at a small distance from the injection (see Figure 25). As a result, the THM-induced fracture dilation (tension) and associated permeability gain are limited to volumes near the wellbore.

6.1.2 April 2011 high flow-rate phase

The high flow-rate phase (controlled hydraulic fracturing) is performed in the *shallow* section of well 27-15 from April 10 to April 23, 2011, with fluid flow rates of 33 to 41 kg/s and well-head pressures of 6.6 to 6.9 MPa, exceeding the minimum principal horizontal stress S_{hmin}. Here too, the main permeability enhancement is revealed by a slowly-decreasing wellhead pressure when fluid injection is maintained over a few days. For this phase, the main permeability enhancement happens between around April 10 and April 23, 2011. In a similar way to the preceding phase, constant and prolonged fluid injection characterized by no pump interruptions appears to be needed in order to trigger noticeable permeability enhancements which are shown in a ~4.9

kg/s/MPa to 5.4 kg/s/MPa (0.5 gpm/psi to ~0.6 gpm/psi) improvement in injectivity. The April 15-23 time window is modeled here with the aim of detecting the permeability change mechanisms. Also for this phase, by selecting the non-linear fracture stiffness model, TFReact can reenact the site WHP drop. Here too, permeability is enhanced as a result of combined thermo-mechanical and hydro-mechanical dilation (tension). For this phase the temperature of the injected fluid is ~54º C. For simplicity, a constant 36.5 kg/s flow rate (4-step field flow-rate weighted average) is used to model this phase. Figure 14 shows the modeled pressure response and a good fit with the site WHP.

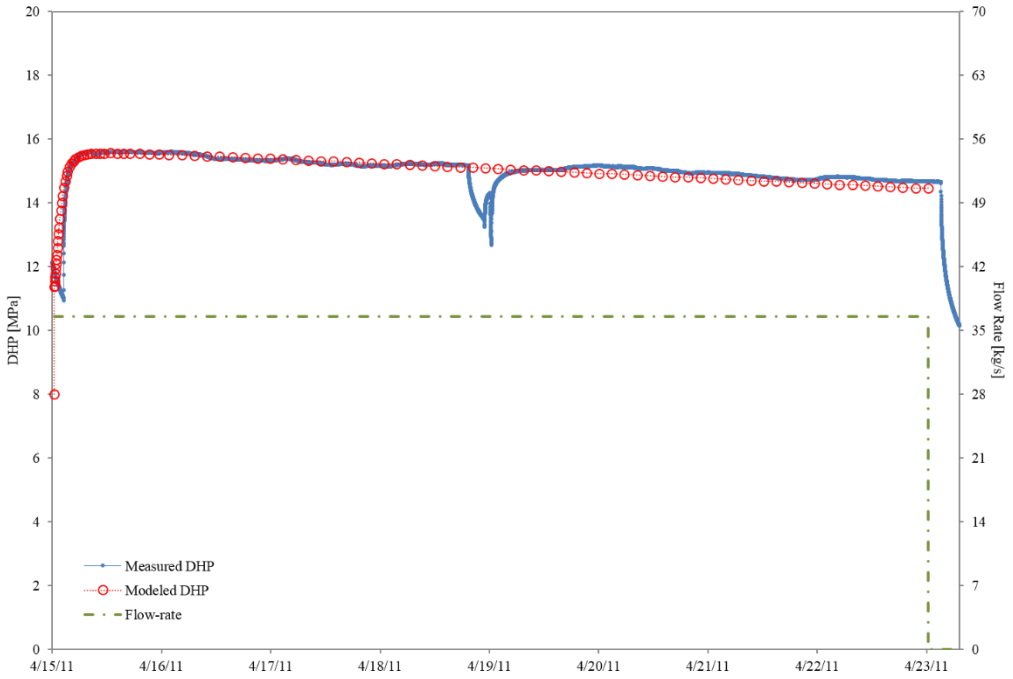

Figure 14 - Measured and TFReact-modeled down-hole pressure (DHP) evolution during the April 2011 high flow-rate phase, evaluated for the mid-point of the *shallow* EGS well 27-15 open interval (corresponding to ~995 m depth). A constant 36 kg/s flow-rate is injected in EGS well 27-15 to simulate this phase.

6.1.3 October 2011 pulse phase

The pulse phase takes place in the *shallow* section of well 27-15 between October 28 and 29, 2011, with a fluid flow-rate of 63 kg/s and well-head pressures of 9 MPa, once again far exceeding S_{hmin}. Here the injectivity grows to ~7.3 kg/s/MPa (0.8 gpm/psi). The enhanced permeability from the end of the preceding high flow-rate simulation run is used as initial condition to model this pulse phase. One could argue that some of the permeability enhanced as part of the previous phase might have been lost between April and October. However, unloading simulations (see par. 133) suggest that the enhanced permeability is only slightly reversible during this short time. The non-linear fracture stiffness model best captures the permeability change mechanisms during this phase too. Although the temperature of the injected fluid is relatively cool, the short injection time does not seem to allow for the diffusion of a strong enough temperature front that would explain the development of thermal strains. It seems that hydro-mechanical fracture dilation processes (tension) were mainly involved in permeability modifications within this small window.

6.2 *Extended* open interval

The *extended* open interval of well 27-15 is used for hydraulic stimulation after the well re-completion in November 2012. This interval is open from ~920 m to ~1770 m in depth and it intersects (and extends beyond) the STF (Figure 8). A large number of microseismic events (MEQs) are observed in the vicinity of well 27-15 at the depth of the STF during every stimulation phase carried out along the *extended* interval. The density and location of the events suggest a direct cause-effect relation exists between stimulation operations and shear deformation on the STF during these phases (Figure 2). The number of MEQs recorded during the *extended* stimulation phase is far greater than during the *shallow*. This is probably due to better access to the STF provided by the *extended* well completion.

When modeling the injection phases relative to the *extended* interval, a temperature of 200º C and pressure of 11 MPa (corresponding to a hydraulic head of 1345 m, evaluated for the mid-point of this open-hole section) are set as initial conditions. The stresses applied to the model are also calculated using a depth of 1345 m (mid-point of the *extended* open interval), with σ_{xx} = 20.3 MPa, σ_{yy} = 26.8 MPa, and σ_{zz} = 33.33 MPa (see Table 1). The enhanced permeability in the volumes surrounding the *shallow* open-hole section of well 27-15, resulting from the preceding *shallow* stimulation phases (medium, high-end pulse), is transferred to the *extended* model. With these initial settings, the simulation of the hydraulic conditions at the beginning of the *extended* stimulation phases reveals an injectivity of ~7.3 kg/s/MPa (0.8 gpm/psi), higher than the pre-EGS baseline injectivity of ~1.8 kg/s/MPa (0.2 gpm/psi), displayed by the 2009 injection test and confirmed by simulations of the baseline conditions (see par. 4.2). This 7.3 kg/s/MPa baseline injectivity reflects the final value obtained as part of the stimulation of the *shallow* interval. This would suggest that the injection-induced shear deformation observed on the STF during the *shallow* stimulation treatments did not contribute to any significant permeability improvement (probably because a sufficient connection between the shallow open interval and the STF had not been established at that time).

The stimulation treatment along this *extended* open-hole section starts with an initial high flow-rate phase (January 15-20, 2013) followed by a long-term low flow-rate phase (February 17 - March 17, 2013).

6.2.1 January 2013 high flow-rate phase

The high flow-rate phase (January 15-20, 2013) in the *extended* open-hole section of well 27-15 is defined by fluid flow rates between 63 and 100 kg/s and well-head pressures of 4.1 to 5.2 MPa. These fluid pressures are close to, but never exceed, S_{hmin} for any point along the *extended* open interval (see Figure 15). Here the injectivity grows from ~7.3 kg/s/MPa to ~22 kg/s/MPa (0.8

gpm/psi to 2.1 gpm/psi). In this study we only model a section of the phase (1 day) available in the literature (Jan 19-20, 2013) [4][17].

Contrary to what is observed during the main *shallow* stimulation phases − where a slow pressure decline indicates permeability enhancements developing over a few days − maximum injectivity (i.e., the lowest WHP for a given flow-rate) is achieved almost immediately during the *extended* stimulation phases. This would imply that a different process, or a new combination of processes (characterized by a different pressure signature at the well-head) govern the main permeability changes for this phase. As introduced above, a clear/direct cause-relation between hydraulic stimulation and microseismicity development at the depth of the STF during this phase is evident. It is possible that during the stimulation of the *extended* interval permeability modifications are linked − at least in part − to shear mechanisms on the STF. In order to answer this question we run separate simulations with the thermo-hydro-mechanical (tension) and shear permeability change models both switched on, then with the thermo-hydro-mechanical (tension) on while the shear is off and vice versa. For runs where thermo-hydro-mechanical (tension) permeability model is switched on, the same fracture parameterization used for the simulation of the *shallow* interval is adopted (i.e. fractures are allowed to dilate under applied stress). However, only if permeability modifications due to shear deformation mechanisms are switched on can the site pressure response and the final injectivity be matched (Figure 16).

The simulation outcomes seem to be in agreement with: 1) less important thermo-hydro-mechanical mechanisms due to injected fluid pressures < S_{hmin}, and 2) rapid permeability as well as WHP changes, revealing highly non-linear shear deformation (further discussion in par. 8). Figure 17 shows the development of temperature, volumetric strain, dilation and shear permeability at the end of the simulated *extended* high flow-rate phase.

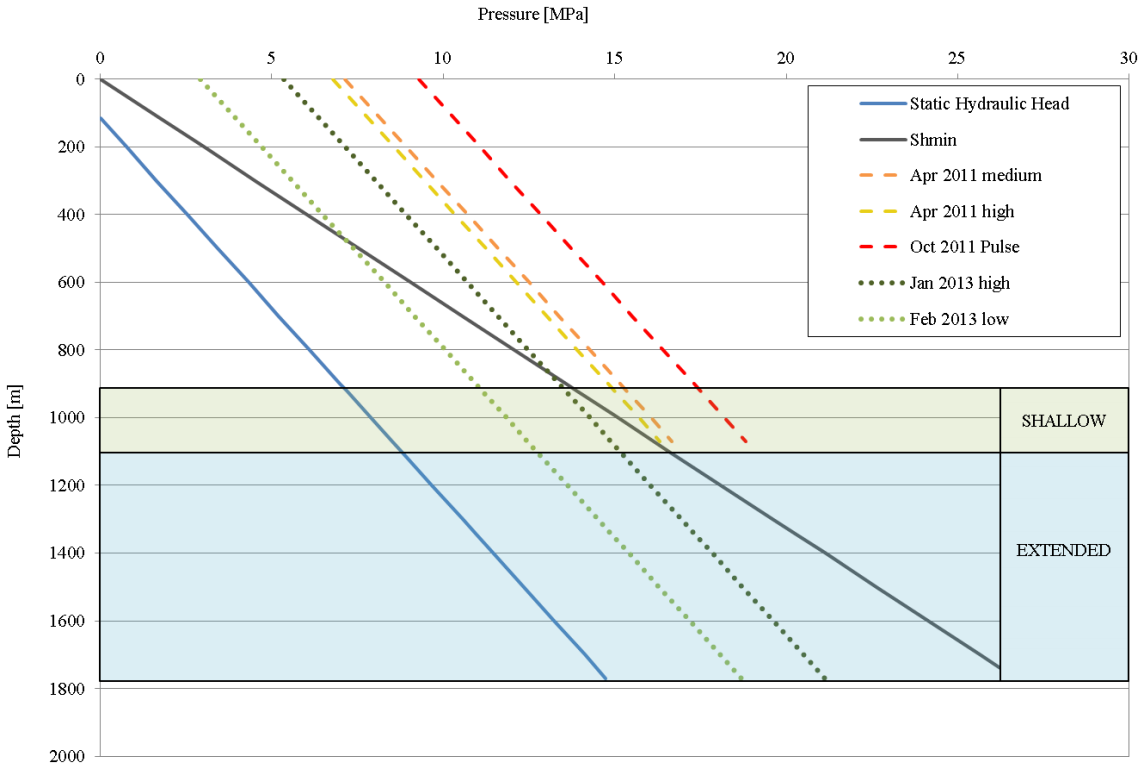

Figure 15 - Stress and fluid pressure gradients expected for the EGS well 27-15 *shallow* and *extended* open intervals. Magnitude of the least horizontal principal stress, S_{hmin} and formation hydraulic head calculated as described in the text and from [16]. Hydraulic fractures (tensile failure) are expected to propagate if a dashed/dotted line pressure (borehole fluid pressures corresponding to specific stimulation phases) exceeds that of the least horizontal principal stress S_{hmin} at the relevant open interval depth.

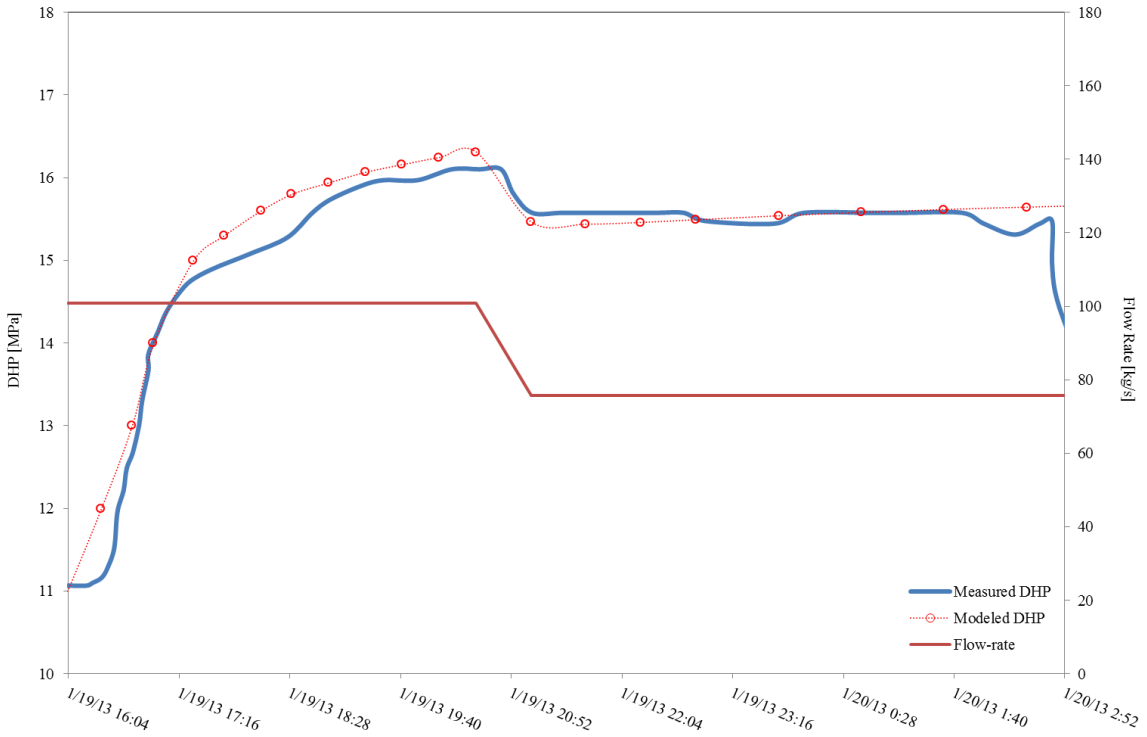

Figure 16 - Measured and TFReact-modeled down-hole pressure (DHP) evolution during the January 19-20, 2013 high flow-rate phase, evaluated for the mid-point of the *extended* EGS well 27-15 open interval (corresponding to ~1345 m depth). An initial 100 kg/s followed by a 76 kg/s flow-rate is injected in EGS well 27-15 to simulate this phase.

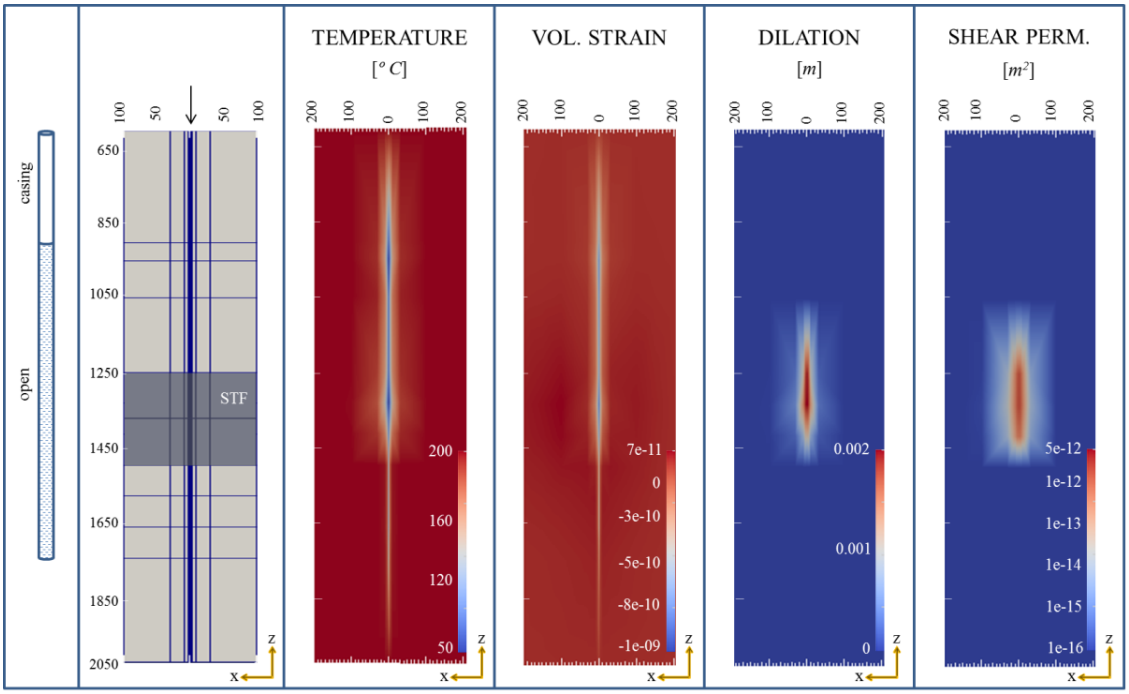

Figure 17 - TFReact output Temperature, Volumetric Strain, Dilation, and Shear Permeability fields at the end of the January 19-20, 2013 *extended* high flow-rate phase simulation. x-z (EW) model slice, depth and horizontal distance from wellbore in meters. Here too, cooler temperature and thermally-induced volumetric strain only diffuse up to ~10 meters around the wellbore. On the other hand, shear permeability gains resulting from plastic deformation of the Shearing Target Fault (STF) affect greater volumes of the reservoir, improving cross-formational connections between EGS well 27-15 and the rest of the reservoir.

6.2.2 February-March long-term, low flow-rate phase

The long-term, low flow-rate phase (February 17 - March 17, 2013) in the *extended* open-hole section of well 27-15 is defined by fluid flow rates of 15.1 to 54.3 kg/s and well-head pressures of 1.4 to 2.8 MPa. These fluid pressures are below S_{hmin} for any point along the *extended* open interval (see Figure 15). The permeability gain detected by the previous simulation is considered in the initial condition set-up of this phase, and the injectivity is confirmed at ~22 kg/s/MPa (2.1 gpm/psi). Based on the approach used to model the *extended* high flow-rate phase (par. 6.2.1),

both permeability change models (tension + shear) are turned on for the simulation of this phase. However, also in this case, thermo-hydro-mechanical (tension) dilation processes appear to have a limited influence on the observed development of permeability, while only hydro-mechanical shear deformation mechanisms are able to reproduce the further monitored gain in injectivity of this low flow-rate phase. This simulated long-term phase does not really seem to improve what was achieved with the high flow-rate phase. This seems to be confirmed by the measured site-injectivity (which does not improve as part of the low flow-rate phase) and a reduced number of induced MEQs during the *extended* low flow-rate phase if compared to the *extended* high flow-rate phase.

6.3 Further simulations

6.3.1 Pressure falloff simulation

The rate at which the pressure in the well falls after the fluid injection is shut in provides some indication of fluid mobility (i.e., permeability) in the formation surrounding the open interval of the well. As a general rule, a long time required to drop by the pressure falloff curve indicates that little space remains for the injected fluid to dissipate in the formation (i.e., low permeability). On the other hand, the steeper the rate of decline of the pressure falloff curve, the higher the permeability and the fracture connection with farther volumes in the reservoir. This behavior is well observed during a number of phases of the Desert Peak project too, and especially as part of the April 2011 controlled hydraulic fracturing phase. Here, as the stimulation treatment progresses, the falloff rate increases and appears to be proportional to the injectivity gain. To simulate the pressure falloff at the end of the April 2011 high flow-rate phase, the high flow-rate simulation is resumed and continued, but with the injection turned off (unloading). When modeling the April 2011 injection treatment the wellbore permeability was kept much higher than the formation permeability to ensure that the wellbore would not affect permeability changes in the reservoir (par. 4.1). This configuration would cause negative pressures to develop in the

model (wellbore) when the injection is shut off. Therefore, to simulate the April 2011 high flow-rate pressure falloff, a low permeability is adopted for the wellbore elements and updated before restarting the simulation. The resulting match between modeled and measured pressure falloff is shown in Figure 18. Given the non-uniformity of the formation surrounding the well, the (more challenging) *extended* interval pressure falloff simulation may be part of a future study.

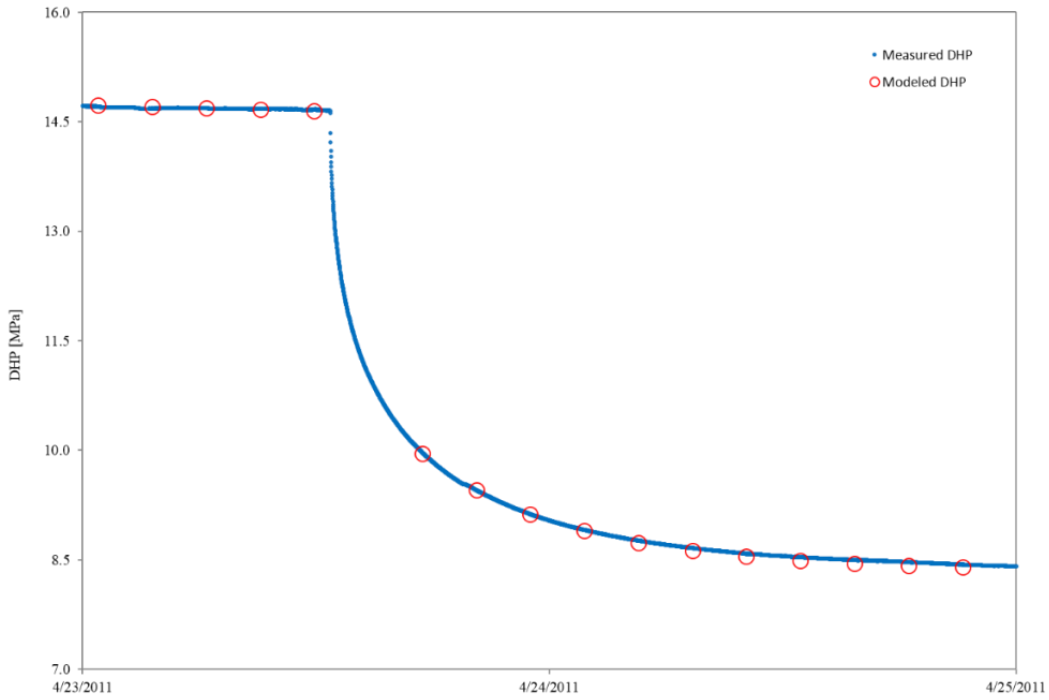

Figure 18 - Well 27-15 April 2011 *shallow* high flow-rate TFReact-modeled pressure falloff, carried out by resuming the April 2011 high flow-rate simulation, but with the injection turned off (unloading) and with impermeable wellbore elements to avoid negative pressure development (initial P offset by ~200 kPa to meet end of high flow-rate phase). The good match between modeled and measured pressure falloff evolution suggests that the enhanced permeability field is correctly simulated.

6.3.2 Unloading and reversibility of mechanisms

As described in par. 0 and 6.2, the permeability gain acquired from each simulation is taken into account by assigning the enhanced values to the relevant elements as initial conditions for the following simulation run. Although we use a plastic Mohr-Coulomb constitutive model for all simulations (i.e., plastic deformation is irreversible), fracture dilation is partly function of the applied stress (fluid pressure) and to some extent it is reversible. We run simulation tests to evaluate the rate at which the enhanced permeability is lost (reversibility) when the injection is turned off (unloading), especially for those phases coming up to a relatively long (weeks) interruption in the stimulation treatment.

When simulating the unloading of the *shallow* interval, the loss of permeability (enhanced) is ~33% and it occurs within the first 50 days from the interruption of the injection. The overall permeability gain (~66%) is maintained in between major injection phases (Figure 19), and is also confirmed by a reduced injectivity loss throughout the EGS experiment. Several minor fluid injection tests carried out in the well may have actually hindered the simulated permeability loss. With regard to the *shallow* stimulation, this seems to imply that most of the permeability gain is related to plastic rather than elastic deformation.

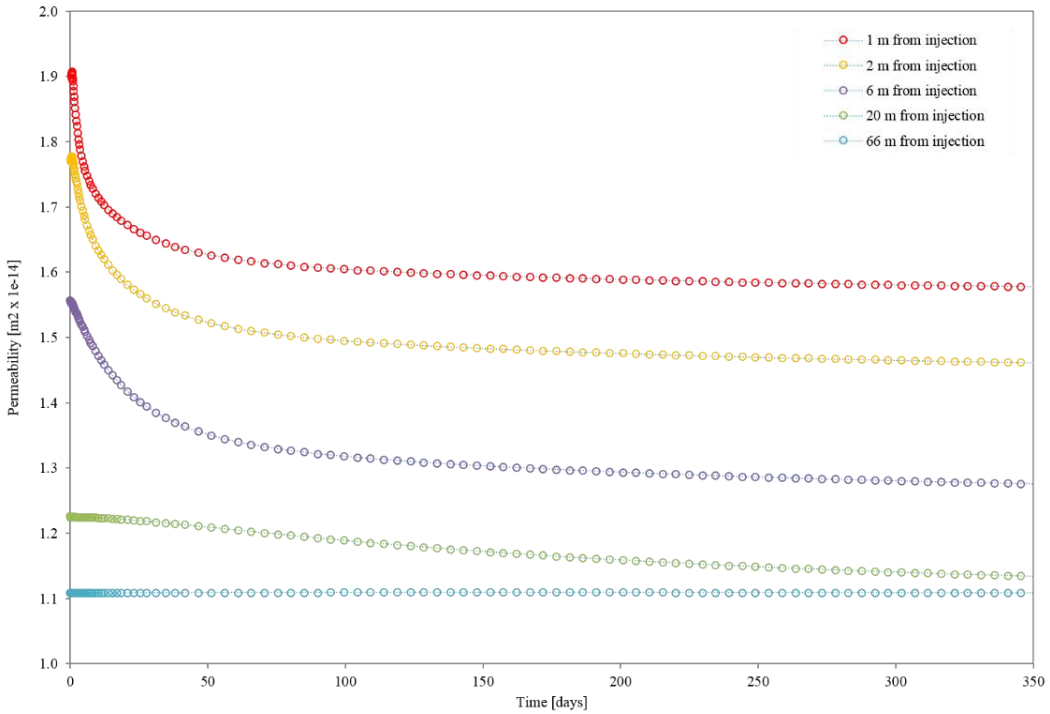

Figure 19 - TFReact-modeled permeability loss following the Apr 2011 *shallow* interval stimulation unloading. All elements shown here have the same 1.1e-14 m^2 initial (pre-April 2011 stimulation) permeability. Permeability is mainly enhanced within the first 10 m from the wellbore and most of it (~70%) is conserved even after a long, simulated unloading period.

The main permeability change process here being plastic (irreversible) deformation/dilation of the STF (Figure 24), the *extended* interval unloading simulation shows that the main permeability gain during this phase (STF volumes) is generally maintained if well 27-15 injection is shut-off for a prolonged time (1 year or longer). This is typically expected with fracture/fault shearing exhibiting extended yielding associated with irreversible changes in the state of the slip plane prior to slip [29].The implementation of the TFReact reactive chemistry component may provide further understanding of a possible long-term permeability reduction due to mineral precipitation; however, it is not part of this study.

6.4 Alternative hydraulic treatment schemes and long-term simulation

6.4.1 *Shallow* interval

Thermo-hydro-mechanical (tension) processes appear to control the evolution of permeability during the *shallow* interval stimulation. We launch a series of further simulation runs to test if the modeled permeability change mechanisms may have improved with the application of different boundary conditions than the ones used as part of the April 2011 medium flow-rate phase. We apply the following ranges separately, as well as in combination with each other: 1) varying fluid temperatures; 2) flow-rates (resulting in a range of fluid pressures); 3) different durations (longer time). With regard to this *shallow* interval, the temperature of the injected fluid influences the rate at which the WHP drops in response to the permeability modifications. Specifically, the lower the temperature of the injected fluid, the steeper the pressure decline at the well-head and the greater the permeability improvement (lower fluid temperature → greater thermal strain → dilation → permeability improvement) (Figure 20).

This is caused by a higher volumetric strain rate developing under the injection of cooler fluids (Figure 21). Cold water injection also produces a higher overpressure than warm water injection and a greater effective stress reduction, and a larger fracture opening tendency occur. However, this hydraulic-induced expansion effect tends to be partly compensated by cold-water-induced thermal strains and corresponding fracture contraction [8].

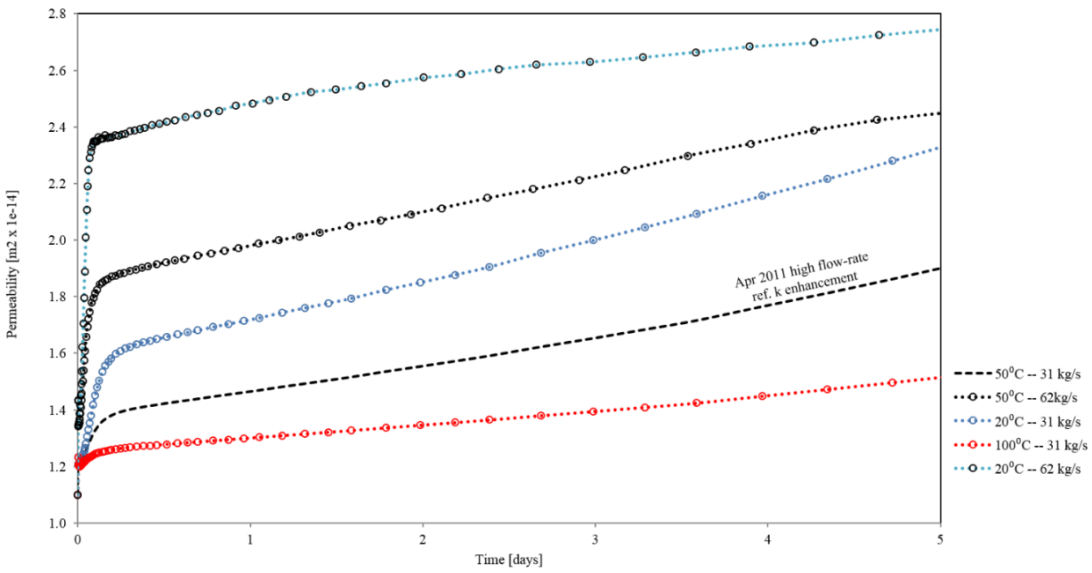

Figure 20 - Well 27-15 April 2011 *shallow* open interval, TFReact-modeled permeability enhancement for alternative scenarios (1 m from injection). Black dashed line is the modeled permeability evolution if the April 2011 medium flow-rate phase injection parameters (~50° C, 31 kg/s) are used. For this *shallow* interval completion, cooler fluids and higher flow rates (especially when combined) would have provided greater permeability gains.

Similarly, higher flow-rates provide greater overpressure and corresponding larger fracture dilation and permeability gain (higher flow-rate → higher pressure (stress) → greater fracture dilation → permeability improvement) (Figure 20).

The April 2011 medium flow-rate phase simulation exercises suggest that: (1) a cooler 20° C fluid would have provided a ~24% further overall permeability gain for the employed 31 kg/s injection rate; (2) a double 62 kg/s injection rate would have resulted in a ~29% higher permeability gain for the applied 50° C injected fluid temperature; and, (3) a combination of cooler 20° C fluid and double 62 kg/s flow-rate would have offered an almost twofold (~45%) permeability gain (Figure 20).

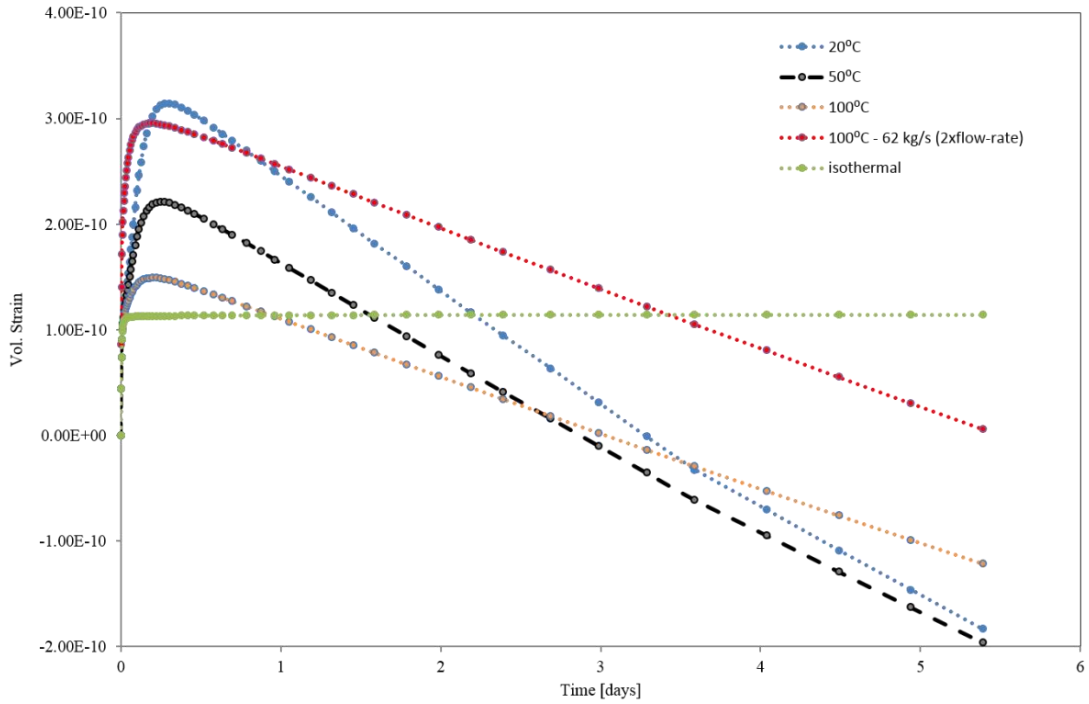

Figure 21 - Well 27-15 *shallow* open interval: TFReact-modeled volumetric strains as a function of fluid temperature (1m from injection). Black dashed line (~50° C) is the approximate reference fluid temperature employed in the April 2011 stimulation. Fluid initially fills and enlarges fractures generating an overall volume expansion; then, the formation is gradually cooled off and thermal contraction (negative volumetric strain) takes place. Cooler fluids generate higher overpressures and contraction rates.

Finally, the conditions employed during the April 2011 *shallow* high flow-rate phase are applied over a longer period to estimate whether prolonged injection in well 27-17 might have offered any further permeability enhancement. The modeled pressure decline continues at the same rate for ~4 more days before leveling out (Figure 22). Therefore, under the April 2011 *shallow* conditions, a much prolonged fluid injection would probably not have been justified. Only if lower temperatures and/or higher flow-rates are applied does the permeability show greater enhancement.

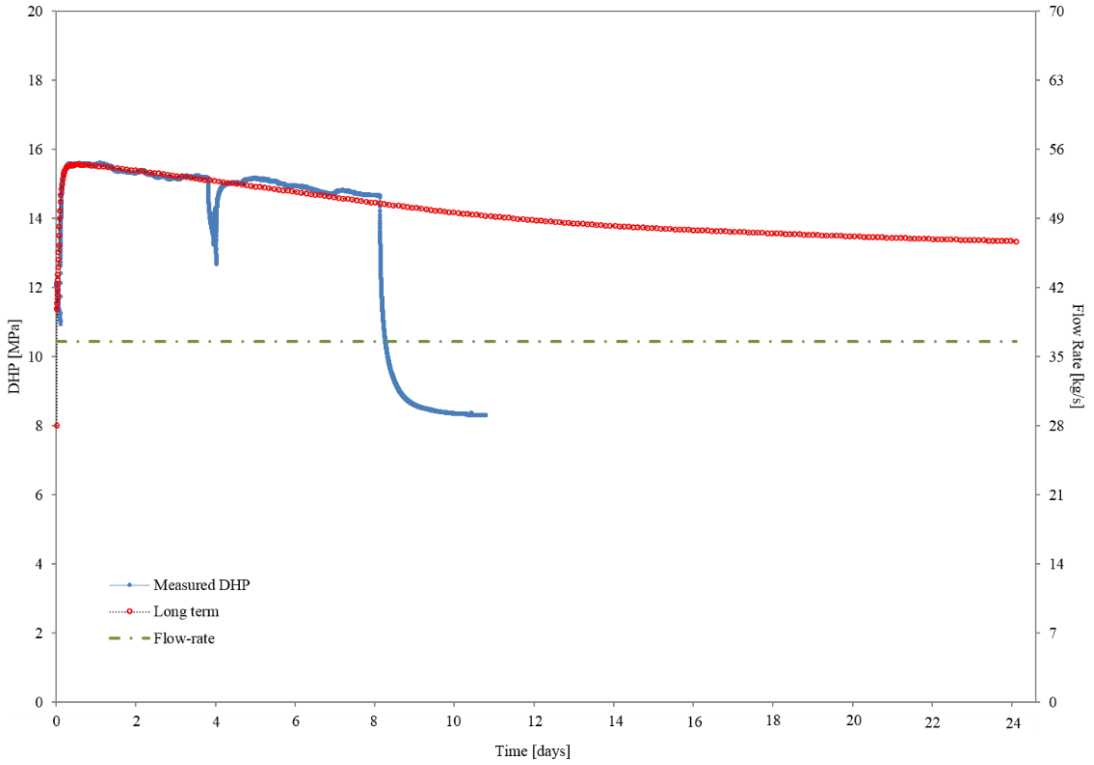

Figure 22 - TFReact-modeled pressure drop (permeability gain) expected from simulating a (hypothetically) longer April 2011 *shallow*, high flow-rate phase. The pressure drop levels after ~4 days, thus a prolonged injection would not have offered a significant enhancement.

6.4.2 *Extended* interval

We now want to test the effectiveness of the stimulation scheme adopted for the *extended* open interval. The injectivity gained from the high flow-rate phase is known, though it is unclear whether the most appropriate sequence was adopted and whether the low flow-rate alone would have produced a better outcome. Therefore, we run alternative simulations where the applied flow-rates are interchanged so that the long-term, low flow-rate phase comes first and the short-term, high flow-rate phase second. The modeling results imply that, given the same conditions, the high flow-rate phase delivers a higher injectivity gain than the low flow-rate phase alone. It

also appears that inverting their order would not affect the results. The higher amount of fluid injected reaches farther volumes and can trigger shear deformation on a larger surface of the STF. Simulation exercises show that lower or higher injectate temperatures would not have changed the final result. On the other hand, a higher injection flow rate shows slightly higher injectivity gains (Figure 23).

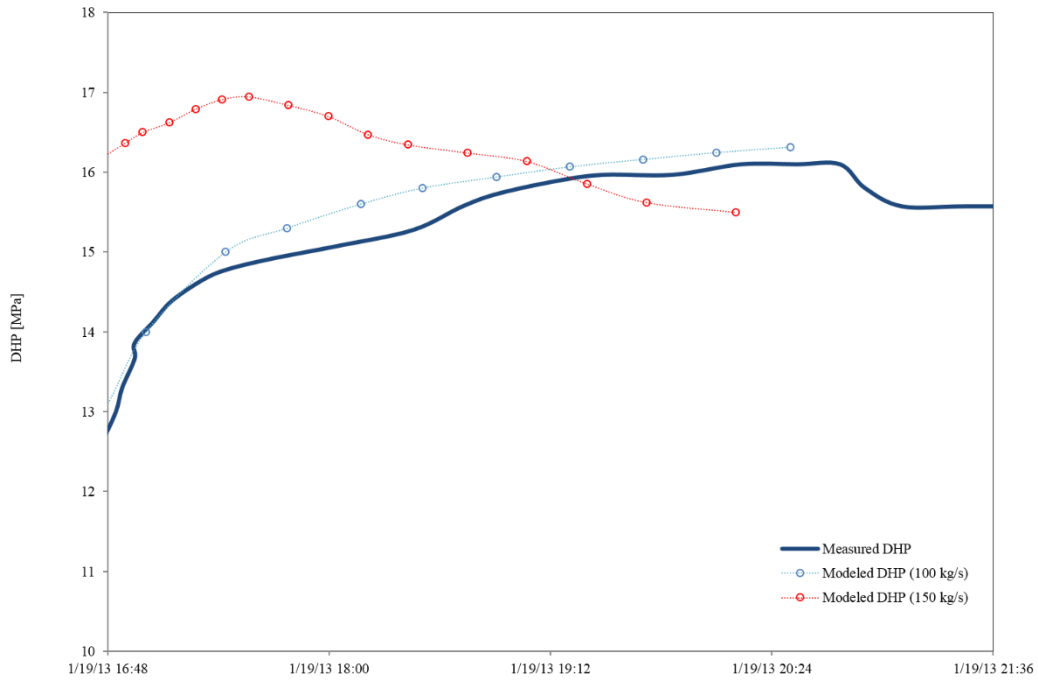

Figure 23 - Well 27-15 January 2013 extended open interval, TFReact-modeled alternative scenarios. Green dotted line is the modeled down-hole pressure corresponding to the fluid flow-rate (~100 kg/s) employed for this phase. Here permeability is mainly enhanced through HM-induced shear deformation on the STF, and modeled higher flow-rates provide a greater injectivity (and permeability) gain. Fluid temperature has minor effect on final permeability for this phase.

We also test whether a direct stimulation of the *extended* open interval (without previous stimulation of the *shallow*) would have provided the well with the same final injectivity. To this

purpose, we run a simulation of the extended interval 2013 injection phases by initializing the entire model with pre-EGS conditions (without considering the permeability enhancements from the *shallow* stimulation phases). The results indicate that the same final 19.2 kg/s/MPa (2.1 gpm/psi) injectivity would still be obtained if only the *extended* interval was stimulated and not the *shallow*.

7 RESULTS

The permeability change mechanisms characterizing selected phases of the Desert Peak EGS experiment (Apr 2011- Mar 2013) are simulated in TFReact and presented here. Our study follows the progression of permeability throughout the course of the main EGS phases for both stimulation treatments in the *shallow* and *extended* open intervals.

A cause-effect relation is evident between stimulation of either the *shallow* or the *extended* intervals and shear deformation on a deep known structural feature (STF). The simulation of the *shallow* interval phases show no connection between observed injectivity improvement and shear failure on the STF, while the simulation of the *extended* interval phases do. As regards the stimulation of the *shallow* interval, the model reveals that the permeability change mechanisms are mainly thermo-mechanical and hydro-mechanical dilation (tension). Conversely, in the stimulation of the *extended* interval, the modeled mechanism seems to be predominantly hydro-mechanical shear dilation (on the STF). A proper match between modeled and monitored pressure responses suggests that the relevant processes are captured.

The simulation of the pressure falloff at the end of selected phases (April 2011 high flow-rate) and the good fit between modeled and observed curves supports the modeling results further, indicating that the enhanced permeability field is correctly represented.

The calculated permeability modifications reveal some reversibility, mainly related to hydro-mechanical fracture-closure mechanisms during unloading of the *shallow* interval. On the other hand, the permeability gained as part of the *extended* interval stimulation is mainly irreversible.

Concerning the *shallow* interval, the simulation of alternative injection scenarios indicates that the April 2011 high flow-rate observed pressure drop (permeability enhancement) would have continued for ~4 extra days before stabilizing had fluid injection not been interrupted. The April 2011 medium flow-rate modeling results show that a comparable additional permeability enhancement (~24 to 30%) might have been offered by the employment of either higher fluid pressure or lower fluid temperature. Further cooling down fluid prior to injecting (or using fluid from nearby streams instead of spent brines) may be a less expensive practice than increasing the injection fluid pressure, although this is site-specific.

Regarding the *extended* interval, simulation results suggest the Jan 2013 high flow-rate phase generates a higher permeability gain if compared to the Feb-Mar 2013 long-term, low flow-rate phase. If fact, most of the permeability gain obtained during the *extended* interval stimulation is observed as part of the January 2013 high flow-rate phase. The model also implies that the same final 2.1 gpm/psi injectivity would have been reached if no stimulation of the *shallow* interval, but only of the *extended*, had been carried out. Here, higher flow rates generate higher injectivity gains with the current configured/calibrated model (Figure 23). Most of the induced microseismicity develops during the time window January 15-20 2013 (*extended* high flow-rate → major modeled and measured permeability gain), while a reduced number of MEQs is observed between February and March 2013 (*extended* long-term, low flow-rate phase → minor/subordinate modeled and measured permeability gain). Rapid changes in the injection flow rate (both positive and negative) also generate observable injectivity/permeability improvements.

At all times, concurrent fluid injection in well 22-22 and/or 21-2 does not seem to affect the permeability improvements observed around well 27-15.

8 DISCUSSION AND CONCLUSIONS

The TFReact model of the main Desert Peak EGS stimulation treatments provides important insights into the permeability change processes activated for given sets of injecting conditions.

Through the simulation and match of the observed WHP responses, thermo-mechanical and hydro-mechanical processes (tension) are found to govern permeability enhancement during the main medium and high flow-rate stimulation phases of the *shallow* interval of well 27-15. These processes yield maximum gains only if injection conditions are applied over a relatively long time and without interruption. They seem to be controlled by pressure and temperature diffusion from the wellbore radially toward more distant volumes. The slow and constant decline of the WHP curve reflects the physics and linearity of these processes. Gradual and linear declines in down-hole pressure under constant flow-rate resulting from cold water injection are observed in other similar cases [27].

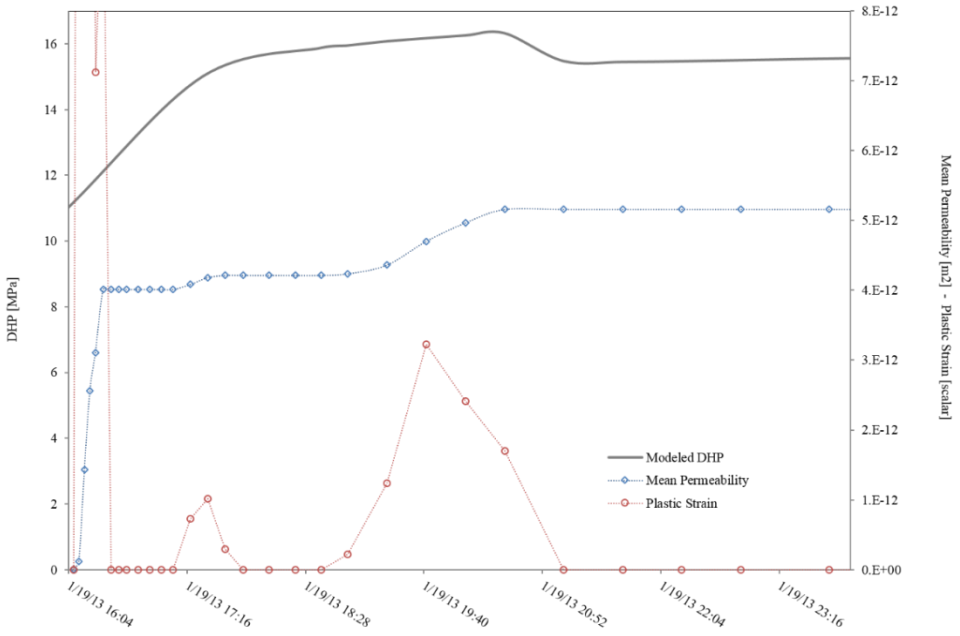

Figure 24 - *Extended* open interval simulation (1 m from injection): the main permeability changes occur as a result of plastic strain (shear deformation).

The development of permeability related to these processes is limited to volumes near the wellbore (~6-10 m), as fluid pressure drops below S_{hmin} at a small distance from the open interval (Figure 25), and given that an effective temperature only diffuses to a maximum distance of ~10 meters (Figure 26).

Conversely, shear failure processes developing on a well-known structural feature (STF) seem to control most of the permeability gain produced during the well 27-15 *extended* interval stimulation (Figure 24). Field observations from analogous projects have shown that the main injectivity gains are usually observed within shear zones [20][14]. Shear failure is a sudden release of energy on fracture and fault planes [28] and, consequently, shear permeability development is highly non-linear and almost instantaneous. This is well observed in the WHP curve, which almost immediately reflects the value associated with the highest injectivity. This behavior was also detected during the Basel EGS project, where occurrence of sudden pressure drops was found to be the expression of shear displacement along pre-existing fractures [29]. The modeled shear permeability appears to be more effective than thermo-hydro-mechanical (tension) permeability mechanisms, because (1) it provides higher final values, (2) it affects larger volumes of the reservoir, and (3) it is mostly irreversible (Figure 27).

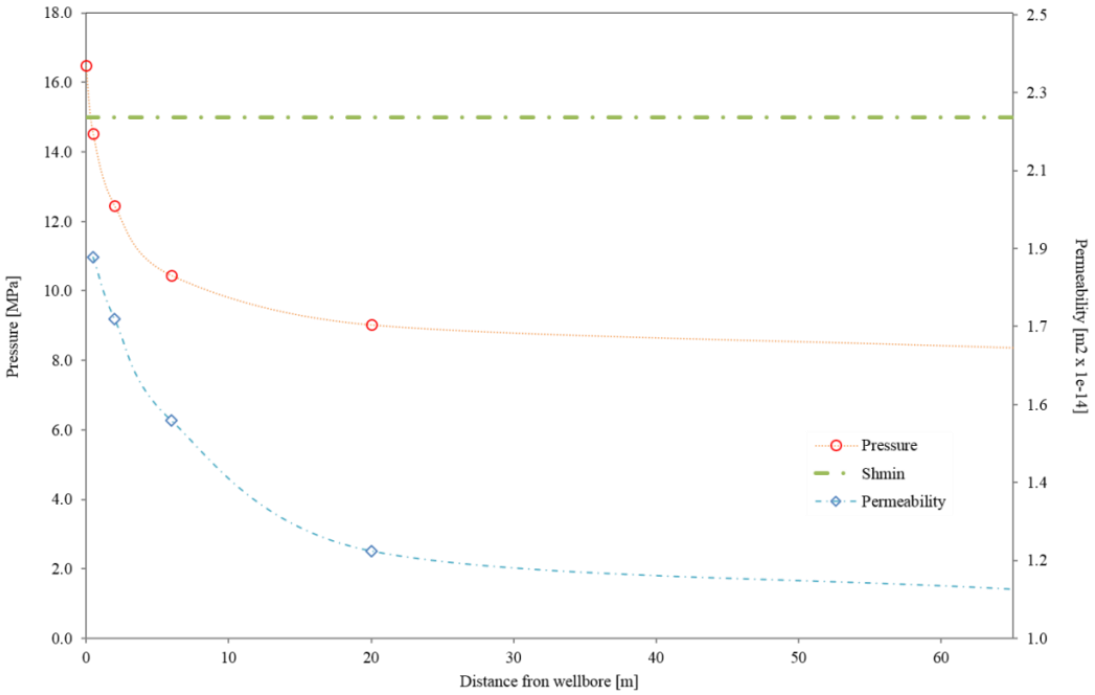

Figure 25 - Well 27-15 Apr 2011 *shallow* open interval, end of medium flow-rate phase (~995 m depth): TFReact-modeled correlation between injection-induced down-hole pressure and permeability as a function of wellbore distance. Some permeability change is − at least partly − pressure-driven (HM) (tension). Hydraulic fractures are only expected to develop within the formation immediately surrounding the open interval, as fluid pressure drops below S_{hmin} at a small distance from the injection.

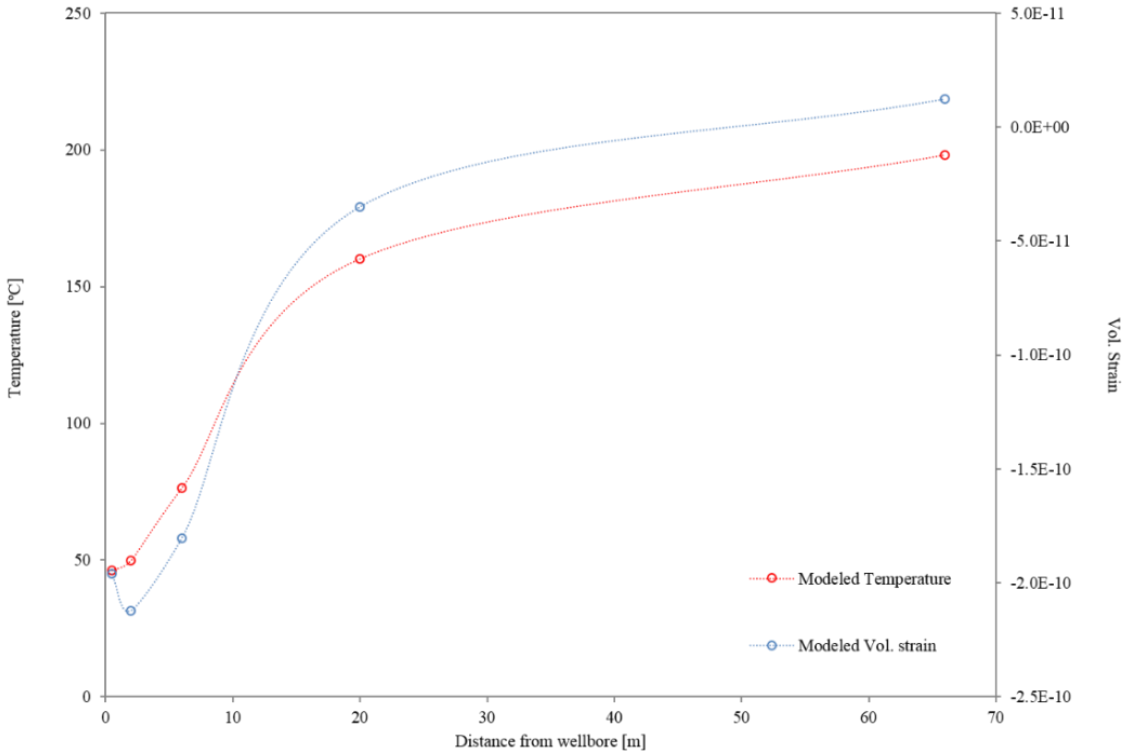

Figure 26 - Well 27-15 Apr 2011 *shallow* open interval, medium flow-rate phase: TFReact-modeled correlation between injection-induced temperature front and volumetric strain as a function of wellbore distance. Negative volumetric strains (contraction) develop within the first ~10 m from the wellbore and evolve following the temperature front diffusion.

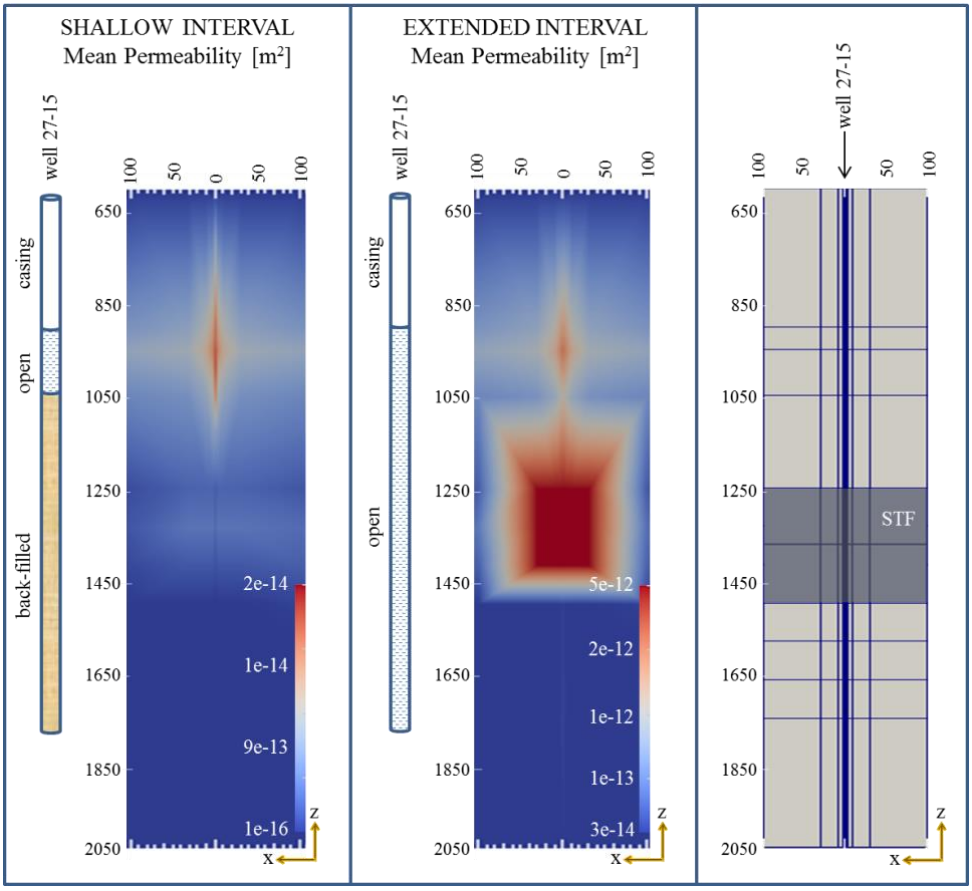

Figure 27 - TFReact output comparison between Mean Permeability field at the end of the April 2011 *shallow* and at the end of the January 2013 *extended* stimulation phases. x-z (EW) model slice, depth and horizontal distance from wellbore in meters. The simulated THM-induced (tension) permeability enhancements obtained during the *shallow* interval stimulation is limited to the formation immediately surrounding the EGS well. Conversely, HM-induced (shear) permeability enhancements developed as part of the *extended* interval stimulation (which targeted the STF) are considerably larger and provide more effective cross-formational connections between well 27-15 and the rest of the reservoir.

We argue that the different processes controlling the enhancement of permeability during the stimulation of the *shallow* and *extended* open intervals show two distinct signatures at the well-head (pressure curve), and this is confirmed by coupled THM simulation results. This interpretation is in agreement with observations made as part of similar projects [27] [29].

Injection-induced microseismicity develops on a deep structural feature (STF) during all of the main stimulation phases (from Apr 2011 to Mar 2013, *shallow* and *extended*). The cause-effect relation between injection operations in well 27-15 (especially if concurrent with well 22-22) and microseismicity is supported by previous and current modeling results. The present study shows that the STF shear deformation does not generate detectable permeability changes during the stimulation of the *shallow* interval. Yet, the STF is key to the success of the subsequent January-March 2013 *extended* interval stimulation, during which direct stimulation of the STF caused extensive shear deformation (and associated microseismic swarms) associated with a significant injectivity improvement (highest permeability gain in the entire experiment). The relation between fluid injection and shear deformation is critical. It appears that, during the *shallow* interval stimulation MEQs highlighted a geological structure prone to shear deformation and permeability enhancement (STF): an attractive target which was in fact intersected by the new, extended well completion, and successfully stimulated. An element of note is that modeling results suggest that the *extended* interval stimulation would have achieved the same final injectivity even if the well had not previously undergone any *shallow* stimulation.

Shear displacement is known to occur in a discontinuous (stick-slip) as well as continuous (creep-like, mostly aseismic) manner [29][36][3][21][22][24][33]. In this paper we mainly refer to stick-slip shear deformation, as this is the most probable type of displacement associated with the observed microseismicity and greatest permeability gains. However, during some phases of the *shallow* interval stimulation (i.e., April 2011), the occurrence of some creep-like shear − facilitated by thermal damage/degradation − cannot be excluded. Given the almost aseismic nature of creep-like shearing and THM (tension) dilation processes (for the available microseismic network), only by comparing pre- and post-stimulation borehole logs, and if small-scale slip motions of pre-existing fractures on the borehole wall are present, would it be possible to discriminate one of the two mechanisms [6]. Nonetheless, since both mechanisms are expected

to be strongly thermo-hydraulically driven, the fundamental April 2011 physical processes are correctly captured by this simulation work.

The THMC simulation approach presented here − based on the calibration and modeling of actual hydraulic stimulation treatments − is a successful methodology applicable to the design and decision-making processes prior to, during and after any hydraulic stimulation treatment in geothermal environments. It can be used to test the stimulation plan prior to its implementation, to predict the affected reservoir volumes and expected permeability changes. During stimulation the method can be used to establish whether injection choices are to be adjusted in order to optimize results.

These results show how much a successful and economically-viable stimulation strongly depends upon the understanding of the permeability mechanisms that can or cannot be activated for given geological, structural, tectonic and adopted well completion characteristics. The importance of calibrating numerical simulations on site-specific, complex, real-world geologic and structural settings is also evident from this study.

This modeling work constitutes the basis for further in-depth analyses concerning: (1) the simulation of permeability modifications associated with fluid circulation through the newly-enhanced fracture permeability over extended operational times (life-cycle analysis), which would ideally require the implementation of the TFReact reactive chemistry component, and (2) induced-seismicity evolution simulation at Desert Peak, following similar recent investigations [19][13], which would provide further constraints and insights for applications of TFReact to future case studies. This Desert Peak TFReact model construction and approach could be employed with minor adjustments for the simulation of hydraulic treatments carried out in similar structural and tectonic settings (i.e., Bradys EGS project [39]).

ACKNOWLEDGMENTS

This work is supported by the Desert Research Institute through a DHS fund and by the Itasca Education Partnership (IEP). The first author wishes to acknowledge Gan Quan and Prof. Derek Elsworth for assisting with the TFReact mass flow rate implementation/function, as well as Prof. Greg Pohll for providing comments/feedback while reviewing the document.

REFERENCES

[1] Benato, S., Hickman, S., Davatzes, N.C., Taron, J., Spielman, P., Elsworth, D., Majer, E.L., Boyle, K., Desert Peak EGS Project: Reservoir Response to the Shallow Medium Flow-Rate Hydraulica Stimulation, Conceptual Model and Numerical Analysis, (in preparation for submission to Geothermics EGS Special Issue).

[2] Benato, S., Reeves, D.M., Parashar, R., Davatzes, N.C., Hickman, S., Elsworth, D., Spielman, P., Taron, J., Computational Investigation of Hydro-Mechanical Effects on Transmissivity Evolution During the Initial Injection Phase at the Desert Peak EGS Project, NV, Proceedings, 38th Workshop on Geothermal Reservoir Engineering, Stanford University, Stanford, California, February 11-13, 2013, SGP-TR-198.

[3] Byerlee, J., Friction of Rocks, Pageoph, Vol. 116 (1978), Birkhfiuser Verlag, Basel.

[4] Chabora, E., Zemach, E., Desert Peak EGS Project, Geothermal Technologies Program 2013 Peer Review, DOE Award: DE-FC6-02ID14406.

[5] Chabora, E., Zemach, E., Spielman, P., Drakos, P., Hickman, S., Lutz, S., Boyle, K., Falconer, A., Robertson-Tait, A., Davatzes, N.C., Rose, P., Majer, E., Jarpe, S., Hydraulic stimulation of well 27-15, Desert Peak Geothermal Field, Nevada, USA, Proceedings, 37th Workshop on Geothermal Reservoir Engineering, Stanford University, Stanford, California, January 30 - February 1, 2012, SGP-TR-194.

[6] Cornet, F. H., Helm, J., Poitrenaud, H., Etchecopar, A., Seismic and Aseismic Slips Induced by Large-scale Fluid Injections, Pure appl. geophys. 150 (1997) 563–583.

[7] Davatzes, N.C. and Hickman, S., Fractures, stress and fluid flow prior to stimulation of well 27-15, Desert Peak, Nevada, EGS project, Proceedings, 34th Workshop on Geothermal Reservoir Engineering, Stanford University, Stanford, California, February 9-11, 2009 SGP-TR-187.

[8] De Simone, S., Vilarrasa, V., Carrera, J., Alcolea, A. and Meier, P., Thermal coupling may control mechanical stability of geothermal reservoirs during cold water injection, Journal of Physics and Chemistry of the Earth, 64: 117-126.

[9] Dempsey, D., Kelkar, S., Lewis, K., Hickman, S., Davatzes, N., Moos, D., Zemach, E., Modeling Shear Stimulation of the Desert Peak EGS Well 27-15 Using a Coupled Thermal-Hydrological-Mechanical Simulator, Proceedings 47th US Rock Mechanics/Geomechanics Symposium, San Francisco, California, USA, 23-26 June 2013.

[10] Drakos, P., Ormat Nevada Inc., Desert Peak EGS Project, Geothermal Technologies Program 2010 Peer Review, DOE: DE-FC6-02ID14406, May 18, 2010.

[11] Faulds, J.E., Coolbaugh, M.F., Benoit, D., Opplinger, G., Perkins, M., Moeck, I., Drakos, P., Structural controls of geothermal activity in the Northern Hot Spring Mountains, Western Nevada: the tale of three geothermal systems (Brady's, Desert Peak, and Desert Queen), Geothermal Resources Council Transactions, Vol. 34, 2010.

[12] Faulds, J.E., Ramelli, A.R., Garside, L.J., Coolbaugh, M.F., and Green, H.L., (2012), Preliminary geologic map of the Desert Peak Quadrangle, Churchill County, Nevada, Nevada Bureau of Mines and Geology Open-File Report 12-5, scale 1:24,000.

[13] Gan, Q., Elsworth, D., Analysis of fluid injection-induced fault reactivation and seismic slip in geothermal reservoirs, J. Geophys. Res. Solid Earth, 119, 3340–3353, doi:10.1002/ 2013JB010679.

[14] Gentier, S., Rachez, X., Dezayes, C., Blaisonneau, A., Genter, A., How to Understand the Effect of the Hydraulic Stimulation in Terms of Hydro-Mechanical Behavior at Soultz-sous-Forêts (France), GRC Transactions, Vol. 29, 2005.

[15] Hickman, S., Stress in the lithosphere and the strength of active faults, U.S. National Report to the International Union of Geodesy and Geophysics 1987-1990, Reviews of Geophysics, v. 29, p. 759-775.

[16] Hickman, S. and Davatzes, N.C., In-situ stress and fracture characterization for planning of an EGS stimulation in the Desert Peak Geothermal field, Nevada, Proceedings, 35th Workshop on Geothermal Reservoir Engineering, Stanford University, Stanford, California, February 1-3, 2010 SGP-TR-188.

[17] Hickman, S., Davatzes, N.C., Zemach, E., Chabora, E., Lutz, S., Majer, E., Spielman, P., Robertson-Tait, A., Rose, P., Dempsey, D., Kelkar, S., Moos, D., Stress and Fracture Characterization for EGS Stimulation: The Desert Peak Project, Abstract Volume 2013, International Conference on EGS, Potsdam, Germany, May 27, 2013.

[18] Itasca FLAC3D manual, Fast Lagrangian Analysis of Continua in 3 Dimensions - version 4.0. Minneapolis, MN, Itasca Consulting Group Inc., 2011.

[19] Izadi, G., Elsworth, D., The influence of thermal-hydraulic-mechanical- and chemical effects on the evolution of permeability, seismicity and heat production in geothermal reservoirs, Geothermics 53 (2015) 385–395.

[20] Jeanne, P., Rutqvist, J., Hartline, C., Garcia, J., Dobson, P.F., Walters, M., Reservoir structure and properties from geomechanical modeling and microseismicity analyses associated with an enhanced geothermal system at The Geysers, California, Geothermics 51 (2014) 460–469.

[21] Jupe, A.J., Green, A.S.P., Wallroth, T., Induced Microseismicity and Reservoir Growth at the Fjällbacka Hot Dry Rocks Project, Sweden, Int..L Rock Mech. Min. Sci. & Geomech., Abstr. Vol. 29. No. 4. pp. 343-354, 1992.

[22] Lockner, D.A., Byerlee, J.D., Dilatancy in hydraulically isolated faults and the suppression of instability, Geoph. Res. Letters, Vol. 21, No. 22, pp. 2353-2356, November 1, 1994.

[23] Lutz, S.J., Hickman, S., Davatzes, N., Zemach, E., Drakos, P., Robertson-Tait, A., Rock mechanical testing in support of well stimulation activities at the Desert Peak geothermal field, Nevada, Geothermal Resources Council Transactions, Vol. 34, 2010.

[24] Marone, C., Laboratory-derived Friction Laws and their Application to Seismic Faulting, Annu. Rev. Earth Planet. Sci. 1998. 26:643–96.

[25] Min, K-B, Rutqvist, J., Tsang, C-F, Jing, L., Stress-dependent permeability of fractured rock masses: a numerical study, International Journal of Rock Mechanics & Mining Sciences, 41 (2004) 1191–1210.

[26] Min, K-B, Rutqvist, R., Elsworth, D., Chemically and mechanically mediated influences on the transport and mechanical characteristics of rock fractures, Int. J. Rock. Mech. Min. Sci., 2008, doi:10.1016/j.ijrmms.2008.04.002.

[27] Nakao, S., Ishido, T., Pressure Transient Behavior during Cold Water Injection into Geothermal Wells, Geothermics Vol 27, No. 4, pp. 401-413, 1998.

[28] Ohnaka, M., (2013), The Physics of Rock Failure and Earthquakes, Cambridge University Press publishing, Cambridge CB2 8RU, UK, 279 p.

[29] Ortiz, A.E.R., Renner, J., Jung, R., Hydromechanical analyses of the hydraulic stimulation of borehole Basel 1, Geophys. J. Int. (2011) 185, 1266–1287, doi: 10.1111/j.1365-246X.2011.05005.x.

[30] Pruess, K., Oldenburg, C., Moridis, G., TOUGH2 User's Guide, Earth Sciences Division, Lawrence Berkeley National Laboratory, University of California, Berkeley, CA, revised September 2012.

[31] Rahman, M.K., Hossain, M.M, Rahman, S.S., A shear-dilation-based model for evaluation of hydraulically stimulated naturally fractured reservoirs, Int. J. Numer. Anal. Meth. Geomech., 2002; 26:469–497 (DOI: 10.1002/nag.208).

[32] Rosso, R.S., A Comparison of Joint Stiffness Measurements in Direct Shear, Triaxial Compression, and In Situ, Int. J. Rock Mech. Min. Sci. & Geomech. Abstr. Vol. 13, pp. 167-172.

[33] Rutledge, J.T., Phillips, W.S., Mayerhofer, M.J., Faulting Induced by Forced Fluid Injection and Fluid Flow Forced by Faulting: An Interpretation of Hydraulic-Fracture Microseismicity,Carthage Cotton Valley Gas Field, Texas, Bulletin of the Seismological Society of America, Vol. 94, No. 5, pp. 1817–1830, October 2004.

[34] Rutqvist, J., Birkholzer, J.T., Tsang, C-F, Coupled reservoir geomechanical analysis of the potential for tensile and shear failure associated with CO2 injection in multilayered reservoir–caprock systems, International Journal of Rock Mechanics & Mining Sciences 45 (2008) 132–143.

[35] Rutqvist, J., Determination of Hydraulic Normal Stiffness of Fractures in Hard Rock from Well Testing, Int. J. Rock Mech. Min. Sci. & Geomech. Abstr. Vol. 32, No. 5, pp. 513-523, 1995.

[36] Scholz, C.H., Engelder, J. T., The role of asperity indentation and ploughing in rock friction - Asperity creep and stick-slip, Int. Rock Mech. Min. Sci. 13, 149-154.

[37] Sherburn, S. and Quinn, R., An Assessment of the Effects of Hydraulic Fracturing on Seismicity in the Taranaki Region, (2012), GNS Science Consultancy Report 2012/50, February 2012.

[38] Snow, D.T., Anisotropic permeability of fractured media, Water Resources Research, 1969, 5(6):1273–89.

[39] Snyder, K., Zemach, E., Bradys EGS project, DOE: DE-FG36-08GO18200, Geothermal Technologies Program 2013 Peer Review, April 22, 2013.

[40] Stacey, R.W., Robertson-Tait, A., Drakos, P., Zemach, E., EGS stimulation of well 27-15, Desert Peak geothermal field, Nevada, Geothermal Resource Council Transactions, Vol. 34, 2010.

[41] Taron, J., (2011), TFReact v2.0 User Manual, TOUGHREACT-FLAC3D modular THMC simulator for complex environments.

[42] Taron, J., Elsworth, D., Kolditz, O., Evolution of Permeability in Fracture Networks: Geophysical and Geochemical Effects in Enhanced Geothermal Systems, GRC Transactions, Vol. 34, 2010.

[43] Taron, J., Elsworth, D., Min, K-B, Numerical simulation of thermal-hydrologic-mechanical-chemical processes in deformable, fractured porous media, Int J Rock Mech Mining Sci (2009), doi:10.1016/j.ijrmms.2009.01.008.

[44] Taron, J., Elsworth, D., Roles and Timing of Onset of Various Thermal-Hydrologic-Mechanical-Chemical Process Couplings in EGS Reservoirs, GRC Transactions, Vol. 33, 2009.

[45] Taron, J., Elsworth, D., Thermal–hydrologic–mechanical–chemical processes in the evolution of engineered geothermal reservoirs, International Journal of Rock Mechanics & Mining Sciences 46 (2009) 855–864.

[46] Taron, J., Hickman, S., Ingebritsen, S.E, and Williams, C., Using a fully coupled, open-source THM simulator to examine the role of thermal stresses in shear stimulation of enhanced geothermal systems, 48th US Rock Mechanics / Geomechanics Symposium held in Minneapolis, MN, USA, 1-4 June 2014, ARMA 14-7525.

[47] Townend, J., and Zoback, M. D., (2000), How faulting keeps the crust strong, Geology, v. 28, p. 399–402.

[48] Warren, J.E., Root, P.J., The behavior of naturally fractured reservoirs. Soc. Pet. Eng. J., Transactions, AIME, 228, 245-255, September 1963.

[49] Witherspoon, P.A., Wang, J.S.Y., Iwai, K., Gale, E., Validity of cubic law for fluid flow in a deformable rock fracture. Water Resources Research 1980, 16(6):1016–24.

[50] Xu, T., E. Sonnenthal, N. Spycher, and K. Pruess (2004), TOUGHREACT User's Guide: A simulation program for non-isothermal multiphase reactive geochemical transport in variable saturated geologic media, Earth Sciences Division, Lawrence Berkeley National Laboratory, Univ. of California, Berkeley, Calif.

[51] Zemach, E., Drakos, P., Robertson-Tait, A., Lutz, S.J., Feasibility evaluation of an "in-field" EGS project at Desert Peak, Nevada, USA, Proceedings World Geothermal Congress, Bali, Indonesia, 25-29 April 2010.

6 RESULTS

In order to define a possible connection between stimulation operations in well 27-15 and the development of the observed MEQs and offer a possible explanation for their deep location, as well as test the mechanisms responsible for the observed permeability evolution, the present research analyzes: (1) 3D site-specific geometry of the key structures involved in the experiment, (2) 3D equivalent permeability tensors in a representative Discrete Fracture Network (DFN) model consistent with observations of the fracture network, hydraulically-conductive fractures within well 27-15 in particular, (3) assessment of permeability distribution based on integrating DFN analysis, injectivity tests, pressure response modeling and interference test modeling, (4) FLAC3D Hydro-Mechanical simulation of pore pressure diffusion and resulting mechanical deformation consistent with the activation of hydraulically-induced shear failure in the reservoir, and (5) TFReact permeability change simulations.

6.1 Statistical fracture network analysis

The data set measured by *Davatzes and Hickman, 2009* from FMS and ABI85 image logs in well 27-15 is used to generate a representative statistical fracture network to simulate the corresponding fluid flow in the rock volume containing the well. A total of 261 discrete fractures sampled over a length of 778 m yields a fracture frequency of 0.3 fractures/m and an average fracture spacing of 3 m. Two identified main fracture clusters represent the most probable fracture populations (cluster 1 = 27.2%, cluster 2 = 43.7%), with the remaining 29.1% of fractures randomly distributed. These two antithetic fracture sets are in agreement with structures observed at the field scale, and Cluster 2 is particularly consistent with the Rhyolite Ridge Fault Zone striking and dipping directions. A scaling approach combining the total number of flowing fractures identified by temperature/spinner anomalies with the permeability thickness value

measured during hydrologic tests yields a mean hydraulic aperture of 30 μm. Fracture length is assumed to be distributed according to a power-law with exponent *a*=2.

6.2 Discrete Fracture Network (DFN) model

The DFN correctly reproduces regional structural trends observed at the field scale from surface mapping, fracture attitudes and densities from borehole observations and borehole log temperature anomalies. Geometric and flow techniques identify the interconnected subset of fractures responsible for conducting flow across the model. By computing hydraulic conductivity from fracture apertures, the generated DFN model evaluates permeability tensors (k_x=2.50-17 m^2, k_y=1.83e-16 m^2, k_z=6.16e-17 m^2) for the volume containing well 27-15. The results are in very good agreement with the on-site measured permeability for the formation surrounding the open-hole section of the well. Results emphasize a preferential flow through k_y and k_z relative to k_x, in accordance with the trends of the major structural features. The existing natural fracture network supports vertical fluid flow and represents a preferential pathway through which injected fluids can reach greater depths.

6.3 FLAC3D simulations

The reservoir's mechanical response resulting from injection operations into the well 27-15 *shallow* open-hole section (September 2010 and April 2011 conditions) is simulated in FLAC3D to verify possible conditions for deformation and shear failure initiation. Numerical modeling results reveal that pore pressure diffusion to depths below the *shallow* stimulation interval can lead to pressurization and poromechanical stressing of the STF, especially when combined with injection operations in well 22-22. When the April 2011 medium flow-rate phase is simulated, conditions for tensile failure also develop in volumes surrounding the well 27-15 open-hole section, in agreement with injection-induced fluid pressures exceeding S_{hmin}. The FLAC3D model shows a localized pressurization of the STF and pore pressure incremental up to 1.0 MPa. The

corresponding effective stress changes – also according to analytical Mohr-Coulomb analyses – are sufficient to satisfy conditions for shear failure within the STF. FLAC3D simulation results show that shear deformation at the depth of the STF and toward well 27-15 is enhanced when both wells 27-15 and 22-22 are actively injecting fluid. Pore pressure diffusion from concurrent injection in wells 27-15 and 22-22 may combine, further destabilizing the STF. Shear failure distribution shown in the modeling results is in agreement with the location of the observed microseismicity, which appears to cluster mainly in the same depth range as the STF below the *shallow* stimulated interval of well 27-15.

6.4 TFReact simulations

The TFReact modeling analysis follows the progression of permeability throughout the course of the main EGS phases for both stimulation treatments in the *shallow* and *extended* open intervals. As regards the stimulation of the *shallow* interval, the model reveals that the permeability change mechanisms are mainly thermo-mechanical and hydro-mechanical dilation (tension). Conversely, in the stimulation of the *extended* interval, the modeled mechanism seems to be predominantly hydro-mechanical shear dilation (on the STF). A proper match between modeled and monitored pressure responses suggests that the relevant processes are captured. The calculated permeability modifications reveal some reversibility, mainly related to hydro-mechanical fracture-closure mechanisms during the unloading of the *shallow* interval. On the other hand, the permeability gained as part of the *extended* interval stimulation is mainly irreversible.

7 CONCLUSIONS

The identified Shearing Target Fault (STF) satisfies some of the necessary conditions for shear failure initiation: 1) adequate initial transmissivity, (2) optimum orientation with respect to the local stress state, and (3) enhanced transmissivity with slip. The conceptual framework provides a

geologically-reasonable model for the April 2011 Desert Peak EGS experiment in that it tests the role of the STF in focusing induced deformation manifested by MEQs.

In agreement with the microseismicity distribution observed during this phase, which is mainly clustered at the depth of – and aligned with – the STF, modeling results display conditions for shear failure that may generate on this deep structural feature (STF) as a result of hydraulic stimulation operations in well 27-15. These results (i.e., pressure diffusion → conditions for shear failure on the STF) support the proposed STF-based conceptual model framework, which correctly reproduces the cause-effect relation between well 27-15 stimulation operations and the development of microseismicity – especially when concurrent with injection in well 22-22. The injected fluid pressure diffusion and fluid migration from the formation surrounding this *shallow* open-hole section toward the deeper reservoir might also have been facilitated by: (a) downward migration of cooler (denser) injected fluids, (b) natural fracture networks characterized by higher N-S and vertical permeability, and (c) leakage through the cement plug at the base of the *shallow* open-hole section or through the drilling-induced damage in the formation.

The TFReact model of the main Desert Peak EGS stimulation treatments provides important insights into the permeability change processes activated for given sets of injecting conditions. Injection-induced thermo-mechanical and hydro-mechanical processes are found to govern permeability enhancement during *shallow* interval stimulation in well 27-15. This permeability development is limited to volumes near the wellbore. In fact, a short distance away from the open interval (~10 meters) the effects of fluid pressure and temperature subside. Conversely, induced shear failure processes developing on a larger structural feature (STF) seem to control most of the permeability gain produced during the well 27-15 *extended* interval stimulation. This mechanism delivers higher permeability gains faster and to larger volumes of the reservoir. Distinctive signatures at the well-head (pressure curve) are shown by different permeability-change processes, and this is confirmed and matched by coupled THM simulation results.

The role of the identified structural feature is key to the success of the *extended* interval stimulation, during which extensive shear deformation on the Shearing Target Fault (STF) is associated with the highest permeability gain over the entire experiment. The relation between fluid injection and shear deformation is critical. It appears that during the *shallow* interval stimulation MEQs highlighted a geological structure prone to shear deformation and permeability enhancement (STF): an attractive target which was in fact intersected by the new, extended well completion, and successfully stimulated. The THMC simulation approach presented here − based on the calibration and modeling of actual hydraulic stimulation treatments − is a successful methodology applicable to the design and decision-making processes prior to, during and after any hydraulic stimulation treatment in geothermal environments.

7.1 Usefulness and Applications

Only a comprehensive understanding of these complex physical THMC processes can encourage a more sustainable development of stimulation techniques and routine management aimed at maintaining the required permeability. The Desert Peak stimulation treatment TFReact model provides important insights into the permeability change processes activated for given sets of injecting conditions. These results may bring about the effort needed to make Enhanced Geothermal Systems (EGS) commercially viable and part of a wider package of clean, alternative energy solutions, hopefully meeting global energy demand in the future.

7.2 Innovations and Technical Contributions

This research addresses a problem which has relevance in climate change, energy independence and the development of clean and sustainable alternative energy solutions. It offers an understanding of the levels of uncertainty in complex geosystems by applying and testing novel modeling and multi-scale computational methods. Very little to no modeling work has been

applied to EGS field test cases so far, from stimulation to post-stimulation, and for this reason this research is – computationally and technologically – innovative.